

AD-A193 512

RESEARCH ON CRYSTAL AND FILM FERROELECTRIC MATERIALS
FOR OPTOELECTRONIC A. (U) ROCKWELL INTERNATIONAL
THOUSAND OAKS CA SCIENCE CENTER R R NEURGAONKAR MAR 89

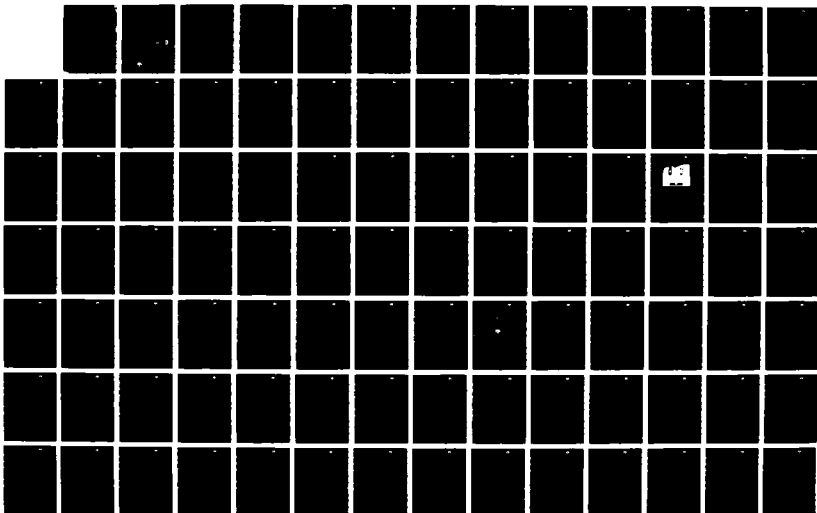
1/2

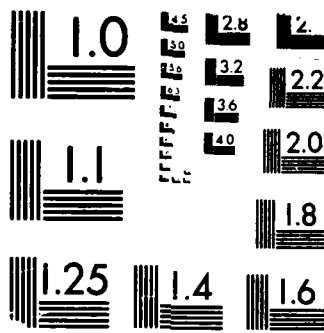
UNCLASSIFIED

SC5345. AR N00014-81-C-0463

F/G 9/5

NL





MICROCOPY RESOLUTION TEST CHART
NBS 1963-A

AD-A193 512

4

SC5345.AR

SC5345.AR

DTIC

Copy No. 4

**RESEARCH ON CRYSTAL AND FILM
FERROELECTRIC MATERIALS FOR
OPTOELECTRONIC APPLICATIONS**

**ANNUAL REPORT FOR THE PERIOD
March 1, 1986 through February 28, 1987**

CONTRACT NO. N00014-81-C-0463

Prepared for

Material Sciences Division
Office of Naval Research
800 North Quincy Street
Arlington, VA 22217
(W.A. Smith)

DTIC
SELECTED
APR 01 1988
S & D

R.R. Neurgaonkar
Program Manager

DISTRIBUTION STATEMENT A

Approved for public release
Distribution Unlimited

MARCH 1988

Reproduction in whole or in part is permitted for
any purpose of the United States Government



Rockwell International
Science Center

88 4 1 10 6

UNCLASSIFIED

SECURITY CLASSIFICATION OF THIS PAGE

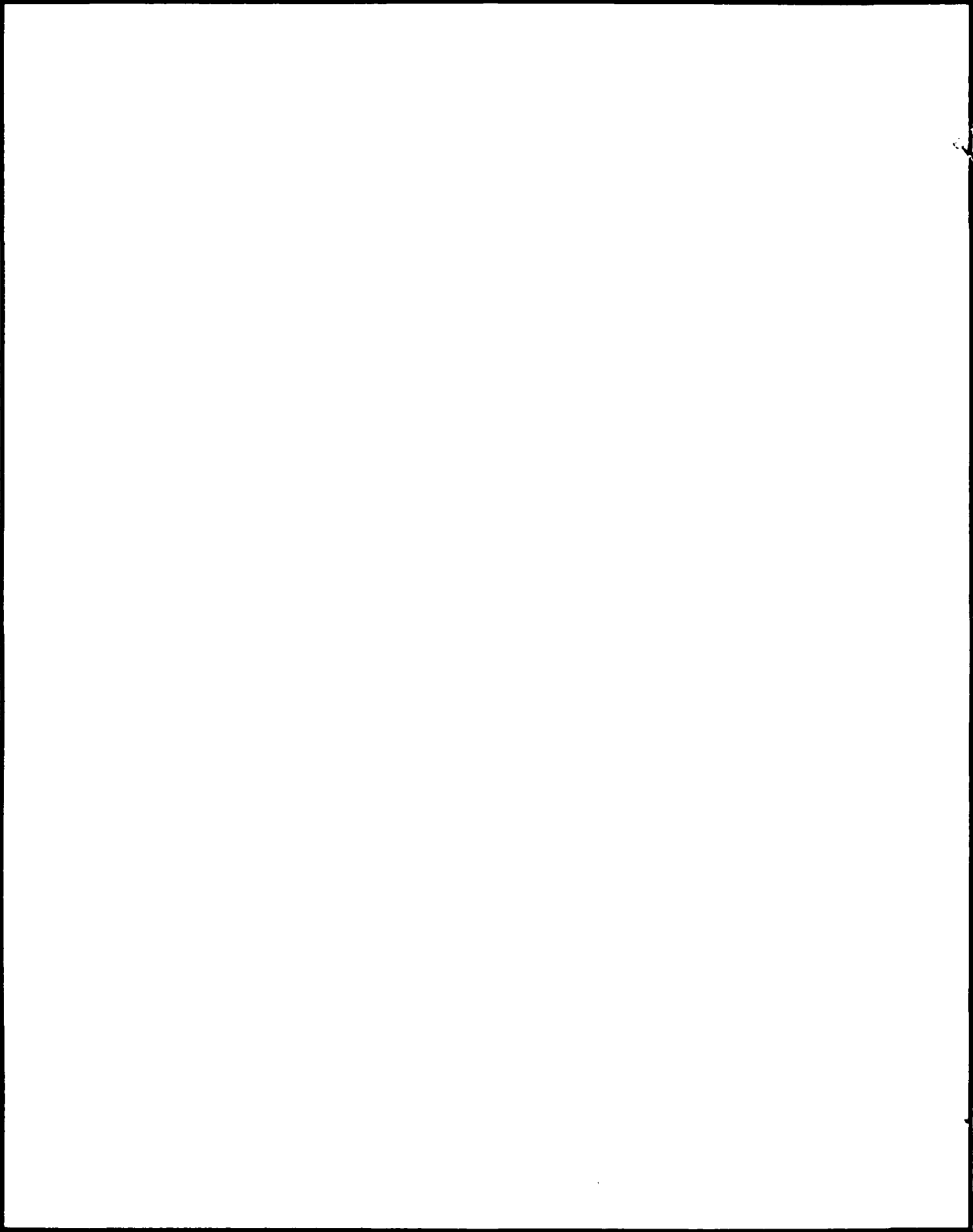
REPORT DOCUMENTATION PAGE

FORM APPROVED
OMB No 0704-0188

| | | | |
|--|---|--|-----------------------------|
| 1a REPORT SECURITY CLASSIFICATION UNCLASSIFIED | | 1b. RESTRICTIVE MARKINGS | |
| 2a SECURITY CLASSIFICATION AUTHORITY | | 3. DISTRIBUTION:AVAILABILITY OF REPORT Reproduction in whole or in part is permitted for any purpose of the United States Government. | |
| 2b. CLASSIFICATION-DOWNGRADING SCHEDULE | | | |
| 4. PERFORMING ORGANIZATION REPORT NUMBER(S) SC5345.AR | | 5. MONITORING ORGANIZATION REPORT NUMBER(S) | |
| 6a NAME OF PERFORMING ORGANIZATION ROCKWELL INTERNATIONAL Science Center | 6b OFFICE SYMBOL <i>(If Applicable)</i> | 7a NAME OF MONITORING ORGANIZATION | |
| 6c ADDRESS (City, State, and ZIP Code) 1049 Camino Dos Rios Thousand Oaks, CA 91360 | | 7b ADDRESS (City, State and ZIP Code) | |
| 8a NAME OF FUNDING SPONSORING ORGANIZATION Material Sciences Division Office of Naval Research | 8b OFFICE SYMBOL <i>(If Applicable)</i> | 9 PROCUREMENT INSTRUMENT IDENTIFICATION NUMBER CONTRACT NO. N00014-81-C-0463 | |
| 8c ADDRESS (City, State and ZIP Code) 800 North Quincy St. Arlington, VA 22217 | | 10 SOURCE OF FUNDING NOS | |
| | | PROGRAM ELEMENT NO. | PROJECT NO. |
| | | TASK NO. | WORK UNIT ACCESSION NO. |
| 11 TITLE <i>(Include Security Classification)</i> RESEARCH ON CRYSTAL AND FILM FERROELECTRIC MATERIALS FOR OPTOELECTRONIC APPLICATIONS | | | |
| 12 PERSONAL AUTHOR(S) Neurgaonkar, R.R. | | | |
| 13a TYPE OF REPORT Annual Report | 13b TIME COVERED FROM 03/01/86 TO 02/28/87 | 14 DATE OF REPORT <i>Year, Month, Day</i> 1988, MARCH | 15 PAGE COUNT 104 |
| 16 SUPPLEMENTARY NOTATION | | | |
| 17 COSAT CODES | | 18 SUBJECT TERMS <i>(Continue on reverse if necessary and identify by block number)</i> | |
| FIELD | GROUP | SUB-GROUP | |
| | | Tungsten bronze ferroelectrics, SBN, BSKNN, millimeter wave, permittivity, loss, electro-optic effect, Perovskite thin films, phenomenology | |
| 19 ABSTRACT <i>(Continue on reverse if necessary and identify by block number)</i> The millimeter wave dielectric behavior of several tungsten bronze ferroelectrics is presented, along with a theoretical evaluation of the origin of the dielectric losses which are shown to arise from polar microdomain fluctuations. Data is also presented for new, La-modified bronze SBN:60 crystals which have very large dielectric constants at room temperature. A comprehensive thermodynamic phenomenology is presented for SBN:60, showing a unique tetracritical phase transition behavior for this ferroelectric. This same phenomenology fails for bronze BSKNN crystals, however, indicating a heretofore unrecognized improper ferroelastic contribution to the dielectric properties. | | | |
| 20 DISTRIBUTION:AVAILABILITY OF ABSTRACT UNCLASSIFIED UNLIMITED <input type="checkbox"/> SAME AS RPT <input type="checkbox"/> DTIC USERS <input checked="" type="checkbox"/> | | 21. ABSTRACT SECURITY CLASSIFICATION UNCLASSIFIED | |
| 22a NAME OF RESPONSIBLE INDIVIDUAL W.A. Smith | 22b TELEPHONE NUMBER <i>(Include Area Code)</i> | 22c OFFICE SYMBOL | |

UNCLASSIFIED

SECURITY CLASSIFICATION OF THIS PAGE



UNCLASSIFIED

SECURITY CLASSIFICATION OF THIS PAGE



TABLE OF CONTENTS

| | <u>Page</u> |
|--|-------------|
| 1.0 INTRODUCTION AND CURRENT STATUS | 1 |
| 2.0 DIELECTRIC PROPERTIES OF FERROELECTRIC La-MODIFIED SBN:60 AT 60 GHz FROM 40K TO 300K | 5 |
| 3.0 COMMENTS ON THE DIELECTRIC SPECTRUM OF TUNGSTEN BRONZE FERROELECTRICS | 20 |
| 4.0 MILLIMETER WAVE ABSORPTION AND REFRACTION IN TUNGSTEN BRONZE FERROELECTRIC | 25 |
| 5.0 FERROELECTRIC PROPERTIES OF La ₃₊ -MODIFIED SBN:60 SINGLE CRYSTALS | 29 |
| 6.0 GROWTH OF PEROVSKITE PZT AND PLZT THIN FILMS | 44 |
| 7.0 A THERMODYNAMIC PHENOMENOLOGY FOR FERROELECTRIC TUNGSTEN BRONZE SBN:60 | 53 |
| 8.0 PRELIMINARY RESULTS ON THE THERMODYNAMIC PHENOMENOLOGY FOR FERROELECTRIC TUNGSTEN BRONZE BSKNN-2 | 86 |



| | |
|--------------------|-------------------------------------|
| Accession For | |
| NTIS | <input checked="" type="checkbox"/> |
| CRA&I | <input checked="" type="checkbox"/> |
| DTIC | <input type="checkbox"/> |
| TAB | <input type="checkbox"/> |
| Unannounced | <input type="checkbox"/> |
| Justification | |
| By <i>per NP</i> | |
| Distribution/ | |
| Availability Codes | |
| Dist | Avail and/or Special |
| <i>A-1</i> | |



1.0 INTRODUCTION AND CURRENT STATUS

The research effort under this contact is part of a long-range program whose objective is to determine the range of dielectric properties attainable at millimeter wave frequencies in various classes of high permittivity ferroelectrics, and to relate these properties to fundamental crystal characteristics. This work involves the preparation of new ferroelectrics in single crystal and ceramic form, characterization of their crystal structure and low frequency dielectric response, and measurement of both linear and non-linear dielectric properties at millimeter wave frequencies.

During the past year, significant progress was made in materials development, millimeter wave dielectric characterization and theoretical modeling efforts. These include:

1. PLZT and PBTF films by magnetron sputtering on a variety of substrates.
2. Successful growth of large-size, high optical quality single crystal BSKNN suitable for free space millimeter wave measurements.
3. Successful growth of SKN single crystal films by LPE on SBN:60.
4. Experimental determination of the millimeter wave dielectric and dn/dE values for La-doped SBN:60 at room and cryogenic temperatures for various crystal orientations.
5. Successful development and testing of a phenomenological model to relate the ferroelectric, dielectric, and electro-optic properties in single crystal tungsten bronze SBN:60.

The factors controlling millimeter wave loss in ferroelectrics are now emerging as evidence accumulates from our studies of the temperature and composition dependence in the tungsten bronzes, and from microstructural characterization of other solid solution systems. Polarization is not uniform, but varies due to microscale compositional fluctuations, providing a means by which the millimeter wave electric field can put energy into the



acoustic modes of the crystal. Fortunately, this loss does not grow as fast with increasing permittivity as does the electric field sensitivity, dn/dE , along the polar axes. We thus have identified a route to obtain the basic device function - phase modulation - with tolerable loss, by moving within the tungsten bronze family toward the highest permittivity compositions.

Our materials growth efforts over the past year have, in fact, been directed toward higher permittivity. PBN doped with La^{3+} was prepared as grain-oriented ceramics, small crystals of SCNN were grown by the Czochralski technique, and new BSKNN compositions were prepared by sintering. In addition, we found that La doping of SBN:60 or :75 dramatically increases the permittivity and other ferroelectric properties. La-doped SBN:60 crystals of 2 cm diameter have now been successfully grown, and have been measured at 60 GHz to compare their high frequency properties with those of undoped SBN:60 single crystals from 40 to 300K. To our surprise, the polar axis permittivity and loss are not much different between doped and undoped samples. However, measurements perpendicular to the polar axis show substantially larger permittivity for La^{3+} -doped SBN:60 crystals with no change in loss. To explore these differences, further measurements of dn/dE are in progress along the polar and nonpolar axes. This information should point out directions for future compositional tailoring to obtain the desired microwave characteristics.

In parallel, we are vigorously pursuing the development of an orthorhombic tungsten bronze crystal, $Sr_{2-x}Ca_xNaNb_5O_{15}$ (SCNN), where we anticipate both longitudinal and transverse electro-optic coefficients to be extremely large. Since the polar axis permittivity of SCNN is larger than for pure SBN:60, we expect that dn/dE along both directions will be large compared to all other crystals studied under this program. On the basis of these results, we will classify the range of millimeter wave properties obtainable in the tungsten bronze family leading to the definition of appropriate device concepts.

Our successful development of growth techniques for the various types of tungsten bronzes, coupled with our improved knowledge of the interrelationship of the materials properties within this family, now provides an opportunity for both developing a fundamental understanding of mechanisms and exploiting the ferroelectric properties of these bronzes in various device concepts.



This year, we also initiated research on thin film growth of ferroelectric materials by the magnetron sputtering and liquid phase epitaxial (LPE) techniques. Figure 1.1 summarizes the number of applications that will be possible when these films become available. Currently, high figure-of-merit ferroelectrics, specifically Pb^{2+} -containing materials such as perovskite PZT, PLZT, PBTf or tungsten bronze PbNb_2O_6 or $\text{Pb}_2\text{KNb}_5\text{O}_{15}$, are difficult to grow in single crystal form and their usefulness for device applications is limited. We have successfully grown single crystal and polycrystalline tungsten bronze PbNb_2O_6 and perovskite PLZT, $\text{Pb}_{1-x}\text{Bi}_x\text{Ti}_{1-x}\text{Fe}_x\text{O}_3$ (MPB composition) thin films on tungsten bronze SBN:60 substrates with thicknesses between 1 to 10 μm . This is the first time perovskite single crystal films have been grown on tungsten bronze substrates, and we expect that such integration will permit a variety of applications for these films. We will continue to explore these growth techniques for the MPB compositions to enhance their quality and performance for devices. The ferroelectric thin film area is relatively new in the USA, and the opportunities to exploit large figure-of-merit compositions are numerous.

We have performed an extensive phenomenological investigation of tungsten bronze SBN:60 and BSKNN crystals showing that the Gibbs free-energy expansion must be taken out to the eighth power of the polarization with strong temperature dependencies for Devonshire coefficients up to the sixth power, totally unlike what is encountered in perovskite systems. The results show well-behaved properties for SBN:60, which appears to have a tetracritical ferroelectric phase transition. BSKNN-2 is also well-behaved for an 80° range below its tetracritical transition, but shows anomalous phenomenological behavior below 90°C and predicted metastable energy states below room temperature. Hence, BSKNN-2 appears to have a previously unknown ferroelastic transition somewhere below the ferroelectric transition, a factor which may help to explain the unusual electro-optic behavior of this ferroelectric material at millimeter wave and optical frequencies.

The details of the research performed during this past year are given in the remaining sections of this report in the form of individual research papers. Each of these papers is being submitted or has been accepted for publication, or has been published in a particular scientific journal.



PIEZOELECTRIC AND ELECTRO-OPTICS

- LARGE k^2 AND d_{33}/ϵ
- TEMPERATURE COMPENSATED ORIENTATIONS
- GRAIN ORIENTED TO SINGLE CRYSTAL FILMS
- THICKNESS GREATER THAN $8 \mu\text{m}$

SUBSTRATES: SBN, ZNO, GLASS, GaAs

APPLICATIONS: FILTERS, RESONATORS,
SENSORS (UNDERWATER),
ADAPTIVE OPTIC, PHASE MODULES

PHOTOREFRACTIVE

- LARGE $n^3 r_{ij}/\epsilon$
- SINGLE CRYSTAL FILMS
- THICKNESS $\sim 5 \mu\text{m}$

SUBSTRATES: GaAs OR SBN

APPLICATIONS: ERASABLE STORAGE

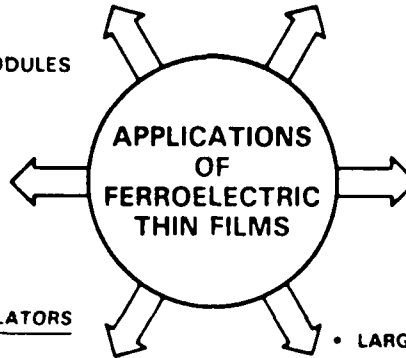
SPATIAL LIGHT MODULATORS

- LARGE r_{51} OR r_{13}/ϵ
- SINGLE CRYSTAL FILMS
- THICKNESS 1 TO $5 \mu\text{m}$

SUBSTRATES: GaAs, Si, SBN

APPLICATIONS: OPTICAL SIGNAL PROCESSING,
INCOHERENT-TO-COHERENT
CONVERSION

NEW OPPORTUNITIES?



GUIDED WAVE OPTICS

- LARGE r_{ij}/ϵ
- LOW OPTICAL LOSSES
- THICKNESS $3-5 \mu\text{m}$
- SINGLE CRYSTAL FILMS

SUBSTRATES: GaAs, Si, SBN

APPLICATIONS: WAVEGUIDES, SWITCHES,
MODULATORS

PYROELECTRIC DETECTORS

- LARGE p/ϵ
- LOW TAN δ
- THICKNESS $\sim 1 \mu\text{m}$
- GRAIN ORIENTED TO SINGLE CRYSTAL FILMS

SUBSTRATES: NONFERROELECTRICS

APPLICATIONS: UNCOOLED FOCAL PLANE ARRAYS,
VIDICON

Fig. 1.1 Device concepts for ferroelectric thin films.



Rockwell International
Science Center

SC5345.AR

2.0 DIELECTRIC PROPERTIES OF FERROELECTRIC La-MODIFIED
SBN:60 AT 60 GHz FROM 40K TO 300K



DIELECTRIC PROPERTIES OF FERROELECTRIC La-DOPED

SBN:60 AT 60 GHz FROM 40 K TO 300 K

W.F. Hall, W.W. Ho, R.R. Neurgaonkar, and P.J. Hood

Abstract

Results of measurements on the dielectric properties of the La-doped tungsten bronze ferroelectric $\text{Sr}_{0.6}\text{Ba}_{0.4}\text{Nb}_2\text{O}_6$ at 60 GHz are reported and compared with earlier measurements on the undoped crystals over the range of temperatures from 40 K to 300 K. An interpretation of the high frequency dielectric behavior of the tungsten bronzes in terms of microscopic variation in the spontaneous polarization is discussed.

Introduction

This paper reports on the final phase of a multiyear research program on millimeter wave properties of the tungsten bronze ferroelectrics. This research has been performed largely under ONR sponsorship, in conjunction with extensive development of growth techniques for tungsten bronze crystals funded by DARPA and ONR.

Our work on the millimeter wave properties of ferroelectrics was inspired by the observation in 1980^[1] that a large change could be induced in the microwave refractive index of a strontium barium niobate (SBN) single crystal by the application of an electric field. This unusual sensitivity can potentially be used to perform a variety of functions, including frequency doubling and mixing, as well as beam steering by means of controlled index gradients in a dielectric lens. Previous measurements on other ferroelectrics^[2,3] at millimeter wavelengths had shown similar effects, but at a much lower level.



To establish the fundamental properties of a ferroelectric material at high frequency, measurements on single crystal samples are generally required. However, most strongly ferroelectric materials are available only in ceramic form or as millimeter-size crystals. Thus, the ongoing program to grow tungsten bronze ferroelectrics in larger size and optical quality^[4] provided us a unique opportunity. In addition to SBN, we have been able to examine a variety of niobate bronzes which incorporate barium, strontium, potassium, and sodium in different amounts^[5,6,7].

Results in this paper are given for $\text{Sr}_{0.6}\text{Ba}_{0.4}\text{Nb}_2\text{O}_6$ doped with La^{3+} to 1.0 mole percent. This doping has been found to lower the temperature of the ferroelectric–paraelectric transition from 75 C to 38 C^[8], as shown in Figure 1.

The features common to all the ferroelectrics we have studied include:

- 1) A large decrease in permittivity along the crystal polar axis from dc to GHz frequencies
- 2) A large dielectric loss along the polar axis, persisting at least from 30 GHz to 120 GHz
- 3) A large temperature dependence of these properties
- 4) Smaller, but still substantial, loss perpendicular to the polar axis at room temperature, with little decrease on cooling.

This behavior in the dielectric properties of good single crystals was unexpected. According to the accepted soft-mode model^[9], the polar axis permittivity ϵ_p is large for simple, proper ferroelectrics because of a relatively low-frequency, optically active lattice mode, whose contribution to ϵ_p takes the form:

$$\Delta\epsilon_p(\omega) = \frac{A}{\omega_0^2 - \omega^2 - i\omega\Gamma_0} \quad (1)$$

where ω_0 is the soft-mode radian frequency, Γ_0 is its damping, and ω is the radian frequency of the incident electromagnetic wave (time dependence $e^{-i\omega t}$). The soft-mode



frequency tends toward zero at the ferroelectric paraelectric transition temperature T_c , being proportional to $(|T - T_c|)^{1/2}$; this gives the usual Curie-Weiss law for $\epsilon_p(0)$ when T is near T_c . Depending on the size of the damping Γ_0 , this model predicts either a negligible frequency dependence below $\omega_0/3$ for $\Gamma_0 < \omega_0$, or a Debye-type relaxation for $\Gamma_0 > \omega_0$. Neither behavior fits the observed frequency dependence in tungsten bronze ferroelectrics.

Experimental Method

In the early phases of this measurement program, sample sizes were small, but adequate to fill a waveguide cross-section at 30 GHz and above. For this reason, power reflection and transmission measurements were carried out in waveguide over the full waveguide band, and the results were analyzed in terms of the sample eigenmodes. Because of the high dielectric permittivity of the sample, great care had to be exercised to eliminate propagation around the sample through any small gaps between the guide wall and the sample. When samples larger than 10 mm became available, free space reflection and transmission using spot focusing lenses became the method of choice above 50 GHz.

The experimental system developed for determining the millimeter-wave dielectric properties of planar samples at cryogenic temperatures is shown schematically in Figure 2. The measurement system consists of a set of spot-focusing lens antennas with a diameter of 15.25 cm, and an f -number of unity suitably positioned such that the sample is at the focal plane of the lens antennas. The spot size of the focused beam is nearly diffraction-limited, and is of the order of 1.5 cm at 35 GHz.

The sample to be characterized is mounted in a vacuum cryogenic cold-stage chamber, where thin fused SiO windows are used to allow the incoming millimeter-wave radiation to pass through the chamber. The power transmission coefficient as a function of frequency at a given incidence angle is determined by first obtaining a background spectrum with the windows in place, but with the sample removed. Power levels are calibrated with the



precision rotary-wave attenuator, as shown in the microwave circuitry of Figure 2. The sample is then placed in the holder and the with-and-without sample difference spectrum is recorded. Microwave absorbers are suitably placed in the chamber to minimize stray radiation from reaching the detector via multiple reflections. The same procedure is used to obtain the power reflection coefficient except, in this case, the calibration is performed by replacing of the sample with an identically sized polished Cu plate. In addition, a phase bridge is incorporated into the apparatus as shown to determine the phase accumulation of the transmitted signal through the sample, and to monitor the relative phase change as a function of sample temperature. The dielectric properties of the sample are then computed from the observed transmission and reflection coefficients and/or phase change as a function of frequency for a given sample thickness and orientation. The current measurements on La-doped SBN:60 were carried out from 55 to 65 GHz on a sample 10 mm by 10 mm at temperatures ranging from 40 to 300 K. Earlier measurements on undoped SBN:60 had been carried out at this laboratory^[7] and by Bobbs, *et al.* at UCLA^[10] from 50 to 110 GHz.

Results

The purpose of extending our dielectric property measurements to La-doped SBN:60 is to test whether a shift in transition temperature significantly affects the general character of the millimeter wave response. Table 1 summarizes the comparison with pure SBN:60 for both crystal axes at two temperatures. The trends observed in the two samples are quite similar, except that the polar axis permittivity decreased much more on cooling in the doped crystal. Doping does not appear to increase the loss at these frequencies (55-65 GHz for the doped sample, 30-50 GHz for the pure SBN:60).

The variation in millimeter wave properties with temperature for the La-doped SBN:60 is plotted in Figures 3 and 4. These data conform to the behavior found in the other bronzes. An idea of the uncertainty in our technique for determining the dielectric properties is provided by the alternative fitted points at 40 K in Figure 3. Both the



Table 1

Millimeter Wave Dielectric Properties of La-Doped and Undoped SBN:60

| Axis | Temp (°K) | Doped ϵ' | Doped ϵ'' | Pure ϵ' | Pure ϵ'' |
|------|-----------|-------------------|--------------------|------------------|-------------------|
| c | 295 | 150 | 73 | 158 | 86 |
| | 77 | 50 | 13.6 | 124 | 8.8 |
| a | 295 | 326 | 53 | 231 | 51 |
| | 77 | 260 | 36 | 190 | 37 |

transmitted phase and the attenuation across the band from 55 to 65 GHz could be fit with a few percent increase in error for the starred values of ϵ' and ϵ'' .

Discussion

The model we have proposed to explain the millimeter wave dielectric response in these materials^[7] postulates that the polarization P in the ferroelectric phase is not strictly uniform throughout the crystal, but varies on a submicron scale in both direction and magnitude. This is likely due to variations in site occupancy from unit cell to unit cell^[11], and the consequence of such a variation is a distribution of electric charge $\rho = \nabla \cdot P$ around the resulting microdomains. The microwave electric field E can couple efficiently to this charge distribution through the piezoelectric effect, generating acoustic waves as the walls of these microdomains are driven against the host.

To derive an estimate for the magnitude of this effect, one can consider planar domain walls separated by a distance d along the polar (3-) axis, driven by the piezoelectric stress



(due to reversed internal polarization)

$$X_{33} = 2Q_{3333} (\epsilon'_{33} - 1) \epsilon_0 P_3^0 c_{3333}^p E_3 \quad , \quad (2)$$

where Q is the electrostriction tensor, ϵ_0 is the permittivity of vacuum, and c^p is the tensor of elastic moduli. The irreversible work done on such a domain by the microwave electric field for a harmonic excitation of frequency ω can be summed over all domains in the sample volume V to give the electrical dissipation $\omega \epsilon_{33}'' \epsilon_0 E_3^2 \cdot V$, with the result

$$\epsilon_{33}'' \epsilon_0 = \frac{[X_{33}/E_3]^2}{\rho v \omega V} \sum_n A_n \sin^2 \left(\frac{\omega d_n}{v} \right) \quad , \quad (3)$$

where ρ is the mass density and v the sound velocity in the crystal, and A_n is the wall area of the n^{th} domain. For microwave frequencies where the acoustic wavelength is large compared to the average domain size \bar{d} ($\omega \bar{d}/v \ll 1$), this relation predicts a dielectric loss proportional to ω , while at the other extreme ($\omega \bar{d}/v \gg 1$), the loss will be proportional to ω^{-1} . For intermediate wavelengths, a more accurate expression including acoustic damping should be used, but the general shape is a broad maximum centered at $\omega \bar{d}/v = 1$, very similar to the Debye relaxor. A comparable expression for dielectric loss in a polydomain sample has been derived by Turik and Shevchenko^[12] for BaTiO₃.

An unusual feature of this loss mechanism is that it relates ϵ_{33}'' at the microwave frequency to ϵ_{33}' at the same frequency, predicting that the ratio $\epsilon_{33}''/(\epsilon_{33}' - 1)^2$ is proportional to the number density of reversed microdomains and to the square of the polarization. The upper curve in Figure 5 shows the behavior of this ratio with temperature for the La-doped SBN:60 crystal. One can tentatively associate the observed rise and fall of this ratio as due to the competing effects of an increase in the number N_r of reversed domains and a decrease in the polarization, which becomes pronounced as T_c is approached.



The high microwave loss observed for electric field perpendicular to the polar axis can be explained from the same model, if one assumes that the polarization axis within a microdomain can be tilted with respect to the host polar axis. This produces a perpendicular component P_{\perp} to the polarization which can couple to the microwave field, and whose magnitude is independent of the direction of the polarization in the microdomain. The dielectric loss predicted by this model is therefore proportional to the total number N_d of such domains, reversed or not. The corresponding ratio $\epsilon''_{11}/(\epsilon'_{11} - 1)^2$ is plotted as the lower curve in Figure 5. It is very nearly constant from 40 K to 300 K, which implies that the product $N_d P_{\perp}^2$ is independent of temperature. This observation is qualitatively consistent with recent reports^[13] of a random polarization that persists above T_c , which affects the birefringence and electrostrictive behavior in ferroelectric crystals.

Acknowledgment

This work was funded by the Office of Naval Research under Contract N00014-81-C-0463.

References

1. W. Ho, W.F. Hall, R.R. Neurgaonkar, R.E. DeWames, and T.C. Lim, *Ferroelectrics* **38**, 833 (1981).
2. G.D. Boyd, T.J. Bridges, M.A. Pollack, and E.H. Turner, *Phys. Rev. Lett.* **26**, 387 (1971).
3. M.B. Klein, *Int. J. Infrared and Millimeter Waves* **2**, 239 (1981).
4. R.R. Neurgaonkar, W.K. Cory, and J.R. Oliver, *Ferroelectrics* **51**, 3 (1983).
5. R.R. Neurgaonkar, W.W. Ho, W.K. Cory, and W.F. Hall, *Ferroelectrics* **51**, 185 (1984).



6. W.W. Ho, W.F. Hall, and R.R. Neurgaonkar, *Ferroelectrics* 50, 325 (1983).
7. W.F. Hall, W.W. Ho, R.R. Neurgaonkar, and W.K. Cory, in *Proceedings of the IEEE 1986 International Symposium on Applications of Ferroelectrics*, p. 469.
8. R.R. Neurgaonkar, J.R. Oliver, W.K. Cory, and L.E. Cross, manuscript submitted to *Ferroelectrics*.
9. See, for instance, Chapter II in *Principles and Applications of Ferroelectrics and Related Materials*, by M.E. Lines and A.M. Glass, Clarendon Press (Oxford, 1977).
10. B. Bobbs, M. Matloubian, A.R. Fetterman, R.R. Neurgaonkar, and W.K. Cory, *Appl. Phys. Lett.* 48, 1642 (1986).
11. L.A. Bursill and Peng Ju Lin, *Phil. Mag. B* 54, 157 (1986).
12. A.V. Turik and N.B. Shevchenko, *Physica Status Solidi B* 95, 585 (1979).
13. G. Burns and F.H. Dacol, *Physical Review B* 30 (7), 4012 (1984).



SC37102

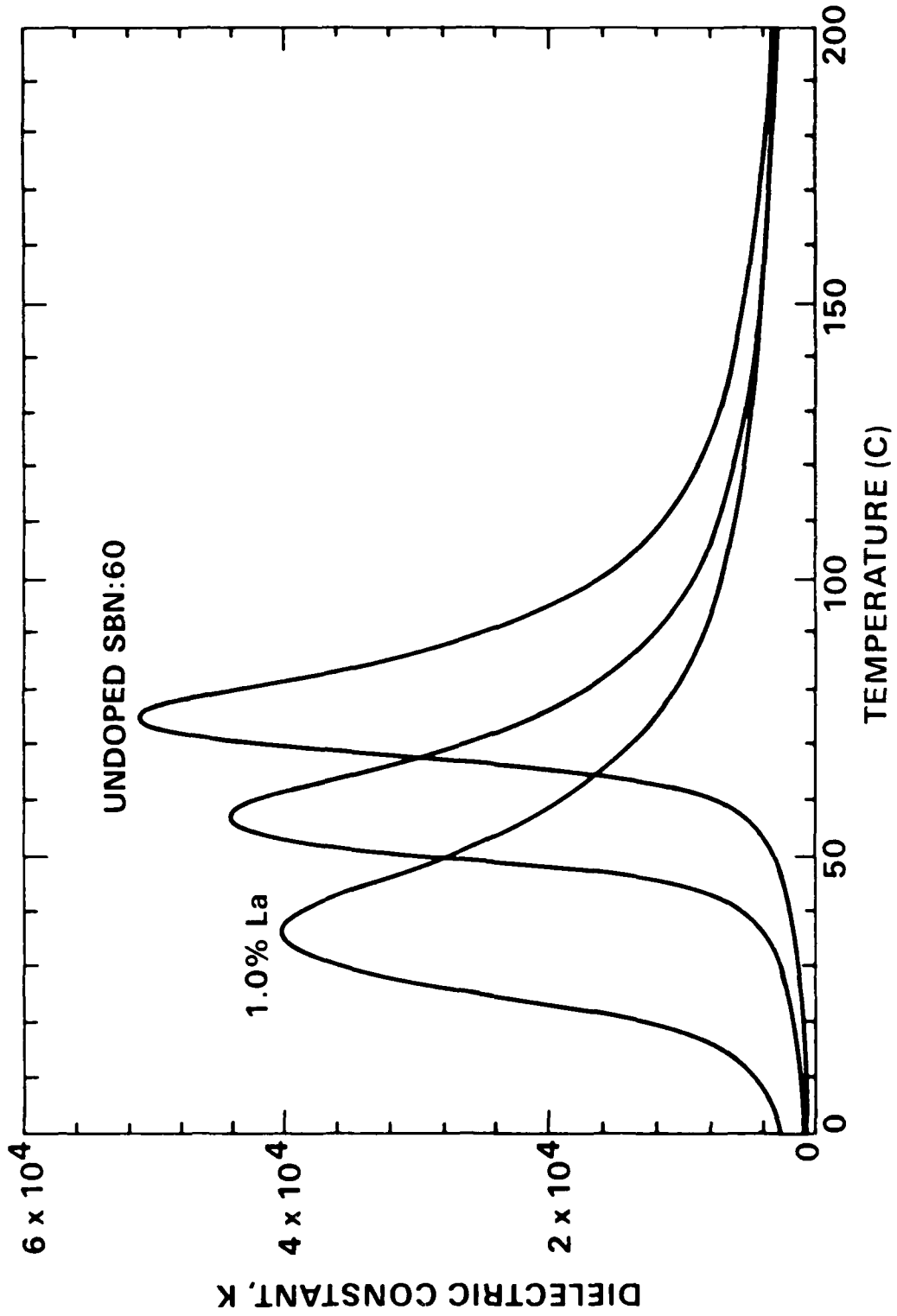


Figure 1. Low frequency polar axis permittivity of SBN:60 single crystals doped to various levels with La³⁺.



SC41897

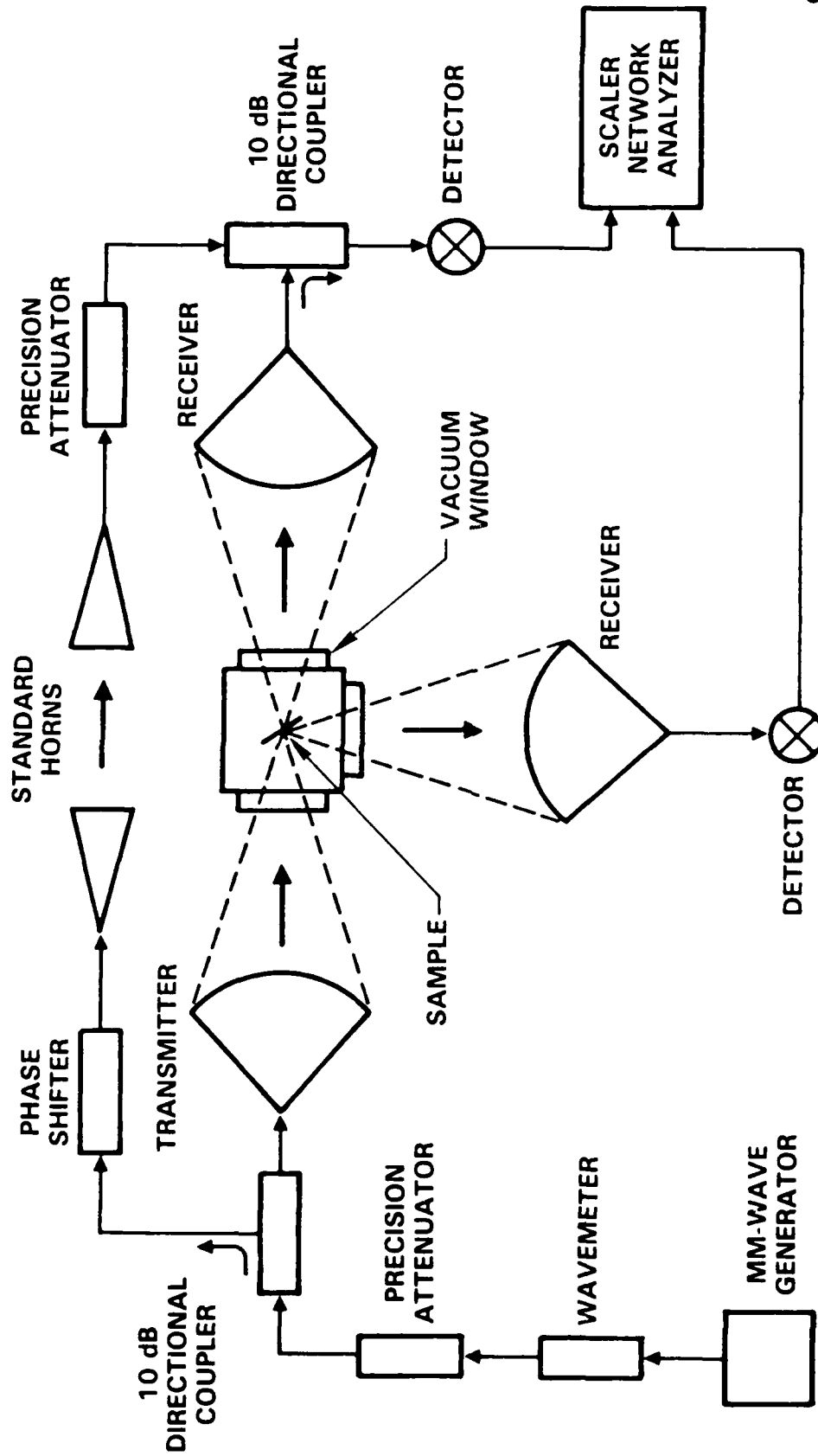


Figure 2. Millimeter wave measurement system for reflection and transmission of planar samples at cryogenic temperatures.

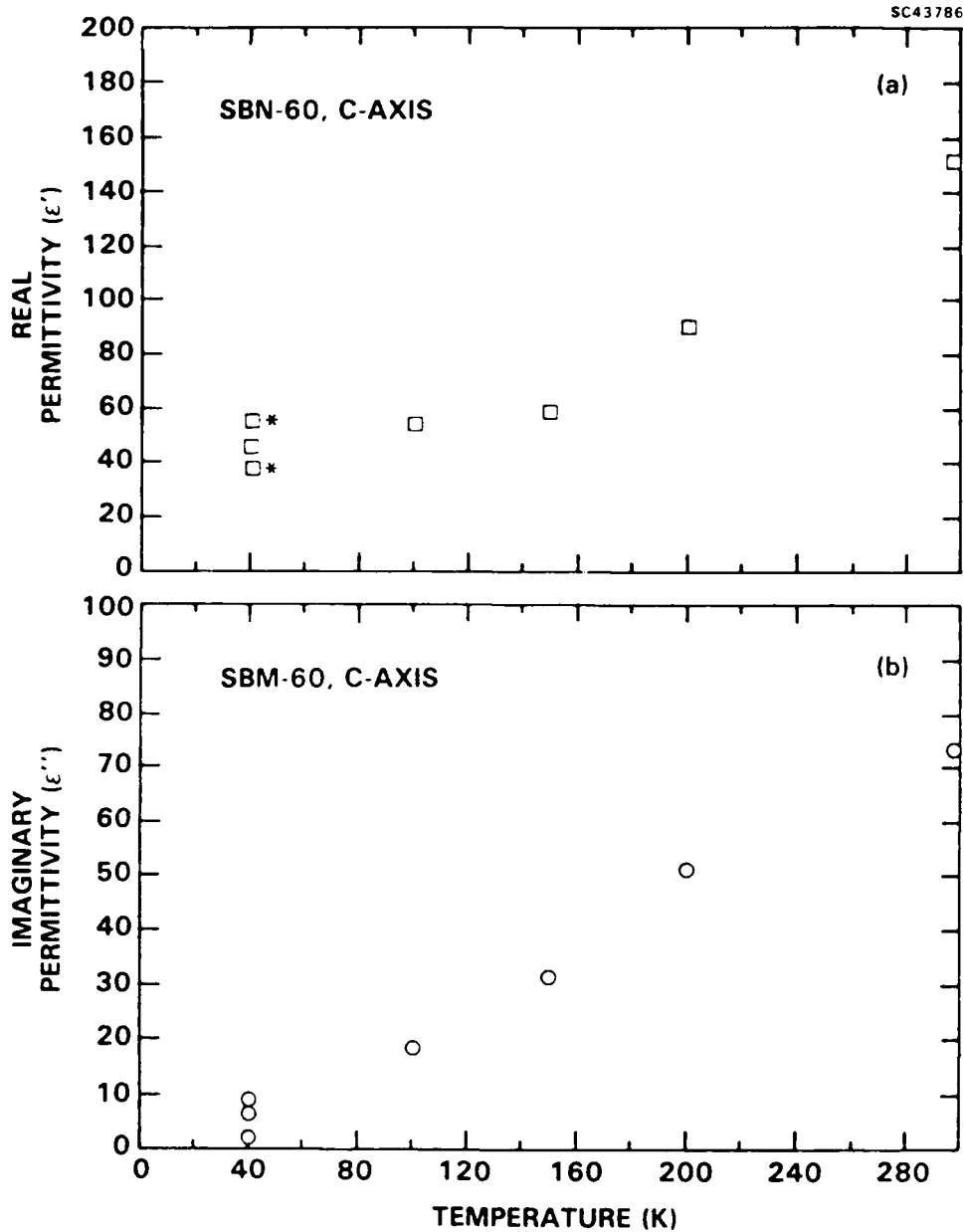


Figure 3. Polar axis permittivity (ϵ') and loss (ϵ'') at 60 GHz from 40 K to 300 K. The asterisked values at 40 K are alternative fits to the measured transmission and phase from 55 to 65 GHz.

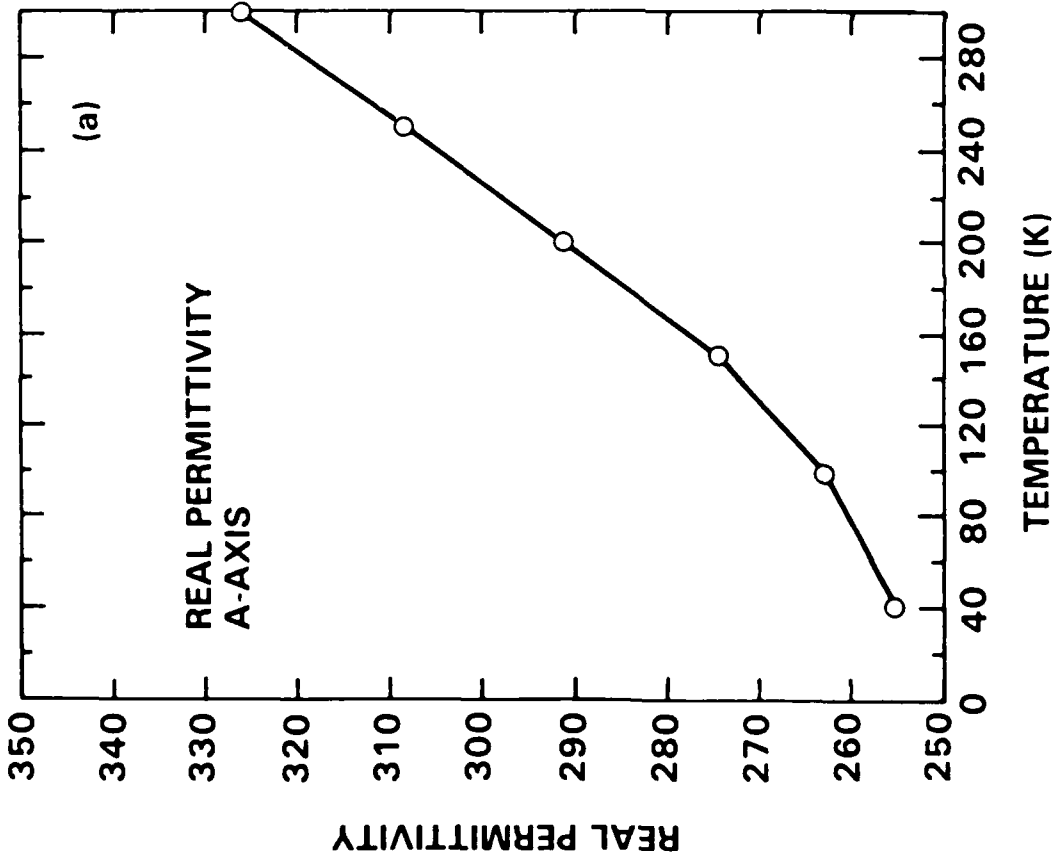
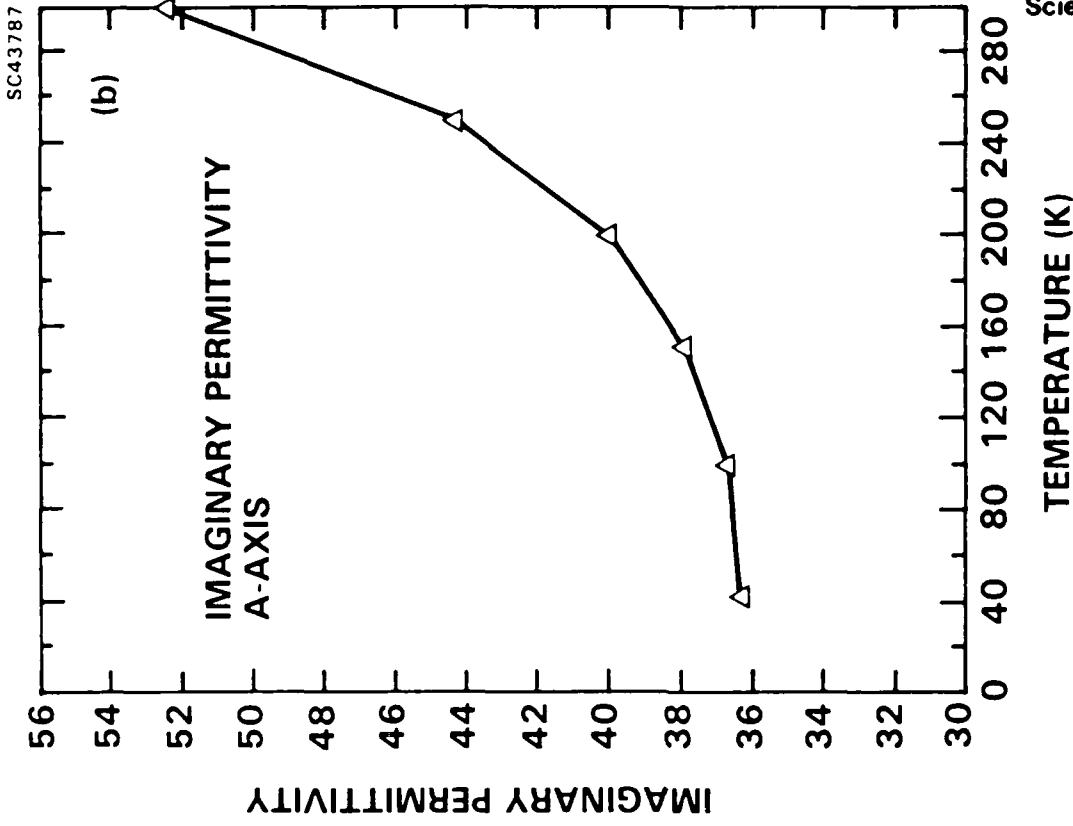


Figure 4. Permittivity and loss perpendicular to the polar axis at 60 GHz from 40 K to 300 K.

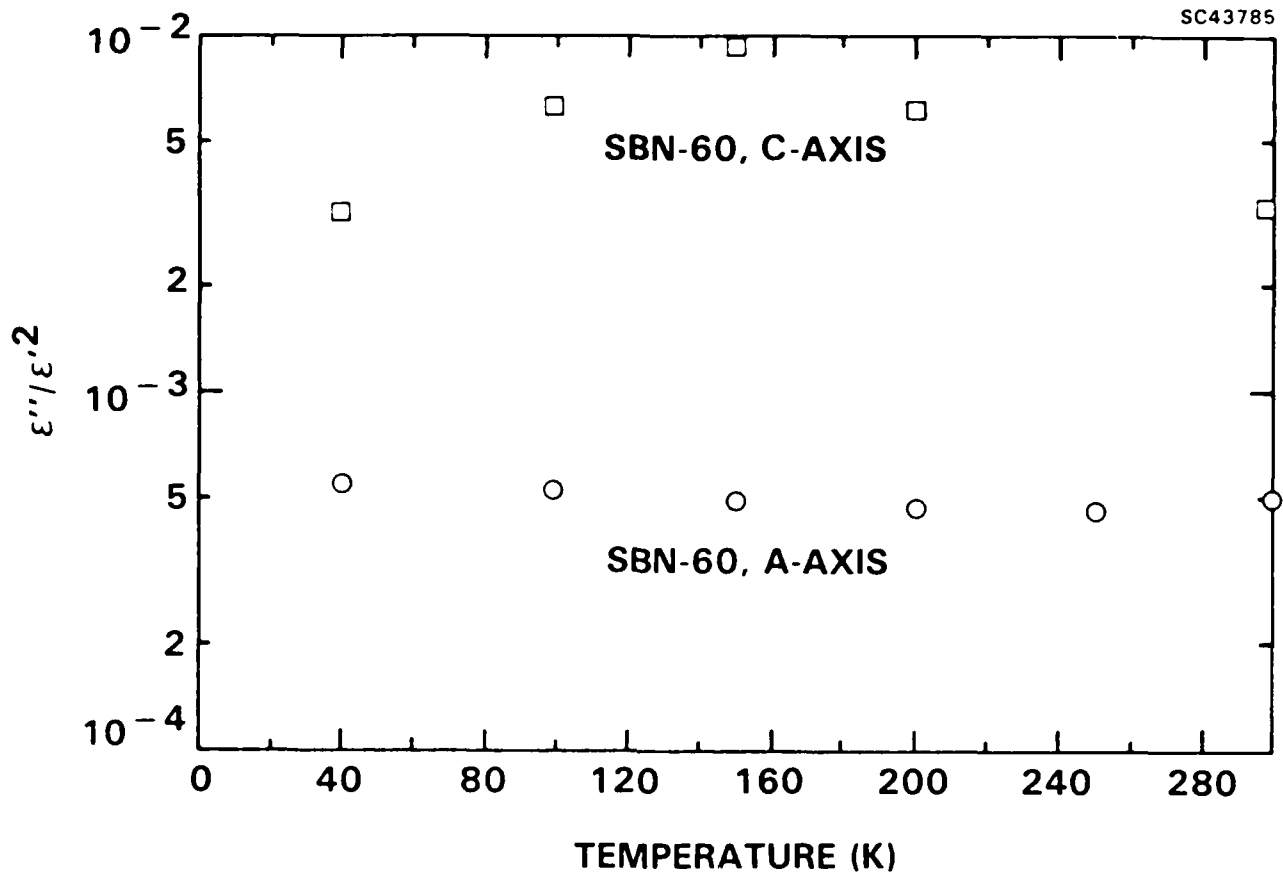


Figure 5. Dielectric loss ratio $\epsilon''/(\epsilon' - 1)^2$ at 60 GHz for microwave electric field along the polar axis (upper curve) and perpendicular to the polar axis (lower curve). The microdomain loss model predicts this ratio to be proportional to $N P^2$, where N is the number density of microdomains that couple to the applied field and P^2 is the component of the mean square polarization parallel to the field in each domain.



Rockwell International
Science Center

SC5345.AR

**3.0 COMMENTS ON THE DIELECTRIC SPECTRUM OF TUNGSTEN
BRONZE FERROELECTRICS**



COMMENTS ON THE DIELECTRIC SPECTRUM OF TUNGSTEN BRONZE FERROELECTRICS

W.F. Hall, W.W. Ho, and R.R. Neurgaonkar

Abstract

An explanation is proposed for the anomalous behavior with frequency and temperature of the dielectric properties in tungsten bronze ferroelectrics.

The dielectric properties of single crystal, single domain ferroelectrics of the tungsten bronze structure have been found to exhibit substantial dispersion and loss at frequencies up to 140 GHz and for temperatures as low as 77°K. In fact, the major part of the polar axis permittivity in these crystals is apparently due to relaxation processes that "freeze out" below 10 GHz. Between 20 and 140 GHz, the observed dispersion has been qualitatively explained as resulting from spatial disorder of the internal polarization on a submicron scale⁽¹⁾.

This picture contrasts markedly with the classical model of a single domain ferroelectric, which is characterized by a uniform spontaneous polarization that disappears at the Curie temperature, and whose dielectric spectrum is dominated by a soft mode located above 1000 GHz. However, evidence has been accumulating from many sources^(2,3,4) that, at least in solid solution ferroelectrics, the well defined average crystal structure determined from conventional X-ray scattering conceals a range of submicroscopic composition fluctuations and lower symmetry structures.

These inferred deviations from ideal symmetry and uniformity provide a reasonable basis for explaining all the anomalous dielectric behavior of tungsten bronzes in the ferroelectric phase. In essence, the local polarization is considered to deviate in direction and magnitude from the average, and to respond to external electric fields by reorientation on a relatively long time scale.

A model for the reorientational contribution to the dielectric properties has been developed by A.V. Turik^(5,6) and co-workers to explain the observed dielectric spectra of barium titanate single crystals. This model idealizes the orientational interaction as a two-minimum system (corresponding to the local dipole moment lying either parallel or antiparallel to the average polarization P_0) with an energy difference $U_0 = 2\mu E_s$ between



the levels, where μ is the dipole moment of a reorientable cluster of unit cells and E_s is the local electric field due to charged defects and the spontaneous polarization of the environment. The contribution to the crystal polarizability from these clusters is then

$$\Delta\epsilon_r = \frac{N\mu^2}{kT \cosh^2(U_0/kT)} \quad (1)$$

where N is the number of clusters per unit volume, T is the temperature, and k is Boltzmann's constant.

The characteristic time τ_r for reorientation of a dipole is also temperature-dependent, and involves two additional parameters, the height U_1 of the potential energy barrier separating the two orientational minima, and a Lorentz factor β expressing the degree of screening between neighboring dipoles:

$$\tau_r = \frac{e^{U_1/kT}}{2\nu \cosh(U_0/kT)} \frac{\epsilon_{33}^0 - 1 + \frac{4\pi}{\beta}}{\epsilon_{33}^\infty - 1 + \frac{4\pi}{\beta}} \quad (2)$$

Here ϵ_{33}^0 is the dc polar axis permittivity, ϵ_{33}^∞ is the low-frequency value calculated using the Lyddane-Sachs-Teller (LST) relation on the phonon modes deduced from Raman spectral data, and ν is the frequency of orientational vibration of the dipoles about one of the minima (a typical phonon frequency, $\approx 10^{13}$ Hz).

The important features of this model to note here are that a large dc permittivity can be obtained with a modest volume fraction of clusters, and that at frequencies much higher than τ_r^{-1} the dipoles appear as frozen-in disorder. This disorder in turn will give rise to the high-frequency dispersion calculated in Reference 1.

A straightforward application of this picture to a uniaxial ferroelectric would imply that only the polar axis dielectric spectrum is modified from its expected soft-mode form. However, observations on the tungsten bronzes have shown that the dielectric properties perpendicular to the polar axis are also anomalous⁽¹⁾. In particular, at millimeter wavelengths a high dielectric loss is found that persists over the range of temperature from 77°K to 300°K. This contrasts with the polar axis loss, which decreases markedly on cooling in approximately the manner implied by equation (1).

To explain this persistent high loss, one needs only to consider that the cluster polar axis may be tilted with respect to the crystal axes. This provides both a mechanism for coupling perpendicularly polarized microwave fields into the polar disorder and a reason that the loss should persist, namely that in either orientation, the cluster dipole will have the same magnitude for its perpendicular component. Thus, even though the fraction of



antiparallel dipoles decreases rapidly with decreasing temperature, the coupling of each dipole to the perpendicular electric field is unchanged.

The qualitative agreement described above for the major features of the dielectric spectrum make it worthwhile to pursue this model in detail. In particular, other physical consequences of polarization disorder and dipolar relaxation should be investigated. These include crystal properties that are sensitive to even powers of the polarization, such as optical birefringence⁽⁴⁾. They will provide an independent measure of the magnitude and symmetry of the spatial fluctuations in P_0 .

Also needed is a microscopic theory for the various parameters that enter into the reorientational model. Microstructural characterization techniques such as transmission electron microscopy are now yielding semiquantitative data with which to test such a theory^(2,3). Clearly, a lattice dynamics description of a cluster and its environment will contain many of the required features.

One implication of this explanation for the microwave properties is that the large dc permittivities in these ferroelectrics are not directly connected with the soft mode of the paraelectric phase. Consequently, optical and microwave nonlinearities should be expected to correlate independently with the LST values for ϵ_{ii} and with the remaining polarizability at the measurement and modulation frequencies.

We consider the specific case of the microwave electro-optic coefficient, dn_{ii}/dE_j , where n_{ii} is the refractive index at microwave frequency ω_1 and E_j is the modulating electric field at frequency $\omega_0 \ll \omega_1$. According to the Devonshire free energy model developed by Cross⁽⁷⁾ and co-workers, the dielectric stiffness χ_{ii} varies with applied field along the polar axis j as

$$\frac{d\chi_{ii}}{dE_j} \sim \alpha_{ij} P_j \epsilon_{jj}(\omega_0) \quad , \quad (3)$$

where the coefficient α and the polarization P are frequency independent properties of the crystal. Since $\chi_{ii} = (n_{ii})^{-2}$, this gives for the electro-optic coefficient the result

$$\frac{dn_{ii}}{dE_j} \sim \alpha_{ij} P_j \epsilon_{jj}(\omega_0) n_{ii}^3(\omega_1) \quad . \quad (4)$$

In this expression, the first two factors appear to be substantially constant across the tungsten bronze family of tetragonal ferroelectrics⁽⁷⁾, the third factor $\epsilon_{jj}(\omega_0)$ is dominated by the reorientational relaxation process, and the last factor is determined at millimeter wave frequencies by the remaining disorder in the polarization at a given temperature. Since this disorder should be roughly proportional to the number of reorientable dipoles, one recovers an approximate scaling of dn/dE with $n^5(\omega_1)$ within the tungsten bronze family, as reported in Reference 1.



ACKNOWLEDGEMENT

This work was supported under ONR Contract No. N00014-C-81-2260. The authors are grateful to Prof. L.E. Cross for his valuable suggestions during the course of this investigation.

REFERENCES

1. W.F. Hall, W.W. Ho, R.R. Neurgaonkar, and W.K. Cory, "Millimeter wave dielectric properties of tungsten bronze ferroelectrics at 77 and 300 K," to be published in Proceedings of the IEEE 1986 International Symposium on the Applications of Ferroelectrics.
2. L.A. Bursill and Peng Ju Lin, "Chaotic states observed in strontium barium niobate." *Phil. Mag. B* 54, 157 (1986).
3. H.M. Chan and M.P. Harmer, "Microstructure and Microchemistry in PST-PMN-PZN Relaxor Ferroelectrics," to be published in Proceedings of the IEEE 1986 International Symposium on the Applications of Ferroelectrics.
4. G. Burns and F.H. Dacol, "Glassy polarization behavior in $K_2Sr_4(NbO_3)_{10}$ -type ferroelectrics," *Phys. Rev. B* 30, 4012 (1984).
5. A.V. Turik, E.N. Sidorenko, and V.F. Zhestkov, "Microwave dispersion of the permittivity of single-domain $BaTiO_3$ crystals," *Sov. Phys. Solid State* 24, 840 (1982).
6. A.V. Turik and N.B. Shevchenko, "Dielectric spectrum of $BaTiO_3$ single crystals." *Phys. Stat. Sol. B* 95, 585 (1979).
7. L.E. Cross and R.R. Neurgaonkar, "A phenomenological analysis of tetragonal tungsten bronze ferroelectrics," submitted to *J. Materials Sci.*



Rockwell International
Science Center

SC5345.AR

4.0 MILLIMETER WAVE ABSORPTION AND REFRACTION IN
TUNGSTEN BRONZE FERROELECTRICS

Millimeter wave absorption and refraction in tungsten bronze ferroelectrics

Bradley Bobbs, Mehran Matloubian, and Harold R. Fetterman
Department of Electrical Engineering, University of California, Los Angeles, California 90024

Ratnakar R. Neurgaonkar and Warren K. Cory
Rockwell International Science Center, 1049 Camino dos Rios, Thousand Oaks, California 91360

(Received 30 January 1986; accepted for publication 21 April 1986)

Tungsten bronze ferroelectric crystals $\text{Sr}_x\text{Ba}_{1-x}\text{Nb}_2\text{O}_6$ and $\text{Ba}_{2-x}\text{Sr}_x\text{K}_{1-x}\text{Na}_x\text{Nb}_5\text{O}_{15}$ have been investigated for potential electro-optic uses at millimeter wave carrier frequencies between 55 and 110 GHz. Indices of absorption and refraction at temperatures between 20 and 300 K were derived from measurements of transmittance spectra containing Fabry-Perot fringes produced by crystal surface reflections. The anisotropies observed in both indices at these frequencies are huge compared with those at optical frequencies. Absorption in both materials decreases markedly upon cooling, but only for incident waves polarized along the crystal polar axis.

Current interest in the properties of ferroelectric materials at millimeter wave frequencies has been motivated largely by their potential for use in devices which control millimeter waves by means of linear electro-optic (Pockels) effect.¹ One of the materials with the largest electro-optic coefficients at these frequencies, $\text{Sr}_x\text{Ba}_{1-x}\text{Nb}_2\text{O}_6$ (SBN),² has large absorption losses at room temperature which limit its usefulness in practical devices. Large absorption has also been observed in another promising ferroelectric in tungsten bronze family, $\text{Ba}_{2-x}\text{Sr}_x\text{K}_{1-x}\text{Na}_x\text{Nb}_5\text{O}_{15}$ (BSKNN).³ A study of the temperature dependence of the properties of these crystals is of interest both because of the possibilities of improved utility when they are cooled and because an understanding of the absorption mechanisms may aid in the development of lower loss crystals. The present study of millimeter wave refraction and absorption has revealed some interesting phenomena which have not been predicted or completely explained by current ferroelectric models.

Transmittance or reflectance spectra over a full millimeter wave band may be measured for small samples with high dielectric constant by means of a spectrophotometer system shown schematically in Fig. 1(a). The frequency of the narrowband output of a backward wave oscillator is stepped across the full band by a computer which also records and ratios the transmitted, reflected, and incident powers measured by thermistor-type detectors. The data were normalized using the transmittance spectrum without a sample and the reflectance spectrum of a metal plate. The sample is mounted so that two parallel surfaces are in contact with standard waveguide flanges and fully cover the waveguide openings, with pressure maintained by small springs. This simple and convenient mounting technique has been shown to allow accurate measurements of sufficiently thin samples⁴ without the complications of sample preparations for mounting inside a waveguide.⁵ Free-space mounting, which has been used at submillimeter wavelengths,⁶ would present severe diffraction problems for small samples at millimeter wavelengths. The use of single mode hollow metal rectangular waveguide throughout maintains the linearly polarized TE_{10} mode everywhere except possibly inside the sample. The isolators and 3 dB directional coupler serve to eliminate extraneous standing waves.

The apparatus is extended to low-temperature measurement by means of the sample mounting arrangement shown

schematically in Fig. 1(b). One of the waveguide flanges contacting the sample is soldered to a copper block attached to a closed cycle helium refrigerator unit. The unit is inside a mechanically pumped vacuum chamber to prevent vapor condensation and heat convection. Thin polyethylene vacuum windows are placed between metal waveguide sections cut approximately at the Brewster angle for the linearly polarized radiation, to minimize reflections which cause extraneous standing waves. A barrier to heat conduction along the waveguides is provided by sections of solid Teflon rectangular waveguide which slide inside the metal waveguide. A two-step transition from hollow metal to Teflon-filled metal to Teflon alone is made by a pyramidal Teflon taper and a metal horn, with low reflection and absorption losses.⁷ In this configuration the lowest sample temperature achievable is about 20 K. A heater and diode temperature sensor are mounted on the copper block and connected to a computer-interfaced controller to allow stabilization at any temperature up to 270 K.

A sample with a large millimeter wave refractive index will have large reflections off its entrance and exit faces which form Fabry-Perot interference fringes in the spectrum. The "optical" constants n and k (real and negative imaginary parts respectively of the complex refractive index) of the sample may then be determined by comparison of the experimental spectrum with theoretical Fabry-Perot spectra which assume negligible dispersion of n and k over the spectrum. The theory uses Fresnel reflection coefficients for the air-dielectric interfaces, where the index in air is modified by the change in phase velocity produced by the presence of the metal waveguide walls.⁸ This modification results in a nonmonotonic variation of peak height with frequency.

An example of a theoretical fit is shown as the dashed line in Fig. 2. The solid line shows combined data over two millimeter wave bands for BSKNN #1 (a composition having a Curie temperature of 476 K) at 40 K. The crystal is oriented so that its polar axis (the c axis in these materials) is parallel to the radiation electric field. The data have been digitally smoothed to remove high-frequency oscillations which are not noise, but are completely reproducible, and are apparently caused by diffraction effects which are not included in the plane wave theory. These oscillations are ignored in determining the theoretical fit. The validity of this

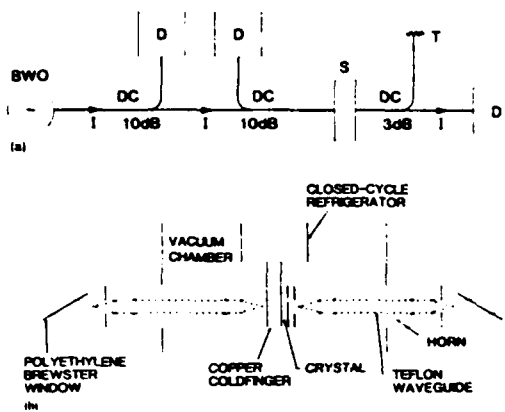


FIG. 1. (a) Millimeter wave transmittance and reflectance spectrum apparatus, showing backward wave oscillator (BWO), ferrite isolators (I), directional couplers (DC), detectors (D), sample (S), and matched termination (T). (b) Sample mounting for low-temperature measurements.

approximation has been demonstrated by the agreement obtained between optical constants measured from different thicknesses of the same material.

Measurements were made on samples of SBN with composition parameter $x = 0.61$, having a Curie temperature of $T_c = 345$ K, and on two different compositions of BSKNN with $T_c = 476$ K (#1) and $T_c = 443$ K (#2). Good theoretical fits were obtained by assuming constant values of n and k over the spectrum. Lower uncertainties were obtained from the transmittance than from the reflectance spectra. The uncertainties in n ranged from around $\pm 1\%$ for low absorption cases up to $\pm 10\%$ for high absorption cases where the Fabry-Perot fringes have poor contrast. Uncertainties for k were around twice that for n .

The measured values of n and k for several temperatures between room temperature and 20 K are plotted in Figs. 3(a) and 3(b) respectively for both c axis (millimeter wave electric field parallel to crystal polar axis) and a axis (field perpendicular to polar axis) geometries. A remarkable feature of these plots is the enormous anisotropies in both absorption and refraction. Upon cooling there is a dramatic

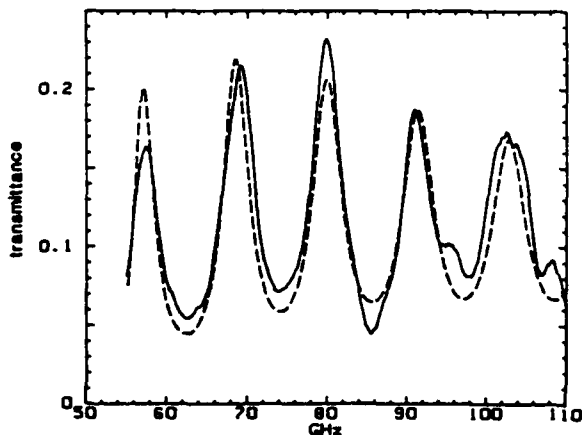


FIG. 2. Experimental spectrum (solid line) and theoretical fit (dashed line) for BSKNN #1 c axis at 40 K. Sample thickness is 0.241 cm.

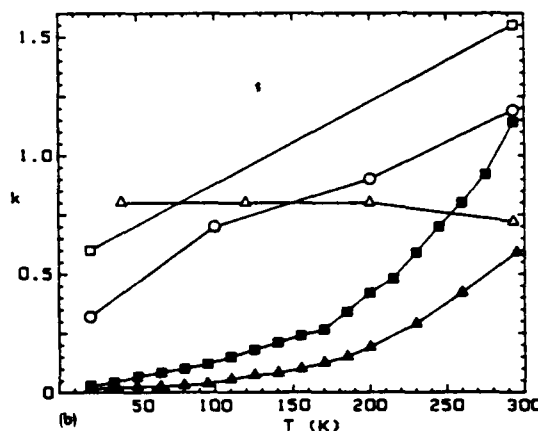
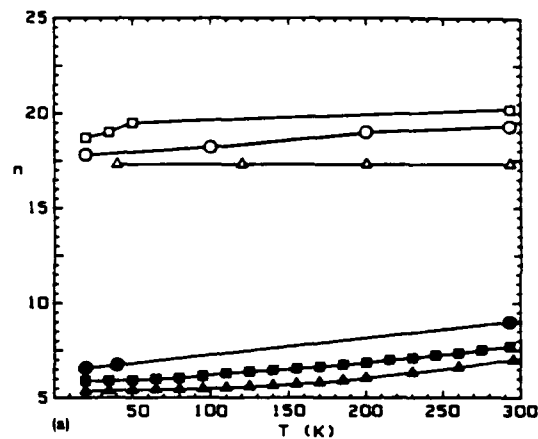


FIG. 3. Results of measurements on SBN (circles), BSKNN #1 (triangles), and BSKNN #2 (squares) for c axis (solid symbols) and a axis (open symbols) geometries: (a) temperature dependence of n , showing huge birefringence; (b) temperature dependence of k , showing large decrease upon cooling for c axis only. Minimum values are 0.016 (BSKNN #1) and 0.03 (BSKNN #2). For the SBN c axis, k decreases from around 4 at 293 K to 0.08 at 20 K.

decrease in absorption, qualitatively similar to that observed in LiTaO_3 at 890 GHz by Fetterman *et al.*,⁸ but only for the c axis. These crystals thus become millimeter wave polarizers at low temperatures, a fact which is especially interesting when one considers how rare crystals are, such as herapathite (used in Polaroid sheets) or tourmaline, which polarize visible light by absorption. It is noted that low absorption is achieved for the geometry which has been shown to give the largest electro-optic effect for visible waves in SBN.⁹ Extremely large millimeter wave birefringence as observed in the tungsten bronzes has also been reported for BaTiO_3 .¹⁰ However, this is not a general property of ferroelectrics, as the birefringence of LiNbO_3 and LiTaO_3 is much smaller.¹¹

Since the current level of understanding of the lattice dynamics of tungsten bronzes is inadequate to permit an accurate description of the mechanisms leading to the observed millimeter wave properties, the interpretation of our experimental results is presently limited to qualitative discussion. The strong decrease in absorption along the c axis upon cooling suggests that the dominant absorption mechanism is the excitation of the ferroelectric soft mode. As the

temperature decreases (further away from T_c), the resonant frequency of this mode increases and so moves further away from the measurement frequencies. Relaxation effects related to the structural disorder inherent in tungsten bronzes could also have a contribution,¹² but may be frozen out at these high frequencies. This is substantiated by the observed lack of strong dispersion across the spectrum. Single phonon absorption of radiation by the soft mode should be allowed by selection rules only for polarizations with a component along the c axis, which lacks a perpendicular reflection symmetry plane. Multiphonon absorption may be significant for both c axis and a axis geometries, and this also leads to a decrease in absorption with temperature as phonon concentrations decrease. However, these considerations do not account for the experimental observation that the a axis absorption exceeds the c axis absorption.

One possible mechanism to account for the observed absorption anisotropy involves coupling of the radiation to small oscillations in the orientations of the NbO_6 distorted octahedral configurations contained within the tungsten bronze crystal structure. Such coupling could occur if the spontaneous polarization of these somewhat disordered crystals is localized within the octahedral units, such as would be the case in a ferroelectric glass.¹³ Using a simple classical model,¹⁴ the magnitude of the oscillations, and hence of the contribution to the complex dielectric constant, is found to be proportional to the sine of the angle between the polarization axis of an octahedron and the millimeter wave electric field. For the c axis geometry this angle is close to zero, so that the effect is minimized; whereas for the a axis geometry the angle is close to 90° , maximizing the effect and thereby possibly accounting for the observed increase in both absorption and refraction for this geometry.

The substantial reduction of millimeter wave absorption upon cooling these materials greatly improves their potential for low-loss applications. Furthermore, the observed sensitivity of the absorption to composition in BSKNN suggests that compositional variation can lead to additional improvement. The outlook for millimeter wave devices using cooled tungsten bronze family ferroelectric crystals is therefore quite promising.

This work was supported in part by the Office of Naval Research and by the Air Force Office of Scientific Research. The authors gratefully acknowledge valuable suggestions by R. A. Satten and by W. W. Ho.

¹M. B. Klein, in *Infrared and Millimeter Waves*, edited by K. Button (Academic, New York, 1983), Vol. 9, pp. 123-175.

²W. Ho, W. F. Hall, R. R. Neurgaonkar, R. E. DeWames, and T. C. Lim, *Ferroelectrics* 38, 833 (1981).

³W. W. Ho, W. F. Hall, and R. R. Neurgaonkar, *Ferroelectrics* 50, 325 (1983).

⁴D. Rytz, M. B. Klein, B. Bobbs, M. Matloubian, and H. R. Fetterman, *Proceedings of 6th International Meeting on Ferroelectricity*, Kobe, Japan, 1985, paper IMF-6.

⁵W. B. Bridges, M. B. Klein, and E. Schweig, *IEEE Trans. Microwave Theory Tech.* MTT-30, 468 (1982).

⁶A. A. Volkov, G. V. Kozlov, and S. P. Lebedev, *Sov. Phys. JETP* 52, 722 (1980).

⁷J. A. How, F. Leuterer, and M. Tutter, *Int. J. Infrared Millimeter Waves* 4, 343 (1983).

⁸H. R. Fetterman, C. Hu, W. E. Barch, and C. O. Parker, *Lincoln Lab. Q. Tech. Summary Rept.*, June, 1975, pp. 30-33.

⁹P. V. Lenzo, E. G. Spencer, and A. A. Ballman, *Appl. Phys. Lett.* 11, 23 (1967).

¹⁰T. S. Benedict and J. L. Durand, *Phys. Rev.* 109, 1091 (1958).

¹¹M. B. Klein, *Int. J. Infrared Millimeter Waves* 2, 239 (1981).

¹²M. E. Lines and A. E. Glass, *Principles and Applications of Ferroelectrics and Related Materials* (Clarendon, Oxford, 1977), pp. 280-292.

¹³M. E. Lines, *Phys. Rev. B* 15, 388 (1977).

¹⁴M. Born, *Optik* (Edwards Brothers, Ann Arbor, 1943), p. 561.



Rockwell International
Science Center

SC5345.AR

5.0 FERROELECTRIC PROPERTIES OF La^{3+} -MODIFIED SBN:60
SINGLE CRYSTALS



Rockwell International
Science Center

SC5345.AR

FERROELECTRIC PROPERTIES OF LANTHANUM - MODIFIED

$\text{Sr}_{0.6}\text{Ba}_{0.4}\text{Nb}_2\text{O}_6$ SINGLE CRYSTALS

R.R. Neurgaonkar, J.R. Oliver, W.K. Cory

Rockwell International Science Center
Thousand Oaks, CA 91360

and

L.E. Cross

Materials Research Laboratory
The Pennsylvania State University
University Park, PA 16802

ABSTRACT

The role of La^{3+} in tungsten bronze $\text{Sr}_{0.6}\text{Ba}_{0.4}\text{Nb}_2\text{O}_6$ (SBN:60) ferroelectric crystals has been studied with respect to Czochralski crystal growth parameters and fundamental ferroelectric properties. Direct substitution of La^{3+} for Sr^{2+} or Ba^{2+} results in a significant decrease of the ferroelectric phase transition temperature and, consequently, dramatic increases in the room temperature dielectric constant and pyroelectric coefficient along the polar axis. Although La-modified SBN:60 is more difficult to grow, it was possible to grow defect-free crystal boules up to 2 cm diameter with optical quality, striation-free crystals found for lanthanum modifications up to 1.0 mole %.

INTRODUCTION

Tungsten bronze solid solution crystals such as $\text{Sr}_{1-x}\text{Ba}_x\text{Nb}_2\text{O}_6$ (SBN), either doped or undoped, have proven to be excellent materials for various applications such as guided wave optics,¹ photorefractive,²⁻⁷ millimeter wave⁸⁻¹⁰ and pyroelectric^{11,12} device applications. Tetragonal (4mm) bronze crystals, such as SBN, exhibit excellent transverse



ferroelectric and optical properties in contrast to perovskite $BaTiO_3$ crystals which show strong longitudinal optical properties. Figure 1 shows the classification of the various types of tungsten bronze crystals based on their crystal structure and ferroelectric and optical properties. Included among these are important bronzes such as SBN, BSKNN, KLN, SKN, morphotropic PBN, SNN and SCNN^{13,14} all of which have potential utility in millimeter wave and optical applications, although high-quality crystal growth has proven to be difficult in some instances.

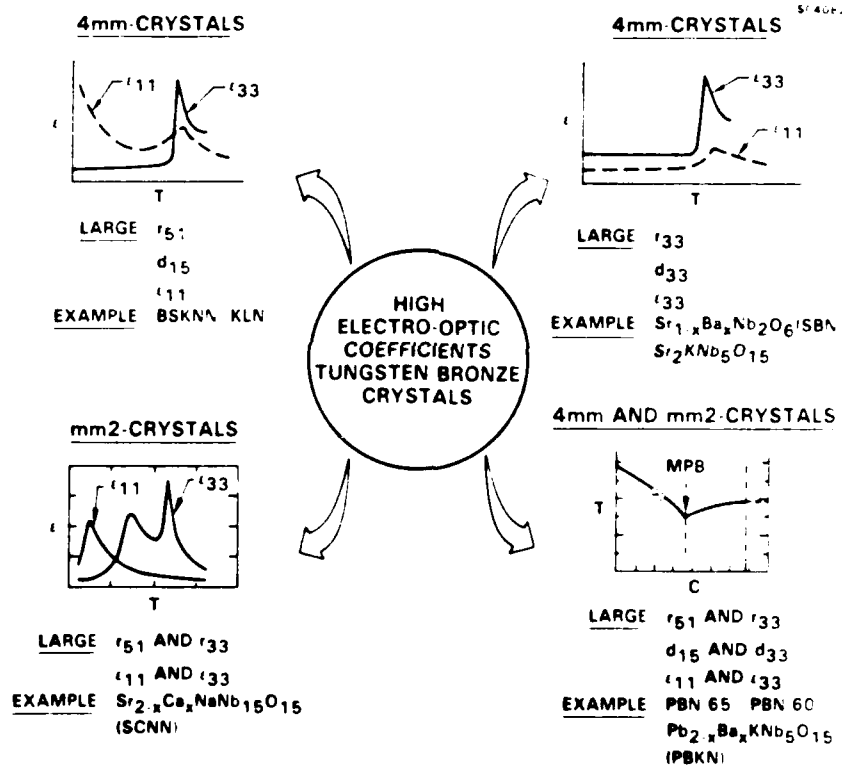


Fig. 1 Classification of tungsten bronze ferroelectric crystals.

The present paper focuses on modified versions of the congruently melting¹⁵ $Sr_{0.6}Ba_{0.4}Nb_2O_6$ (SBN:60) crystal composition with La^{3+} substituting for Sr^{2+} or Ba^{2+} in the crystal lattice. Previous work by Liu and Maciolek¹¹ has shown that rare earth-modified $Sr_{0.5}Ba_{0.5}Nb_2O_6$ (SBN:50) results in a lowered ferroelectric phase transition temperature and thereby improved pyroelectric properties. However, SBN:50 is an incongruently melting



bronze composition which is difficult to grow in bulk single crystal form, particularly with good optical quality. SBN:60, on the other hand, can be grown with excellent optical quality^{14,16} and therefore presents the opportunity to grow modified crystals of comparable high quality for potential millimeter wave, optical and pyroelectric applications.

Experimental

1. The SBN:60 - M³⁺NbO₄ System

Modified forms of SBN were initially studied using sintered ceramic samples. For convenience, modifications of the composition SBN:50 were examined because of its higher phase transition temperature (~ 120°C vs 75°C for SBN:60). Reagent grade BaCO₃, SrCO₃, Nb₂O₅ and La₂O₃ or Y₂O₃ oxide powders were used for these ceramics, with the thoroughly mixed materials calcined at 1000°C, ball-milled in acetone, and then cold-pressed and sintered at 1350°C for 4 hours. Rare earth modifications of Sr_{0.75}Ba_{0.25}Nb₂O₆ (SBN:75) and SBN:60 ceramic compositions were also checked for solid solubility and structure using x-ray diffraction measurements.

Since lanthanum and yttrium exist in trivalent states, modifications of SBN:50 were attempted in the following manner:

1. $Sr_{0.5-x}M^3_xBa_{0.5}Nb_2O_{6+x}$
2. $Sr_{0.5-3x}La_{2x}Ba_{0.5}Nb_2O_6$

M = La or Y

where ... represents a lattice site vacancy. Equivalent substitutions for Ba²⁺ were also examined. The phase diagram for La-modification is illustrated in Fig. 2; x-ray analysis showed that the solubility limit for these modifications of SBN is upwards of 20 mole %.

Figure 3 shows the room temperature dielectric constant at 1 kHz for two types of SBN:50 ceramic modifications using La³⁺; similar results were obtained for Y³⁺ modifications. Only the type Sr_{0.5-x}La_xBa_{0.5}Nb₂O_{6+x} modification resulted in significant changes in the dielectric constant with increasing La³⁺ or Y³⁺ substitution, this being a



SC41530

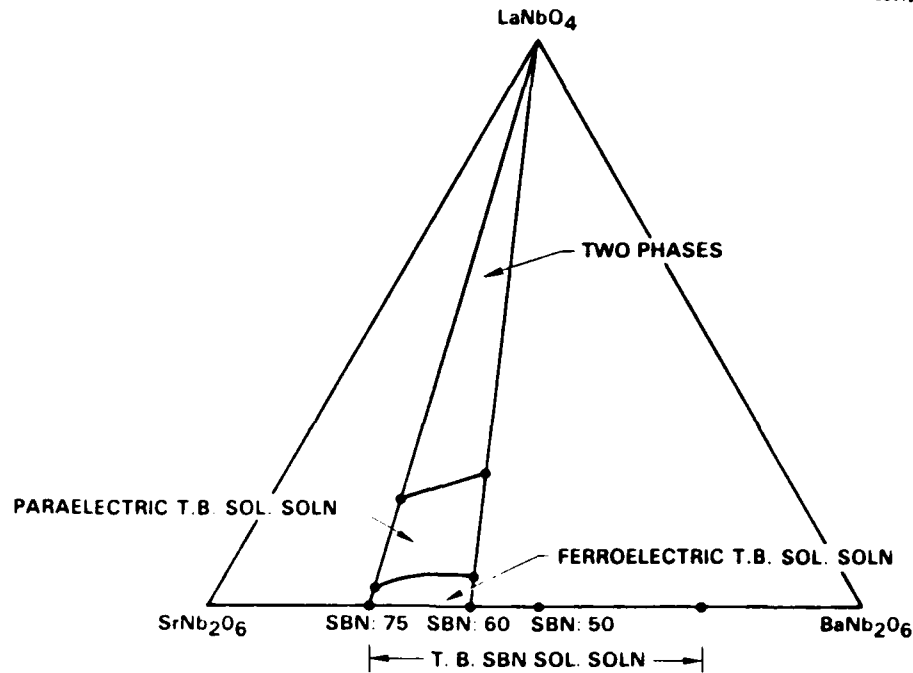
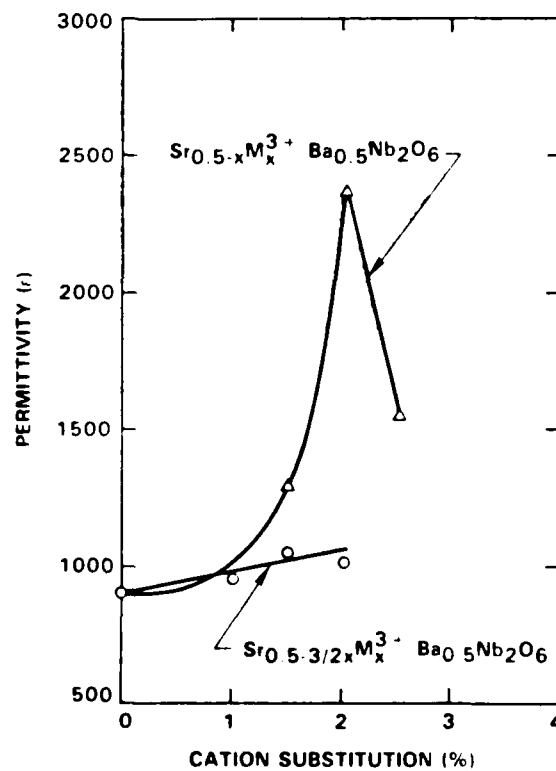


Fig. 2 Ternary phase diagram for the SrNb_2O_6 - BaNb_2O_6 - LaNbO_4 solid solution system.



SC85 33521

Fig. 3

Room temperature dielectric constant for La-modified SBN:50 ceramics.



consequence of a lower ferroelectric phase transition temperature. Equivalent results were also obtained with rare earth substitutions for Ba^{2+} . Hence, only type 1 modifications were used in subsequent crystal growth work with SBN:60. Since Sr^{2+} and La^{3+} have similar cationic sizes, Czochralski crystal growth was attempted for La-modified SBN:60 to avoid potential growth problems which might arise from dissimilar size cations in the same crystallographic site.

2. Growth of La-Modified SBN:60 Single Crystals

Because of extensive prior experience in the Czochralski crystal growth of congruently melting SBN:60¹⁷, the growth of La-modified SBN:60 proceeded without undue difficulty. A $\text{Sr}_{0.5-x}\text{La}_x\text{Ba}_{0.5}\text{Nb}_2\text{O}_6$ substitution of La^{3+} for Sr^{2+} was used (type 1 modification), with concentrations varying from 0.5 to 2.0 mole %. High purity starting materials were used exclusively for these growths with the calcined materials thoroughly ball-milled in acetone prior to melting in a 5 cm diameter, 5 cm height platinum crucible. All crystal growths were performed in an RF induction heated furnace operating at 370 kHz.

The incorporation of La^{3+} in the SBN crystal lattice did not cause major changes in the growth conditions. Czochralski growth was performed along the c-axis ($\langle 001 \rangle$) using an automatic diameter control system (proven mandatory for high-quality tungsten bronze crystal growth) and an after-heater geometry. Initially, c-axis SBN:60 crystal seeds were used until La-modified crystals became adequate for use in subsequent growths. Bulk fracture was an early problem in these growths, probably as a result of the multiple site preference of La^{3+} in the 15-, 12- and 9-fold coordinated oxygen octahedra sites of the SBN lattice. This problem was overcome in part by maintaining strictly constant cooling rates after crystal growth.

Figure 4 shows examples of unmodified and La-modified SBN:60 crystal boules. Modified crystals were successfully grown up to 2 cm in diameter. A striking feature of these crystals, common to other tungsten bronzes, is the presence of large natural facets. La-modified SBN:60 boules grow with 24 natural facets, similar to unmodified crystals, with the crystal cross-section becoming more rectangular with increasing lanthanum modification and featuring large $\langle 100 \rangle$ and $\langle 010 \rangle$ facets, as seen in Fig. 4. A rectangular growth habit is not uncommon to crystals in the tungsten bronze family; for example, larger unit cell bronzes such as $\text{Ba}_{2-x}\text{Sr}_x\text{K}_{1-y}\text{Na}_y\text{Nb}_5\text{O}_{15}$ (BSKNN) and KLN typically grow in a rectan-



SC5345.AR

SC44292

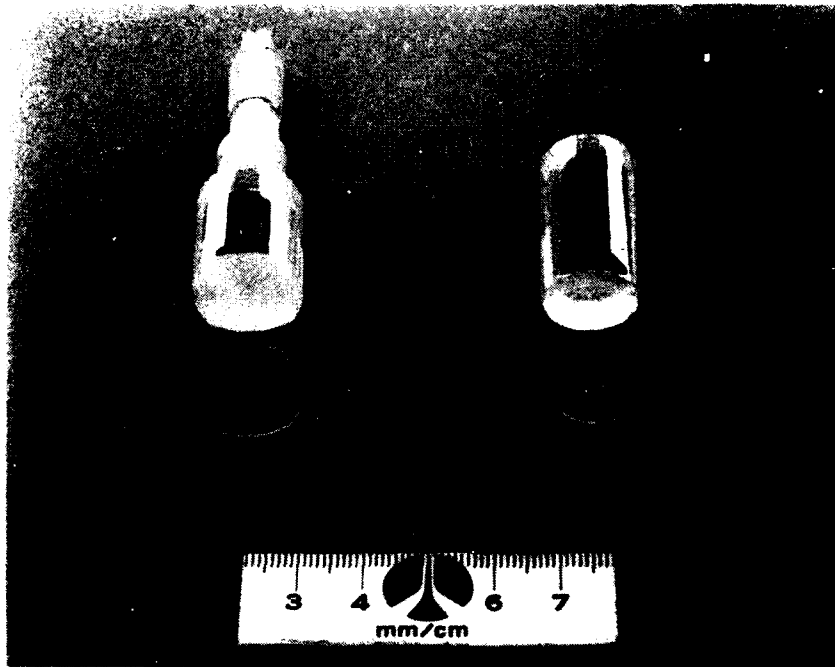


Fig. 4 La-modified (left) and unmodified (right) SBN:60 crystal boules grown by the Czochralski technique.

gular shape with 8 well-defined facets.¹⁶ What is unusual about La-modified SBN:60 crystals is that the crystal unit cell does not change markedly with increasing lanthanum content; for example, a 1.0 mole % La-modified crystal has unit cell dimensions of $a, b = 12.466\text{\AA}$, $c = 3.930\text{\AA}$ compared to $a, b = 12.465\text{\AA}$, $c = 3.935\text{\AA}$ for unmodified SBN:60. Hence, the gradual change in growth habit from a circular to a more rectangular shape with La modification may be a result of the partial occupancy of the otherwise empty 9-fold coordinated lattice site.

Table I summarizes the major crystal growth parameters and physical properties of these crystals. Crystal growth beyond 2 mole % modification was not attempted since we wished to maintain a ferroelectric phase at room temperature. Furthermore, the more heavily modified compositions showed major optical striations and were very difficult to grow. Nevertheless, it would be interesting to examine crystals with heavier La modifications since such paraelectric ($4/mmm$) crystals should have large quadratic electro-optic and possibly large electrostrictive properties.



Table I
Growth Conditions and Properties for Pure and La³⁺ Modified
SBN:60 Crystals

| | SBN:60 | SBN:60/La (1 mole % La) | SBN:60/La (1.5 mole % La) |
|-------------------------|-----------------|-------------------------------|-------------------------------|
| Crystal Symmetry @ 20°C | 4 mm | 4 mm | 4 mm |
| Growth Temperature | 1480°C | 1480°C | 1475°C |
| Pulling Rate (mm/h) | 10 | 9 | 6-7 |
| Interface | Smooth and flat | Rough but nearly flat | Rough and concave |
| Quality | Optical | Optical | Weak striations |
| Growth Habit | Circular | Near-circular | Squarish |
| Number of Facets | 24 Facets | 24 Facets, (100) prominent | 24 Facets, (100) prominent |
| Color | Pale cream | Pale cream | Pale cream |

3. Ferroelectric Properties

The polar c-axis dielectric properties for a poled, 1 mole % La-modified SBN:60 crystal are shown as a function of temperature in Fig. 5. Like unmodified SBN crystals, the polar axis dielectric constant is characterized by a large dielectric anomaly at the ferroelectric phase transition temperature (Curie point), above which the dielectric constant follows a Curie-Weiss law,

$$\epsilon_{33} = \frac{C_3}{(T - \theta_3)} \quad (1)$$

where $C_3 = 4.3 \times 10^5$ and $\theta_3 = 38^\circ\text{C}$. The Curie constant, C_3 , remains remarkably unchanged with La substitution up to 2 mole %, with the only change occurring in the Curie temperature, θ_3 , which is 75°C in unmodified SBN:60. The drop in θ_3 with La substitution is nearly linear at approximately $36^\circ\text{C}/\text{mole } \%$, so that for a 1.5 mole % substitution, θ_3 occurs at room temperature.

As evident in Fig. 5, SBN:60/La shows a strong frequency dependence for the polar axis dielectric constant near the phase transition. Because of this relaxor behavior, the temperature of the dielectric maximum, T_c , varies with frequency from $34\text{-}42^\circ\text{C}$ over a 100 Hz - 100 kHz range, for a 1 mole % La substitution, so that the specification of T_c loses some of its meaning. Relaxor behavior has also been found in unmodified SBN:60,¹⁰ but the

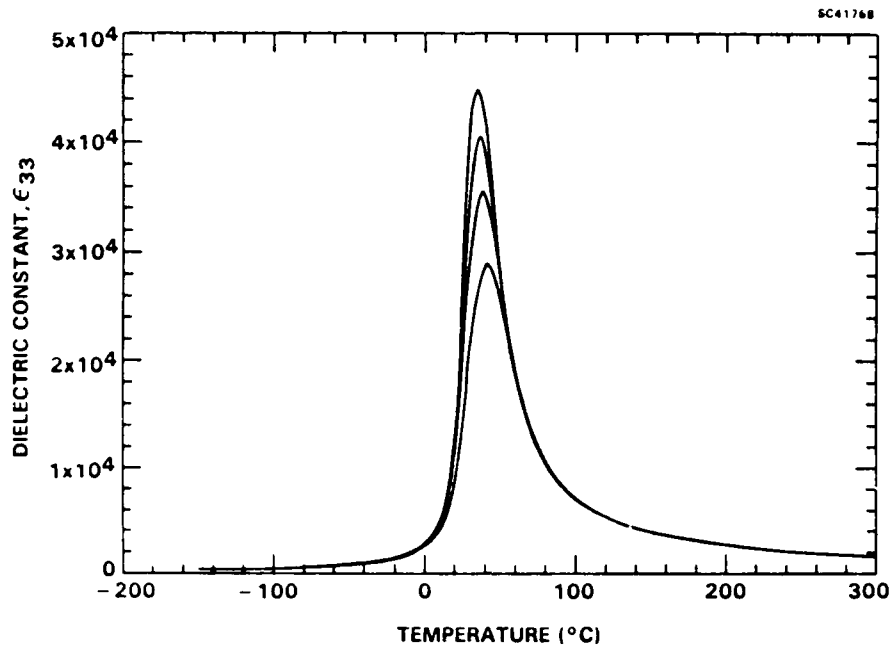


Fig. 5 Polar axis dielectric constant for a poled, 1.0 mole % La-modified SBN:60 crystal at 100 Hz (upper curve), 1.0 kHz, 10 kHz and 100 kHz (lower curve).

effects are much less pronounced than those in Fig. 5. This behavior in SBN:60 is felt to arise from the lattice site uncertainty of the Sr^{2+} and Ba^{2+} ions between the 15- and 12-fold coordinated oxygen octahedra sites of the partially empty lattice, leading to a distribution of phase transition temperatures in the crystal bulk. In the present case of La substitution, this site uncertainty extends to the 9-fold coordinated site as well, so that more pronounced relaxor effects would be expected.

Because of the lowered phase transition temperature and increased relaxor effects, the room temperature polar axis dielectric constant for 1 mole % La-substituted SBN:60 is very large at 9600-7000, depending on frequency. These values are roughly an order of magnitude larger than the nearly dispersionless value of 920 for unmodified crystals. The corresponding room temperature dielectric loss tangent varies from 0.01 to 0.07 in poled crystals, about a factor of five greater than for unmodified SBN:60 but still reasonable in light of the close proximity of the phase transition temperature. For 1.5 mole % La substitution, the relaxor effects become very pronounced, with $\epsilon_{33} = 36000-21000$ and $\tan \delta = 0.05-0.28$.



Crystal poling was found to be straightforward, with a 5 kV/cm dc poling field being sufficient to pole the crystals at room temperature to a single ferroelectric domain. No advantages were found by poling from the phase transition temperature down to room temperature. The coercive field necessary to initiate ferroelectric domain reversal at room temperature was relatively low at 1-2 kV/cm, a factor for consideration in potential device applications.

The nonpolar a-axis dielectric constant, ϵ_{11} , for a 1 mole % La-modified SBN:60 crystal is shown as a function of temperature in Fig. 6. The dielectric anomaly near 40°C is typical of SBN:60 crystals and arises from the onset of nonzero spontaneous polarization along the c-axis.¹⁶ As a result, some frequency dispersion is observed near the peak, but the effect is generally minimal. The a-axis constant follows a Curie-Weiss law above the phase transition temperature, with $C_1 = 2.1 \times 10^5$ and $\theta_1 = -265^\circ \pm 20^\circ\text{C}$. As in the c-axis case, C_1 is essentially the same as for unmodified SBN:60, with only θ_1 varying downward from -245°C with increasing La substitution. At room temperature, $\theta = 640$ for 1 mole % La modification, increasing to 700 for 1.5 mole % crystals. The corresponding dielectric loss tangents are low (0.012 or less) and are nearly independent of frequency.

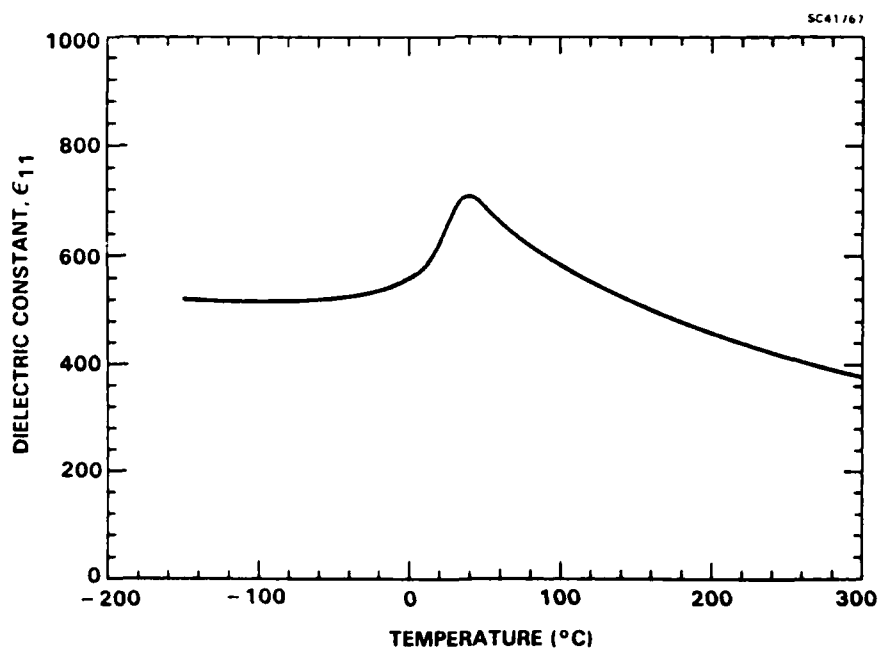


Fig. 6 Nonpolar a-axis dielectric constant for 1.0 mole % La-modified SBN:60 at 10 kHz. Data at other frequencies are substantially the same.



The net spontaneous polarization along the c-axis, P_3 , was measured by integrating the charge released during warming at a uniform rate ($2^\circ\text{C}/\text{min}$) under zero bias conditions.¹² The results for 1 mole % La substituted SBN:60 are shown in Fig. 7 along with the pyroelectric coefficient, $p = -dP_3/dT$. As in the case for the dielectric properties, the polarization and the pyroelectric coefficient behave in a manner similar to that for unmodified SBN:60, differing only in an overall temperature shift of the characteristics due to the change in θ_3 and a slight broadening of the pyroelectric peak near the phase transition. The pyroelectric maximum occurs at 27°C , 11° below θ_3 , compared to the 8° separation typical of unmodified SBN:60 crystals; this downward shift from θ_3 is a consequence of the diffuse nature of the ferroelectric transition.

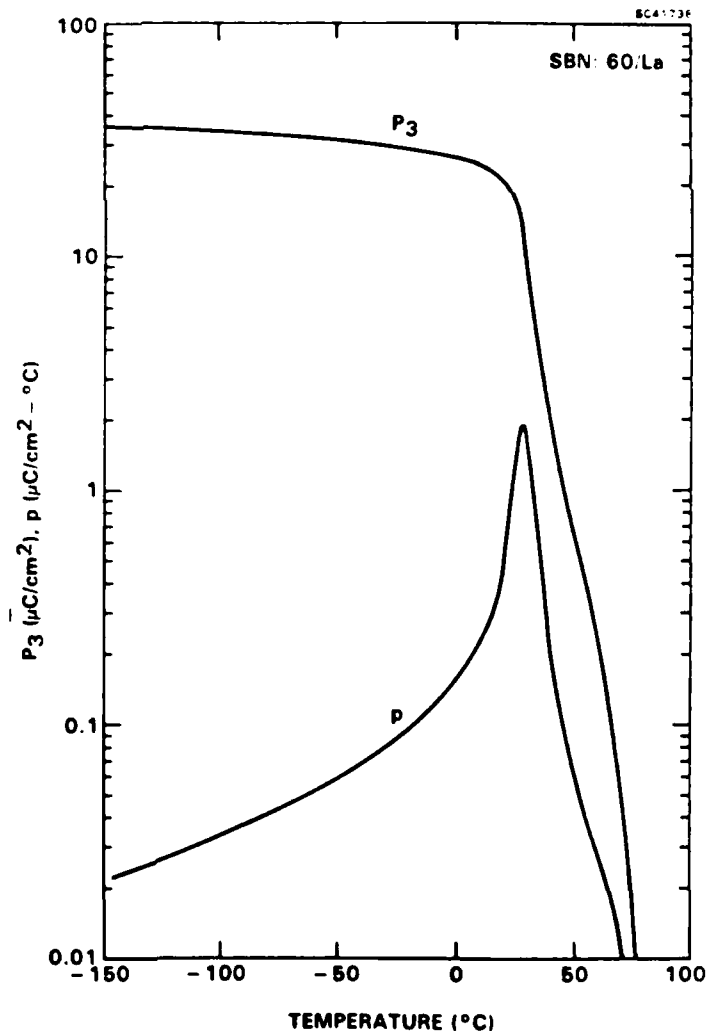


Fig. 7

Polarization, P_3 , and the pyroelectric coefficient, p , for 1.0 mole % La-modified SBN:60.



The room temperature values of the spontaneous polarization and the pyroelectric coefficient are summarized in Table 2 along with other ferroelectric data for unmodified, 1 mole % and 1.5 mole % La-modified SBN:60 crystals. The changes in these parameters with composition, as well as the changes in the dielectric properties, are essentially reflections of the changes in the Curie temperature. For example, in the particular case of 1.5 mole % La modification, the very low polarization and large ϵ_{33} are due to the occurrence of the phase transition close to room temperature; consequently, these parameters are also extremely sensitive to small temperature changes.

Table 2
Ferroelectric Properties

| | SBN:60 | SBN:60/La (1.0 mole % La) | SBN:60/La (1.5 mole % La) |
|---|---------------------|------------------------------|------------------------------|
| Curie Point, T_c (°C)* | 73-74 | 34-42 | 17-28 |
| θ_3 (°C) | 75 | 38 | 22 |
| C_3 (°C) | 4.1×10^5 | 4.3×10^5 | 4.3×10^5 |
| θ_1 (°C) | $-245 \pm 20^\circ$ | $-265 \pm 20^\circ$ | $-275 \pm 20^\circ$ |
| C_1 (°C) | 2.05×10^5 | 2.1×10^5 | 2.1×10^5 |
| ϵ_{33} (@ 1 kHz) | 920 | 8800 | 30,000 |
| ϵ_{11} (@ 1 kHz) | 485 | 640 | 700 |
| P_3 ($\mu\text{C}/\text{cm}^2$) | 30.2 | 21.1 | 3.4 |
| p ($\mu\text{C}/\text{cm}^2\text{-}^\circ\text{C}$) | 0.10 | 0.62 | 0.95 |
| E-O coeff., r_{33} ** (10^{-12} m/V) | 440 | 2960 | 1620 |

All values are at 20°C unless otherwise indicated.

*Over range 100 Hz-100 kHz.

**Calculated values (see text).



DISCUSSION

It is worthwhile to examine the potential utility of La-modified SBN:60 crystals in potential device applications. For pyroelectric detector considerations, the decrease of the phase transition temperature with La-modification crystals necessarily increases both the polar axis dielectric constant and the pyroelectric coefficient at room temperature, as shown in Table 2, so that the longitudinal pyroelectric device figure-of-merit, p/ϵ_{33} , actually declines with increasing La substitution. However, in transverse pyroelectric detector configurations where a low detector impedance (high capacitance) is desirable, La-modified SBN:60 is clearly superior to unmodified SBN:60 because of the higher dielectric constant and pyroelectric coefficient available.

The large increase in the room temperature dielectric constant over unmodified SBN:60 is also significant for electro-optical or nonlinear optical applications. From the phenomenology developed for tetragonal tungsten bronze ferroelectrics¹⁸, the linear electro-optic coefficient, r_{33} , is given by

$$r_{33} = 2g_{33}P_3\epsilon_0\epsilon_{33} \quad (2)$$

where g_{33} is the quadratic electro-optic coefficient and ϵ_0 is the permittivity of free space. In the particular case of La-modified SBN:60, the enhancement of r_{33} due to the dramatic increase of ϵ_{33} at room temperature is partially offset by a corresponding decrease in the spontaneous polarization. Nevertheless, the calculated r_{33} for 1.0 mole % La modification, using $g_{33} = 0.10 \text{ m}^4/\text{C}^2$ typical of bronze ferroelectrics, is $3290 \times 10^{-12} \text{ m/V}$ at 1 kHz compared to $460 \times 10^{-12} \text{ m/V}$ (470×10^{-12} , measured) for unmodified SBN:60. The lower value of $1800 \times 10^{-12} \text{ m/V}$ for 1.5 mole % modification in Table 2 results from the substantial decline in the spontaneous polarization at the room temperature ferroelectric phase transition. In this case, it is also difficult to maintain a single ferroelectric domain unless a dc bias field is maintained on the crystal; this would also serve to substantially increase P_3 , and therefore, r_{33} .

The large pyroelectric and electro-optic coefficients for La-modified SBN:60 crystals make these very attractive materials for infrared focal plane array, millimeter wave, electro-optic and nonlinear optical applications. Although heavily modified crystals (≥ 1.5 mole %) have prominent optical striations, more lightly modified crystals have



excellent optical quality and can maintain a single ferroelectric domain, after poling, for an indefinite period of time below 35°C. Lanthanum modifications greater than 1.5 mole % result in crystals which are paraelectric at room temperature, which may be of interest for very low loss, biased pyroelectric detectors or for electrostrictive applications; quadratic electro-optic applications, however, would necessarily require further improvements in crystal optical quality.

ACKNOWLEDGMENTS

This work was supported by DARPA (Contract No. N00014-82-C-2246) and by the Office of Naval Research (Contract No. N00014-81-C-0463).

REFERENCES

1. O. Eknayan, C.H. Bulmer, H.F. Taylor, W.K. Burns, A.S. Greenblatt, L.A. Beach and R.R. Neurgaonkar, *Appl. Phys. Lett.* 48, 13 (1986).
2. G.J. Salamo, M.J. Miller, E.J. Sharp, G.L. Wood and W.W. Clark III, *Opt. Comm.* 59, 417 (1986).
3. E.J. Sharp, M.J. Miller, G.L. Wood, W.K. Clark III, G.J. Salamo and R.R. Neurgaonkar, *Proc. 6th IEEE Int'l Symp. on Applications of Ferroelectrics (ISAF)*, 51 (1986).
4. G.E. Rakuljic, A. Yariv and R.R. Neurgaonkar, *Appl. Phys. Lett.* 50, 10 (1987).
5. M.J. Miller, E.J. Sharp, G.L. Wood, W.W. Clark III, G.J. Salamo and R.R. Neurgaonkar, *Opt. Lett.* 12, 340 (1987).
6. J. Rodriguez, A. Siahmakoun, G. Salamo, M.J. Miller, W.W. Clark III, G.L. Wood, E.J. Sharp and R.R. Neurgaonkar, *Appl. Optics*, 26(9), 1732 (1987).



7. M.D. Ewbank, R.R. Neurgaonkar, W.K. Cory and J. Feinberg, Appl. Phys. Lett. 62(2), 374 (1987).
8. B. Bobbs, M. Matloubin, H.R. Fetterman, R.R. Neurgaonkar and W.K. Cory, Appl. Phys. Lett. 48, 1642 (1986).
9. W.W. Ho, W.F. Hall and R.R. Neurgaonkar, Ferroelectrics, 56, 230 (1984).
10. R.R. Neurgaonkar, W.W. Ho, W.K. Cory, W.F. Hall and L.E. Cross, Ferroelectrics, 51, 185 (1984).
11. S.T. Liu and R.B. Maciolek, J. Electron. Mat. 4, 91 (1975).
12. A.M. Glass, J. Appl. Phys. 40, 4699 (1969).
13. J.R. Oliver, G. Shoop and R.R. Neurgaonkar, Proc. 6th IEEE Int'l Symp. on Applications of Ferroelectrics (ISAF), 485 (1987).
14. R.R. Neurgaonkar and W.K. Cory, J. Opt. Soc. Am. B3, 274 (1986).
15. K. Megumi, N. Nagatsuma, K. Kashiwada and Y. Furuhashi, Mat. Sci. 11, 1583 (1976).
16. R.R. Neurgaonkar and W.K. Cory, J. Opt. Soc. Am. B3, 274 (1986).
17. R.R. Neurgaonkar, W.K. Cory and J.R. Oliver, Ferroelectrics 35, 301 (1983).
18. M. DiDomenico and S.H. Wemple, J. Appl. Phys. 40(2), 720 (1969).



Rockwell International
Science Center

SC5345.AR

6.0 GROWTH OF PEROVSKITE PZT AND PLZT THIN FILMS



Rockwell International
Science Center

SC5345.AR

GROWTH OF PEROVSKITE PZT AND PLZT THIN FILMS

R.R. Neurgaonkar, I. Santha, J.R. Oliver and E.T. Wu
Rockwell International Science Center
Thousand Oaks, CA 91360

and

L.E. Cross
Pennsylvania State University
University Park, PA 16802

ABSTRACT

This paper reports preliminary results on the fabrication of perovskite PZT and PLZT thin films using a sputtering technique. For glass, quartz and sapphire substrates, it was necessary to raise the substrate temperature above 550°C to achieve perovskite tetragonal structures of interest. Growth at temperatures below 550°C yielded a major pyrochlore structure phase. Excess of PbO in target was also required to maintain stoichiometry in these films.



INTRODUCTION

Recently, considerable attention has focused on the development of low-loss ferroelectric thin films for optical waveguides. Several attempts have been made to grow single crystal waveguide films using materials such as LiNbO_3 ,¹⁻³ PLZT,⁴⁻⁶ KLN and SBN.^{7,8} More recently, other ferroelectric materials such as BaTiO_3 and PBN have been considered using semiconductor substrates for various optical applications, including waveguides, spatial light modulators, switches and pyroelectric detectors. The top surfaces of as-grown LiNbO_3 and SBN films fabricated by liquid phase epitaxial growth, chemical vapor deposition, melting methods and so on, are relatively rough so that they must be optically polished to couple a light beam into the film. On the other hand, polishing is not necessary for sputtered thin films. Therefore, the sputtering technique has been used in the present work to develop perovskite PZT and PLZT films using a variety of substrates such as glass, quartz and sapphire. This paper reports the growth of PZT and PLZT films and their associated growth problems.

EXPERIMENTAL PROCEDURE

The sputtering targets employed were a mixture of PZT or PLZT and PbO . Approximately 5 mole% excess PbO was added in these targets to control the Pb concentration in the films. The targets were prepared using ceramic sintering or hot pressing; well-mixed powders were cold pressed and then sintered or hot pressed at 1100°C after ball-milling.

Sapphire (Al_2O_3) and quartz (SiO_2) substrates were first etched by sputtering. The substrates were mounted on a heating block with a stainless steel mask of 0.2 mm thickness. Substrate temperature was monitored by a Pt-Pt.Rh 13% thermocouple inserted into the center of the substrate holder. The sputtering conditions, summarized in Table I for each material, are as follows:

| | |
|----------------------------|---|
| Target-Substrate Distance: | 5 cm |
| Input Power Density | 1.9 to 2.4 W/cm^2 |
| Sputtering Gas | $\text{Ar}:\text{O}_2$ (40:60 or 50:50) |



Gas Pressure 8-12 μ m
 Substrate Temperature 300-600°C
 Deposition Rate 20-25Å/h
 Annealing Temperature 700-800°C

Table I
 Growth Condition for PZT and PLZT Films

| Substrate | Substrate Temperature s 550°C - 600°C | | Atmosphere | Power Density (W/cm ²) | Film Thickness (μ m) | Remarks |
|--|---|------------|-----------------------------|---------------------------------------|------------------------------|--------------------|
| PZT Films | | | | | | |
| Glass | Pyrochlore | Perovskite | 50% Ar + 50% O ₂ | 2.2-2.4 | 1-5 | |
| Quartz (SiO ₂) | Pyrochlore | Perovskite | 50% Ar + 50% O ₂ | 2.2-2.4 | 3-10 | Excellent Films |
| Sapphire (Al ₂ O ₃) | Pyrochlore | Perovskite | 50% Ar + 50% O ₂ | 2.2-2.4 | 3-10 | Reasonable Quality |
| PLZT Films | | | | | | |
| Glass | Pyrochlore | Perovskite | 40% Ar + 60% O ₂ | 1.9-2.1 | 3-10 | Reasonable Quality |
| Quartz (SiO ₂) | Pyrochlore | Perovskite | 40% Ar + 60% O ₂ | 1.9-2.1 | 2-8 | Excellent Quality |
| Sapphire (Al ₂ O ₃) | Pyrochlore | Perovskite | 40% Ar + 60% O ₂ | 1.9-2.1 | 2-5 | Reasonable Quality |

EXPERIMENTAL RESULTS AND DISCUSSION

PZT and PLZT compositions have been of practical interest for the last 25 years and are being exploited for optical applications such as switches, modulators, image storage and optical display devices. PZT occurs on the pseudobinary PbZrO₃-PbTiO₃ system and exhibits a morphotropic phase boundary at a Zr:Ti ratio of 52:48, as shown in Fig. 1. However, the development of bulk single crystals has been hindered by growth problems associated with Pb²⁺ losses during growth and cracking when cycling through the paraelectric/ferroelectric phase transition. For this reason, thin-film growth of these compositions is now being explored in several countries.⁹⁻¹¹

The deposition of PZT and PLZT films by the sputtering technique has shown that the structure of the film is sensitive to the substrate temperature (Fig. 2). PZT or PLZT thin films having a pyrochlore structure were obtained below 550°C, whereas a perovskite structure was obtained above 600°C. However, traces of PbTi₃O₇ were observed with Pb²⁺ deficiencies, and for this reason, an extra 5 mole% PbO was incorporated in the targets to stabilize the film composition.

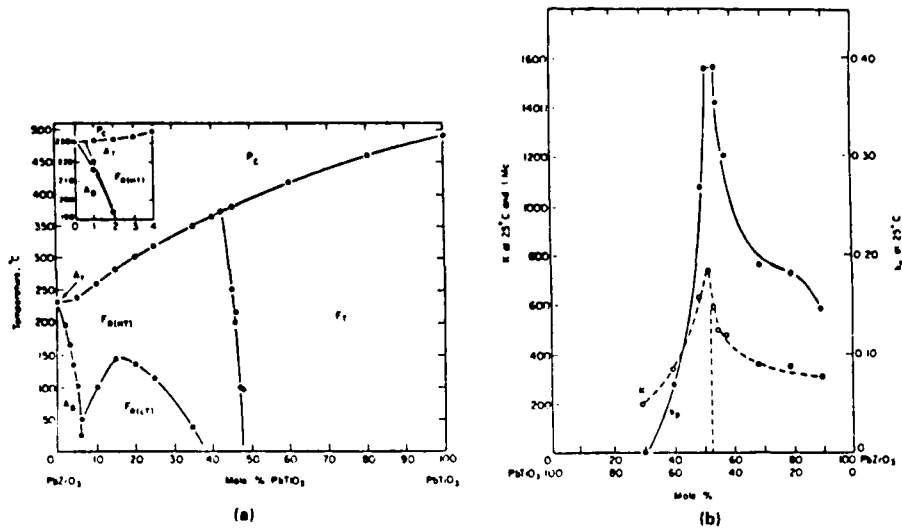


Fig. 1 Morphotropic phase boundary in the PZT system.

Fig. 2

Structural sensitivity of
PZT and PLZT compositions.

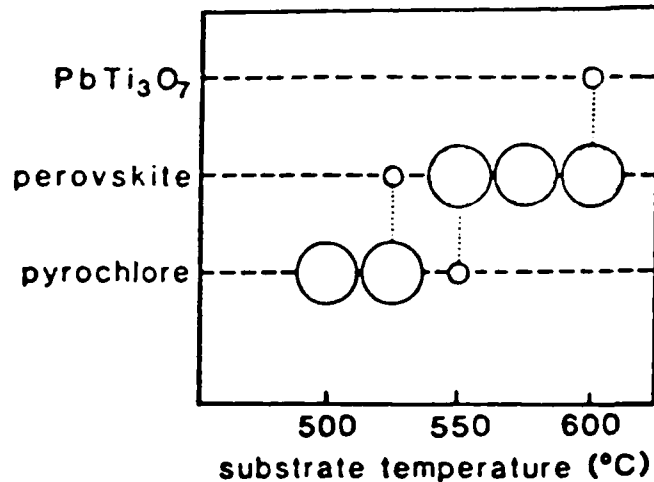


Figure 3 shows the x-ray diffraction patterns of PLZT films sputtered on fused quartz and sapphire and for a PLZT(9/65/35) hot-pressed ceramic. In Fig. 3, (a) is for a film (~ 4 μm thickness) sputtered at a substrate temperature of 550°C with a target containing 5 mole% of PbO excess, (b) is for a film sputtered at 600°C with a target containing 3 mole% PbO excess, and (c) is for the hot-pressed PLZT ceramic target. The good agreement between the thin film and ceramic target patterns shows that the films have maintained the desired perovskite structure, although they are polycrystalline due to the



poor lattice match with the substrates. A small split of the (200) peak into (200) and (002) was observed after a post-growth anneal at 700°C/2 h, indicating a tetragonal symmetry. However, this caused some loss of Pb^{2+} , as indicated by the appearance of small second phase peaks associated with ZrO_2 . To maintain a perovskite phase during growth, substrates were held at 600–650°C; growth temperatures below 350°C resulted in completely amorphous films which could not be annealed to a crystalline form. Although excess PbO is clearly required to maintain film stoichiometry during growth, based on evidence from this work and the results of others,¹ the optimum excess PbO amount still needs to be established.

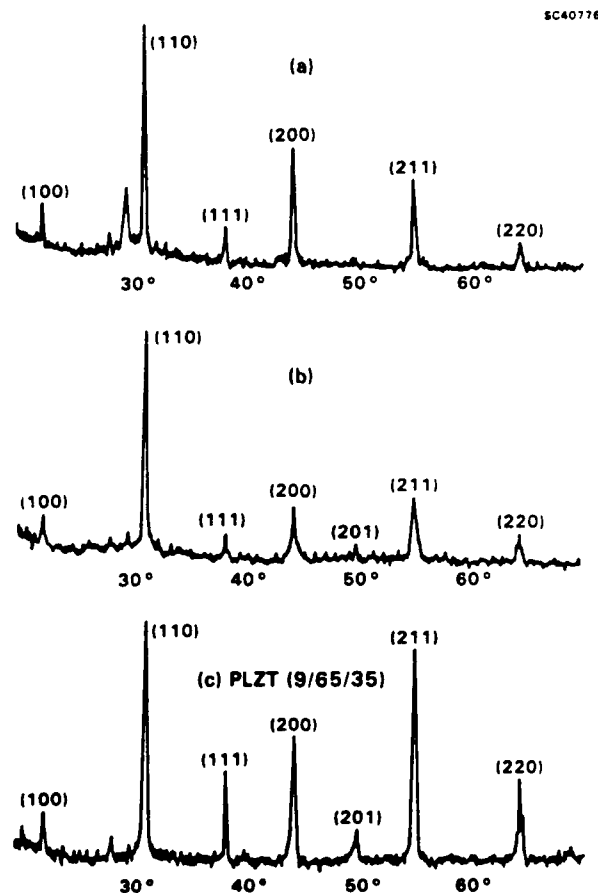


Fig. 3 X-ray diffraction patterns of PLZT sputtered films and hot-pressed ceramic. (a) Film sputtered with a target with 5 mole% excess PbO; (b) film sputtered with a target with 3 mole% excess PbO; and (c) hot-pressed ceramic.



FUTURE PLANNED WORK: MULTILAYERED FERROELECTRIC FILMS

Recent work by Higuma et al¹² has shown that the growth of PLZT single crystal films is possible using perovskite SrTiO₃ substrates at temperatures between 500 and 700°C. Although film growth was successful, there was a considerable lattice mismatch between the film and the substrate. Table 2 summarizes the lattice match of PLZT with SrTiO₃ and other ferroelectric crystals, including tungsten bronze SBN and PBN. The lattice match between PLZT and PBN is very good for (001)-oriented PBN and potentially allows the growth of better quality PLZT films. In future work, we propose to develop PZT and PLZT films as follows:

1. SBN:60 substrate with a 5 μm PBN:60 film for lattice matching to PZT or PLZT.
2. SBN:60 substrate with a 5 μm PBN:60 film and then alternate PLZT and PBN layers to develop a superlattice structure.

Table 2
Lattice Match Between PZT/PLZT and Tungsten Bronze Substrates

| Film Composition | (001)-Oriented Tungsten Bronze Substrates | | | Perovskite SrTiO ₃ |
|-----------------------|---|-------|--------|----------------------------------|
| | SBN:60 | BSKNN | PBN:60 | |
| <u>PZT (40:60)</u> | | | | |
| a = 4.042Å | 2.6% | 1.99% | 1.4% | 3.01% |
| c = 4.082Å | 3.6% | 3.00% | 3.00% | 4.12% |
| <u>PLZT (8/40/60)</u> | | | | |
| a = 4.029Å | 2.1% | 1.5% | 1.1% | 2.5% |
| c = 4.072Å | 3.4% | 2.7% | 2.1% | 4.3% |
| <u>PBN:60</u> | | | | |
| a = 12.501Å | 0.38% | 0.20% | ----- | ----- |
| c = 3.985Å | 0.65% | 0.35% | ----- | ----- |



Since the lattice mismatch between PLZT and PBN is small, we expect that optical-quality PZT/PLZT films or PLZT-PBN superlattices can be more readily achieved with these film structures. An additional advantage is the ability to improve the lattice match by adjustment of the Pb:Ba ratio in PBN and thereby improve PZT/PLZT film crystallinity.

The previously discussed considerations for the electrical evaluation of PBN:60 thin films also apply here in the case of PZT/PLZT films. Because of the additional complexity of PZT/PLZT thin-film growth, the growth of good quality films on metallized substrates may be vastly more difficult than for PBN:60. A closely spaced surface electrode configuration appears to be a preferable geometry for electrical characterization of PZT/PLZT films, at least in the near term. A high-temperature sample holder to accommodate this type of geometry for dc conductivity, pyroelectric and dielectric measurements over a wide temperature range is now being designed and tested for this purpose.

ACKNOWLEDGEMENT

This work was supported by the AFOSR (Contract No. F49620-86-C-0052) and ONR (Contract No. N00014-81-C-0463). The authors are grateful for the discussions on this research with W.F. Hall and T. McGill (Caltech).

REFERENCES

1. A. Okada, J. Appl. Phys. Lett 48, 2905 (1977).
2. M. Ishida, S. Tsuji, K. Kimura, H. Matsunami and T. Tanaka, J. Cryst. Growth 45, 393 (1978).
3. M. Adachi, T. Shiosaka and A. Kawabata, Ferroelectrics 27, 89 (1980).



4. Y. Higuma, K. Tanaka, T. Nagawa, T. Kariya and Y. Hamakawa, Jap. J. Appl. Phys. 16, 1707 (1977).
5. M. Ishida, T. tsuji, K. Kimura, H. Matsunami and T. Tanaka, J. Cryst. Growth 45, 383 (1978).
6. H. Adachi, T. Kawaguchi, K. Setsune, K. Ohji and K. Wasa, Appl. Phys. Lett. 42, 867 (1983).
7. T. Shiosaki, M. Adachi and A. Kawabata, Thin Solid Films 96, 129 (1982).
8. R.R. Neurgaonkar and E.T. Wu, Mat. Res. Bull. 22(8), 1095 (1987).
9. C.A.T. Salama and E. Siciunas, J. Vac. Sci. and Tech. 9, 91 (1971).
10. T. Nagamoto, T. Kosaka, S. Omori and O. Omoto, Ferroelectrics 37, 681 (1981).
11. S. Iida and S. Kataoka, Appl. Phys. Lett. 18, 391 (1971).
12. Y. Higuma, K. Tanaka, T. Nagawa, T. Kariya and Y. Hamakawa, Jap. J. Appl. Phys. 16, 1707 (1977).



Rockwell International

Science Center

SC5345.AR

7.0 A THERMODYNAMIC PHENOMENOLOGY FOR FERROELECTRIC
TUNGSTEN BRONZE SBN:60



Rockwell International

Science Center

SC5345.AR

A THERMODYNAMIC PHENOMENOLOGY FOR FERROELECTRIC TUNGSTEN

BRONZE $\text{Sr}_{0.6}\text{Ba}_{0.4}\text{Nb}_2\text{O}_6$ (SBN:60)

J.R. Oliver and R.R. Neurgaonkar

Rockwell International Science Center
Thousand Oaks, CA 91360 USA

and

L.E. Cross

Materials Research Laboratory
The Pennsylvania State University
University Park, PA 16802 USA

ABSTRACT

The tetragonal tungsten bronze ferroelectrics in the strontium barium niobate system have been extensively studied over many years. As for many of the bronzes, a crude interpretation of the experimental data has been attempted in the past using the simple Landau-Ginsburg-Devonshire expansion of the Gibbs free energy as a Taylor series in powers of the polarization, lumping all the temperature dependence into the lowest order term. In this paper, new measurements are presented for the temperature dependence of dielectric polarization, permittivity and the E-field dependence of the permittivity. It is shown that for a realistic fitting of the data, the Taylor expansion must be taken to at least the eighth power term, and that the coefficients of terms up to the sixth power must be taken as functions of temperature. Since the phenomenology describes equilibrium behavior, it is the total static polarizability that is being explored in this treatment. The nature of this temperature dependence strongly suggests that the phase transition from a macro-polar to a macro-nonpolar state is tetracritical.



I. INTRODUCTION

Tungsten bronze ferroelectric oxides have received considerable attention for many years, with perhaps the best known of these being compositions in the $\text{Sr}_{1-x}\text{Ba}_x\text{Nb}_2\text{O}_6$ (SBN) solid solution system. Numerous applications have been realized for SBN, particularly in the areas of pyroelectric infrared detection,¹ piezoelectrics,^{2,3} electro-optics,⁴⁻⁸ and photorefractive optics,⁸⁻¹⁴ the latter resulting from the evolution of techniques for the growth of high quality single crystals in the congruently melting $\text{Sr}_{0.6}\text{Ba}_{0.4}\text{Nb}_2\text{O}_6$ (SBN:60) composition.¹⁵ As in the case for other ferroelectric materials, much of the experimental data for SBN has been interpreted on the basis of the Landau-Ginsburg-Devonshire (LGD) phenomenology, as in the extensive work by Shroud et al¹⁶ on the elastic, dielectric and piezoelectric properties of SBN:60.

With some important exceptions, nearly all of these interpretations of ferroelectric behavior have involved simple LGD expansions of the Gibbs free energy as a Taylor series in even powers of the polarization, truncated at the sixth power, with all temperature dependence carried only in the lowest order coefficient.¹⁷ This approach has proven successful for SBN:60,^{3,16} although in some instances only rough approximations of the experimental data can be obtained, as in the case of the dielectric properties.

The development of optical-quality SBN:60 crystals has made it possible to accumulate very reproducible dielectric and polarization data as a function of temperature. In this paper, we present new measurements of these properties along with measurements of the electric field dependence of the permittivity as a function of temperature. It is shown that for an accurate fitting to these data in the ferroelectric phase, the Taylor expansion of the Gibbs free energy must be taken out to at least the eighth power of the polarization, and that the coefficients of terms up to the sixth power must be taken as strong functions of temperature. Since the phenomenology describes equilibrium behavior, it is the total static polarizability, summing all possible contributions, which is being explored in this treatment.



II. THERMODYNAMIC PHENOMENOLOGY

The free-energy function of interest for a polarizable insulator is the elastic Gibbs function, given by

$$G_1 = U - TS - Xx \quad (1)$$

where U is the internal energy, T the temperature, S the entropy, X the elastic stress, and x the strain. Under the symmetry constraints of bronze ferroelectrics with a high-temperature tetragonal prototype symmetry 4/mmm, the change in free energy, ΔG_1 , due to nonzero polarization P_i may be written as a power series expansion in the P_i 's along the three principal crystallographic axes. Under isothermal conditions and zero stress, the LGD phenomenological elastic Gibbs function in the shortened matrix notation¹⁸ becomes

$$\begin{aligned} \Delta G_1 = \frac{1}{\epsilon_0} & [\alpha_1 (P_1^2 + P_2^2) + \alpha_3 P_3^2 + \alpha_{11} (P_1^4 + P_2^4) + \alpha_{12} P_1^2 P_2^2 \\ & + \alpha_{13} (P_1^2 + P_2^2) P_3^2 + \alpha_{33} P_3^4 + \alpha_{111} (P_1^6 + P_2^6) \\ & + \alpha_{112} (P_1^2 P_2^4 + P_1^4 P_2^2) + \alpha_{113} (P_1^4 + P_2^4) P_3^2 \\ & + \alpha_{133} (P_1^2 + P_2^2) P_3^4 + \alpha_{123} P_1^2 P_2^2 P_3^2 + \alpha_{333} P_3^6 \\ & + \alpha_{1111} (P_1^8 + P_2^8) + \alpha_{1122} P_1^4 P_2^4 \\ & + \alpha_{1133} (P_1^4 + P_2^4) P_3^4 + \alpha_{3333} P_3^8] \end{aligned} \quad (2)$$

where the α 's have been normalized by the free-space permittivity, ϵ_0 , for later convenience. Equation (2) differs principally from earlier treatments^{3,16} by the inclusion of terms out to the eighth power of the polarization for reasons which will become evident later.

For nonzero electric fields, E_i , we must examine the complete Gibbs function $\Delta G = \Delta G_1 - (E_1 P_1 + E_2 P_2 + E_3 P_3)$. Setting the first partial derivatives of ΔG with respect to polarization equal to zero then gives the electric field relations along the principal axes:



$$E_1 = \frac{1}{\epsilon_0} [2\alpha_1 P_1 + 4\alpha_{11} P_1^3 + 2\alpha_{12} P_1 P_2^2 + 2\alpha_{13} P_1 P_3^2 + 6\alpha_{111} P_1^5 + \alpha_{112} (2P_1 P_2^4 + 4P_1^3 P_2^2) + 4\alpha_{113} P_1^3 P_3^2 + 2\alpha_{133} P_1 P_3^4 + 2\alpha_{123} P_1 P_2^2 P_3^2 + 8\alpha_{1111} P_1^7 + 4\alpha_{1122} P_1^3 P_2^4 + 4\alpha_{1133} P_1^3 P_3^4] \quad (3)$$

$$E_3 = \frac{1}{\epsilon_0} [2\alpha_3 P_3 + 2\alpha_{13} (P_1^2 + P_2^2) P_3 + 4\alpha_{33} P_3^3 + 2\alpha_{113} (P_1^4 + P_2^4) P_3 + 4\alpha_{133} (P_1^2 + P_2^2) P_3^3 + 2\alpha_{123} P_1^2 P_2^2 P_3 + 6\alpha_{333} P_3^5 + 4\alpha_{1133} (P_1^4 + P_2^4) P_3^3 + 8\alpha_{3333} P_3^7] \quad (4)$$

The electric field expression for E_2 has been omitted since it is formally equivalent to Eq. (3) for the tetragonal symmetry assumed here.¹⁶ The solutions of these equations with $E_i = 0$ determine the normal ferroelectric states; in the case of tetragonal bronze ferroelectrics, the 3 (or c) axis is the only spontaneously polarizable axis, so that Eqs. (3) and (4) reduce to

$$E_1 = \frac{1}{\epsilon_0} [2\alpha_1 P_1 + 4\alpha_{11} P_1^3 + 2\alpha_{13} P_1 P_3^2 + 6\alpha_{111} P_1^5 + 4\alpha_{113} P_1^3 P_3^2 + 2\alpha_{133} P_1 P_3^4 + 8\alpha_{1111} P_1^7 + 4\alpha_{1133} P_1^3 P_3^4] \quad (P_2 = 0) \quad (5)$$

$$E_3 = \frac{1}{\epsilon_0} [2\alpha_3 P_3 + 4\alpha_{33} P_3^3 + 6\alpha_{333} P_3^5 + 8\alpha_{3333} P_3^7] \quad (P_1 = P_2 = 0) \quad (6)$$



The dielectric stiffnesses, $\chi_{ii} = \epsilon_{ii}^{-1}$, are then given by

$$\begin{aligned} \chi_{11} = \epsilon_0 \frac{\partial E_1}{\partial P_1} = & 2\alpha_1 + 12\alpha_{11}P_1^2 + 2\alpha_{13}P_3^2 \\ & + 30\alpha_{111}P_1^4 + 12\alpha_{113}P_1^2P_3^2 + 2\alpha_{133}P_3^4 + 56\alpha_{1111}P_1^6 \\ & + 12\alpha_{1133}P_1^2P_3^4 \quad (P_2 = 0) \end{aligned} \quad (7)$$

or

$$\chi_{11} = 2\alpha_1 + 2\alpha_{13}P_3^2 + 2\alpha_{133}P_3^4 \quad (P_1 = P_2 = 0) \quad (7a)$$

and

$$\begin{aligned} \chi_{33} = \epsilon_0 \frac{\partial E_3}{\partial P_3} = & 2\alpha_3 + 12\alpha_{33}P_3^2 + 30\alpha_{333}P_3^4 + 56\alpha_{3333}P_3^6 \\ & (P_1 = P_2 = 0) \end{aligned} \quad (8)$$

At temperatures well above the ferroelectric Curie point, T_c , $P_3 = 0$ under zero bias conditions and the paraelectric stiffnesses generally follow a linear Curie-Weiss behavior of the form

$$\chi_{11} = 2\alpha_1 = \frac{(T - \theta_1)}{C_1} \quad (T > T_c) \quad (9)$$

$$\chi_{33} = 2\alpha_3 = \frac{(T - \theta_3)}{C_3} \quad (T > T_c) \quad (10)$$

with $\theta_1 \ll \theta_3$. For a first-order phase transition, $\theta_3 < T_c$, whereas for a second-order transition, $\theta_3 = T_c$ under ideal conditions.^{17,19}

Generally, there are no restrictions on the temperature dependence of the higher order Devonshire coefficients α_{ij} , α_{ij} , α_{ijj} , etc., and indeed for cases such as BaTiO₃ some temperature dependence has been found.²⁰ However, in most treatments of ferroelectric materials, the higher order coefficients are assumed to be temperature-invariant, at least over a limited range below T_c , and reasonably good fits to dielectric and spontaneous



polarization data can be obtained. Nevertheless, the uniqueness of the Devonshire coefficients is necessarily determined by physically measurable parameters such as the low-frequency dielectric constant, the spontaneous polarization and the electric field which must rigorously satisfy the dielectric stiffness and electric field equations as well as other derived phenomenological relations. These we shall now examine on the basis of macroscopic experimental data for tungsten bronze SBN:60.

III. TUNGSTEN BRONZE SBN:60

The congruently melting SBN:60 composition is a smaller unit cell bronze with a tetragonal 4mm crystal structure at room temperature and lattice constants $a, b = 12.465\text{\AA}$ and $c = 3.935\text{\AA}$ as determined by x-ray diffraction measurements. The SBN solid solution system is represented by the formula $(A_1)_4(A_2)_2B_{10}O_{30}$ in which both the Sr^{2+} and Ba^{2+} ions occupy the 15-fold (A_1) and 12-fold (A_2) coordinated oxygen octahedra sites.^{21,22} Since only 5/6 of these sites are occupied, SBN is referred to as an unfilled bronze. The high-temperature prototype symmetry is tetragonal 4/mmm, placing SBN in the Shuvalov ferroelectric species 4/mmm(1)D4F4mm.²³

The SBN:60 solid solution crystals examined were grown by the Czochralski technique^{15,24,25} using an automatic-diameter control system to facilitate tight compositional control and high optical quality during bulk crystal growth. Further details may be found in previous papers.^{6,8,12} Over 100 growths have now been performed in the SBN system, including undoped and doped crystals (Ce, La, Fe, etc.), and crystal quality has evolved to the point where c-axis boules up to 4 cm diameter are now routinely grown free of detectable imperfections and major optical striations. These crystals have been of sufficiently high optical quality to permit extensive optical measurements such as two- and four-wave mixing and self-pumped phase conjugation.⁸⁻¹⁴

A photograph of a typical SBN:60 crystal boule is shown in Fig. 1. A general characteristic of tungsten bronze crystals is the presence of major facets parallel to the growth axis; in the particular case of SBN:60 c-axis growths, there are 24 facets, including (100), (010), (110), etc., a feature which significantly eases the task of crystal orientation and cutting.



SC5345.AR

SC44291

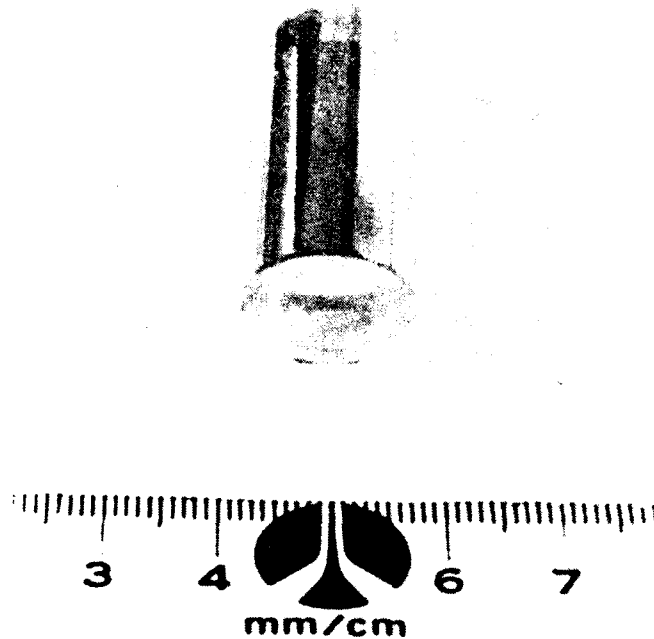


Fig. 1 Czochralski-grown SBN:60 bulk single crystals.

IV. EXPERIMENTAL METHOD

The two principal crystallographic axes of interest in SBN:60 are the a or b axes ($\langle 100 \rangle$ or $\langle 010 \rangle$) and the polar c-axis ($\langle 001 \rangle$). Crystal wafers in these orientations were cut with a diamond saw and then mechanically lapped and, in some instances, additionally polished to an optical finish. The latter step was not found to be particularly necessary for electrical measurements, however, as long as the contacts were annealed. We have used sputtered Pt or Au full-area contacts almost exclusively in our measurements, and although other materials (such as Al) and contact forming methods (such as fired pastes) are viable alternatives, sputtered noble metal contacts have been found more stable at elevated temperatures and yield highly reproducible electrical measurement data.

Contacted crystal samples were generally annealed in a dry oxygen atmosphere at 450-550°C for 1-3 h prior to measurement. Although the crystal boules undergo a post-growth anneal at 1300-1400°C, the second low-temperature anneal establishes a good interface between the contact metallization and the crystal surface, and helps to minimize surface conductivity along the unmetallized edges. Surface damage due to cutting,



polishing and metal deposition appears to be minimized at these relatively low temperatures, and residual internal stress is probably also reduced.

The measurement apparatus for dielectric, conductivity and polarization measurements consisted of a fully shielded alumina sample mount enclosed in an environmentally sealed alumina chamber. Electrical contact with the test samples was established by small Pt pads which lightly pressed against a portion of the contact metallization using an adjustable spring-loaded alumina rod. Details of the design are given in the paper by Morin et al;²⁶ the apparatus in its present configuration represents evolutionary refinements of the original design. Sample temperature control was facilitated by a Kanthal-wound tube furnace, with temperatures below room temperature achieved by spraying liquid nitrogen onto the sample chamber wall. N₂ gas was used in the chamber below 0°C and O₂ above at a ~ 2 psi positive pressure to maintain a dry environment.

All dielectric measurements were made with a calibrated HP4274A bridge covering the frequency range of 100 Hz-100 kHz. DC currents were measured with a Keithley 619 electrometer. All data acquisition, process control and data analysis were facilitated by a HP9816 desktop computer using an IEEE-488 interface bus.

V. POLAR AXIS PROPERTIES

The bronze solid solution system $\text{Sr}_{1-x}\text{Ba}_x\text{Nb}_2\text{O}_6$, $0.25 \leq x \leq 0.75$, is characterized by a large dielectric anomaly along the polar c-axis at the paraelectric/ferroelectric phase transition temperature, T_c . An example is shown in Fig. 2 for the weak-field c-axis dielectric constant, ϵ_{33} , as a function of temperature for an SBN:60 crystal poled to a single ferroelectric domain. A recurring feature of SBN is the significant dielectric dispersion which appears within a 10-15° range of T_c (~ 75°C), as shown in Fig. 2. This Debye-type relaxation behavior is why SBN solid solution crystals are generally referred to as relaxor ferroelectrics. This behavior is postulated to occur because of the distribution of phase transition temperatures in the bulk of the crystal arising from the site uncertainty of the Sr²⁺ and Ba²⁺ ions in the partially filled lattice. Further evidence for this postulate is provided by comparison with "filled" bronze ferroelectrics, such as $\text{Ba}_{2-x}\text{Sr}_x\text{K}_{1-y}\text{Na}_y\text{Nb}_5\text{O}_{15}$ (BSKNN),¹⁴ where relaxor behavior is greatly diminished.

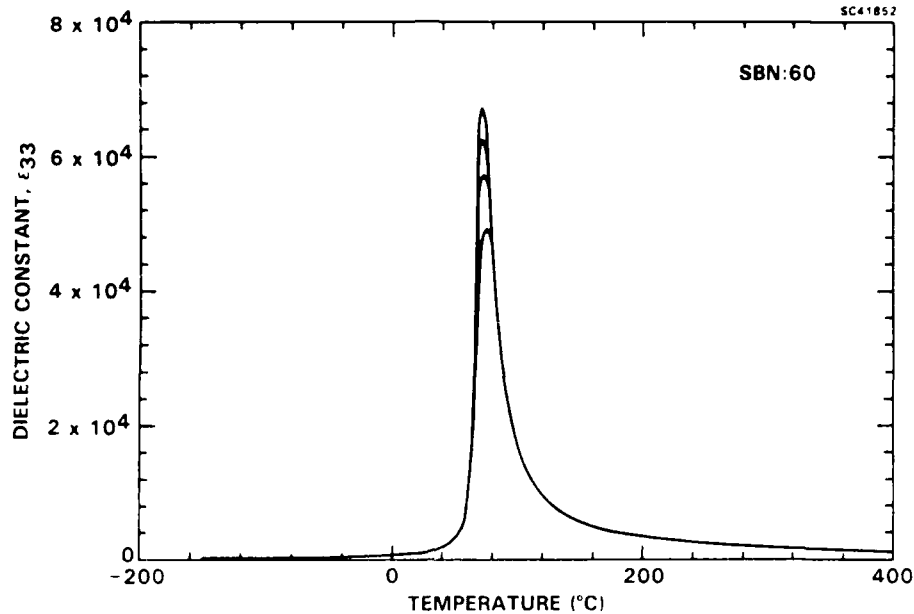


Fig. 2 Polar axis dielectric constant for a poled SBN:60 crystal at 100 Hz (highest curve), 1 kHz, 10 kHz and 100 kHz (lowest curve). $T_c = 73 - 76^\circ\text{C}$, depending on frequency.

For temperatures approximately 20° or more on either side of T_c , the dielectric dispersion is small (typically $< 2\%$ from 100 Hz-100 kHz), as is the dielectric loss ($\tan\delta$ typically 0.007 or less at 20°C , and less than 0.001 at 120°C). Room-temperature dark dc conductivity is also very small, typically $10^{-15} \Omega^{-1}\text{-cm}^{-1}$ or less, and can be measured only under absolutely stable temperature conditions because of the large pyroelectric currents which can otherwise occur.

SBN:60 crystals which have been thermally depoled by warming well above 100°C show the same low dielectric dispersion and loss above T_c , but very large dispersion and loss ($\tan\delta = 0.10\text{-}0.25$ at 20°C) which persist well below 0°C . The substantial differences between the poled and depoled ac conductivities are shown in the Arrhenius plots of Fig. 3 at 100 Hz and 10 kHz. The higher conductivities and large dielectric dispersion for depoled crystals are felt to arise primarily from antiparallel domain wall relaxation²⁷ which progressively freezes out at lower temperatures. A curiosity of SBN compositions is that at low temperatures, typically below -100°C , the antiparallel ferroelectric domains of a depoled crystal effectively clamp the crystal, resulting in a nearly dispersionless dielectric constant which is less than that for a normally poled crystal.

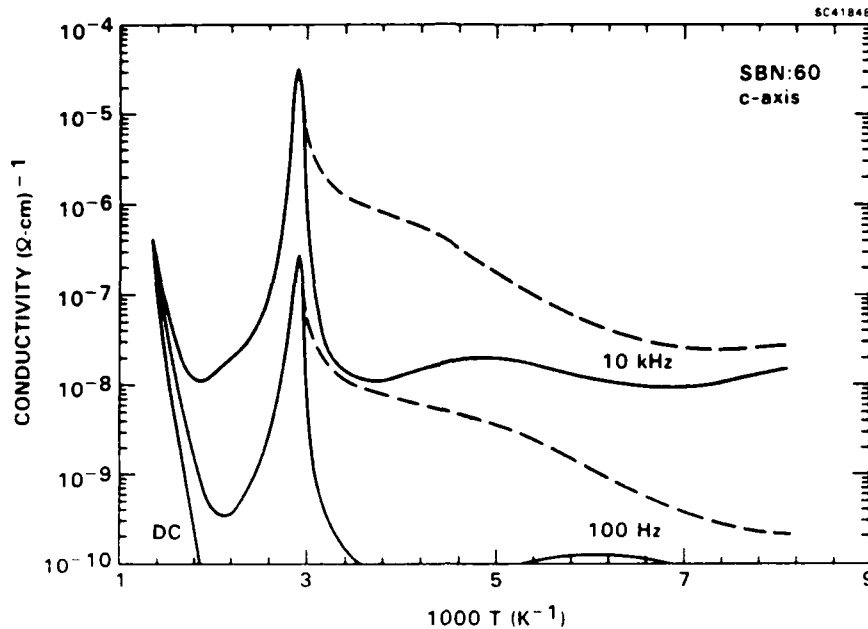


Fig. 3 Arrhenius plots of the polar axis conductivity of SBN:60 at dc, 100 Hz and 10 kHz. The dashed lines are for a thermally depoled crystal; the solid lines are for the same crystal in a poled condition.

SBN:60 may be poled to a single ferroelectric domain by applying a 5-10 kV/cm dc field along the polar c-axis at room temperature. However, an initial thermally depoled condition is necessary since the inadvertent application of a reversed polarity field to a partially poled crystal can result in the formation of antipolar macrodomains which cannot be fully switched.²⁸⁻³⁰ For this work, poling was accomplished by a field-cooling method with the dc field applied from just below T_c down to room temperature or below. Although it would appear advantageous to apply a poling field well above T_c and then cool because of the distributed nature of the phase transition temperature in the crystal bulk, in practice this was found to degrade the room-temperature dielectric losses by as much as a factor of three due to space-charge effects and did not result in any significant changes of the measured polarization.

Figure 4 shows the c-axis polarization, P_3 , and the pyroelectric coefficient, p , for a poled SBN:60 crystal. These data were obtained during warming at a nominal 3°C/min rate, with other rates giving substantially the same results. The polarization was determined from the numerically integrated charge released during warming at zero bias. The pyroelectric coefficient was measured simultaneously with the polarization^{1,19} using



$$p = - \frac{dP_3}{dT} = - \frac{J_p}{r_T} \quad (11)$$

where r_T is the rate of temperature change and J_p is the measured current density. Although either form of Eq. (11) may be used to determine p , numerical differentiation of the polarization data was found less noisy since it was less affected by small fluctuations in the thermal ramp rate.

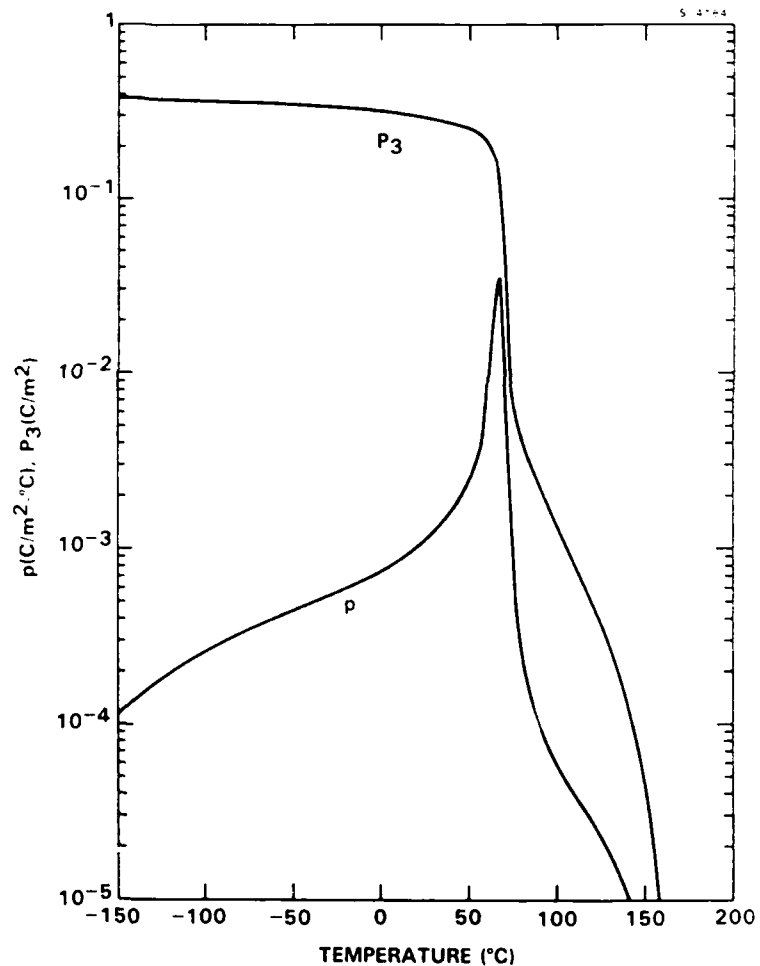


Fig. 4

The polar axis polarization, P_3 , and the pyroelectric coefficient, p , for SBN:60. The high temperature tail regions tend to vary somewhat with the poling conditions.

The pyroelectric maximum for SBN:60 occurs at 67°C (Fig. 4), roughly 8°C below T_C , and the net polarization persists well above T_C because of the distribution of phase transition temperatures; this distribution is estimated to have a Gaussian half-width of



8°C. At room temperature, $P_3 = 0.28 \text{ C/m}^2$ and $p = 9.7 \times 10^{-4} \text{ C/m}^2\text{-}^\circ\text{C}$, values which are comparable to other published results.^{1,28} Secondary pyroelectric contributions to these data due to thermal dilatation are expected to be small except very close to T_C .³¹

A. Phenomenological Fitting

From the standpoint of the thermodynamic phenomenology, it is preferable to examine the polar axis dielectric constant of SBN:60 in terms of the dielectric stiffness, $\chi_{33} = \epsilon_{33}^{-1}$, as shown in Fig. 5. The dielectric stiffness accurately follows a linear Curie-Weiss law both above and below T_C over a wide temperature range, with

$$\begin{aligned} \epsilon_{33} &= \frac{C_3}{T - \theta_3} & (T > \theta_3) \\ &= \frac{C_{3f}}{\theta_{3f} - T} & (T < \theta_{3f}) \end{aligned} \quad (12)$$

where in the paraelectric phase, $C_3 = 4.1 \times 10^5$ °C and $\theta_3 = 75$ °C, and in the ferroelectric phase, $C_{3f} = 4.5 \times 10^4$ °C and $\theta_{3f} = 69$ °C. The general behavior of the dielectric stiffness suggests a near-second-order phase transition; the fact that $\theta_{3f} \neq \theta_3 \neq T_C$ is felt to be due to the finite distribution of phase transition temperatures in SBN crystals. Indeed, for "filled" bronzes such as BSKNN, this difference amounts to at most 1-2°C.¹⁴

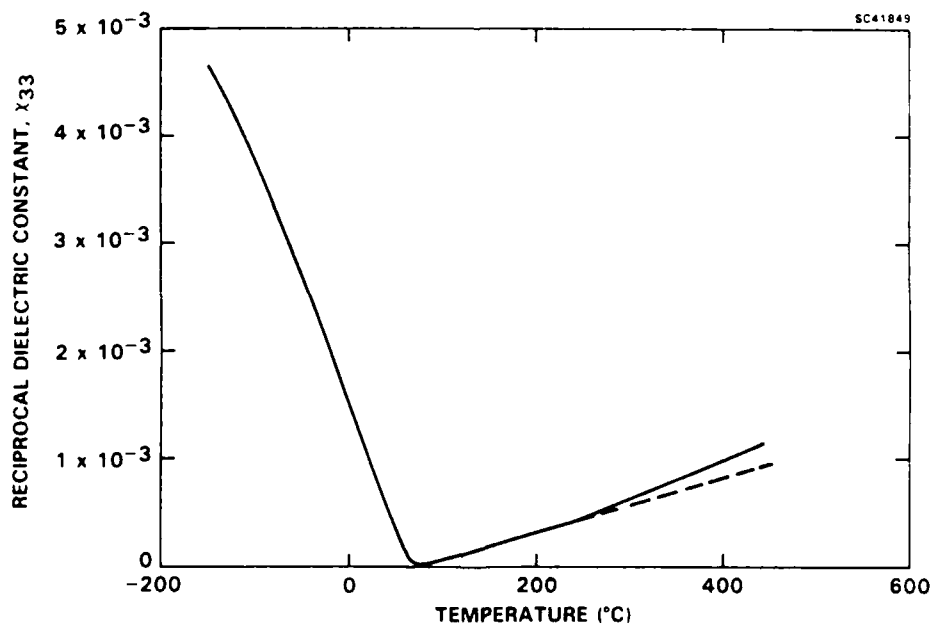


Fig. 5 The polar axis reciprocal dielectric constant at 10 kHz for poled SBN:60.



The linear behavior of the dielectric stiffness over such a wide temperature range below T_C is unusual compared to other ferroelectric materials such as LiNbO_3 and BaTiO_3 .^{19,20} A quick inspection of the electric field and dielectric stiffness expressions in Eqs. (6), (8) and (10) shows that for a stiffness expansion truncated at the fourth power of P_3 and temperature-invariant α_{33} and α_{333} , only a ~ 4:1 ratio for $C_3:C_{3f}$ is predicted in the low-temperature limit (P_3 large), compared to the ~ 9:1 ratio measured. Adiabatic vs isothermal considerations can modify the predicted results,^{17,19} but only weakly so due to the slow variation of the spontaneous polarization well below T_C .

An examination of the spontaneous polarization (Fig. 4) shows a linear temperature dependence for P_3^6 over a very wide temperature range, as shown in Fig. 6. Deviations from linearity occur only very close to T_C and at the low-temperature extreme. Formally,

$$P_3 = P_{30}(\theta_{3f}-T)^{1/6} \quad , \quad (13)$$

with $\theta_{3f} = 69^\circ\text{C}$, as before, and $P_{30} = 0.150 \text{ C/m}^2\text{-}^\circ\text{C}^{1/6}$. From Eq. (11), the pyroelectric coefficient is then

$$p = \frac{P_{30}}{6(\theta_{3f}-T)^{5/6}} = \frac{P_3}{6(\theta_{3f}-T)} \quad , \quad (14)$$

which is experimentally satisfied over an equally wide temperature range.

The temperature dependence of p in Eq. (14) may be compared with the phenomenology by taking the derivative with respect to temperature of the electric field expression in Eq. (6) under zero field conditions. For temperature-invariant higher order coefficients and α_3 defined by Eq. (10), we have

$$0 = \frac{1}{C_3} P_3 + \left[\frac{(T-\theta_3)}{C_3} + 12\alpha_{33}P_3^2 + 30\alpha_{333}P_3^4 + 56\alpha_{3333}P_3^6 \right] \frac{dP_3}{dT} \quad . \quad (15)$$

Comparing this with the dielectric stiffness expression in Eq. (8), Eq. (15) reduces to

$$p = - \frac{dP_3}{dT} = \frac{\epsilon_{33}P_3}{C_3} \quad . \quad (16)$$

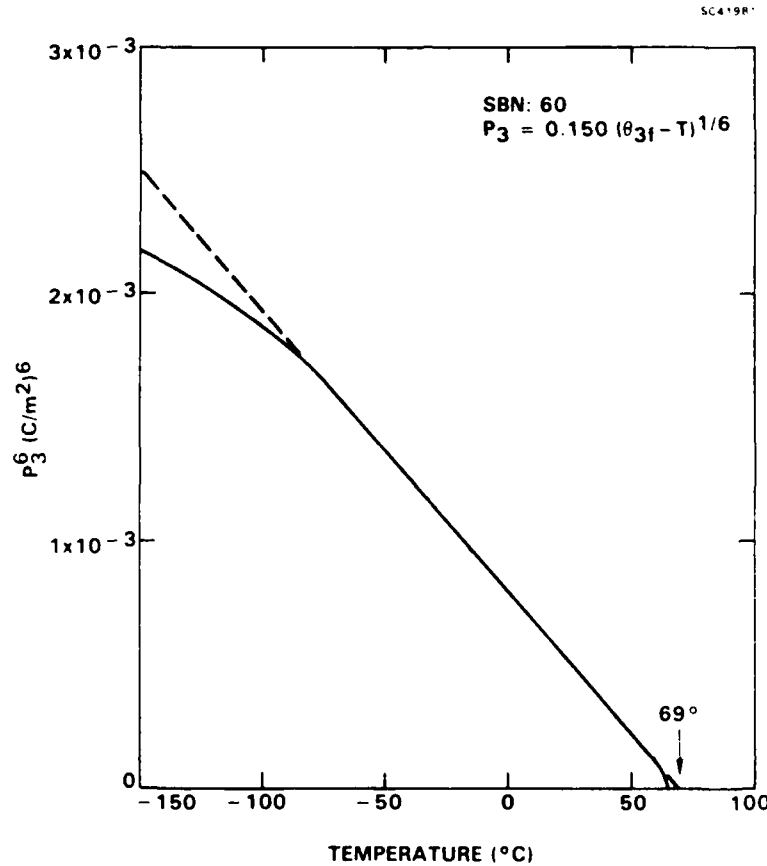


Fig. 6 Plot of the sixth power of P_3 vs temperature, showing a wide linear region below the zero intercept at 69°C .

Using the empirical relation for ϵ_{33} given in Eq. (12) for $T < \theta_{3f}$, Eq. (16) becomes

$$p = \frac{C_{3f} P_3}{C_3(\theta_{3f} - T)} = \frac{P_3}{9.11(\theta_{3f} - T)} \quad (17)$$

a relationship which is in vast disagreement with the observed behavior of Eq. (14). Note that Eqs. (16) and (17) are correct for any number of higher order Devonshire coefficients, as long as they remain independent of temperature. In the particular case of SBN:60, this assumption is clearly not valid.

The dielectric, pyroelectric and polarization behavior described here for SBN:60 has been found consistently in a large number of crystal samples, with relatively minor variations in the physical constants being found from one crystal growth to another.



Effects due to sample geometry are also not significant; excellent agreement in the properties has been found for samples from 0.35 mm up to several millimeters in thickness, indicating that contact layer effects do not play an important role.

It is evident from the polar-axis behavior of SBN:60 that the phenomenology for the Gibbs free energy must be taken out to at least the eighth power of P (sixth power in dielectric stiffness) with temperature-dependent higher order coefficients. Ironically, a reasonable sixth-order least-squares fit to the dielectric data can still be achieved over a moderate temperature range using temperature-independent coefficients.¹⁶ However, the pyroelectric data clearly show that the relationship between p and P_3 (Eq. (14)) is independent of the Curie-Weiss coefficient C_3 , in violation of the phenomenology for temperature-independent higher order coefficients (Eqs. (16) and (17)). This situation is not unique to undoped SBN:60; we have found equivalent behavior in other SBN compositions (e.g., SBN:50), doped crystals (e.g., La^{3+}) and, more importantly, for other ferroelectric bronzes, including compositions in the BSKNN system.¹⁴

The measured temperature dependencies of the spontaneous polarization and the polar-axis dielectric stiffness are highly suggestive of higher order thermodynamic coefficients of the form

$$\alpha_{33} = \alpha_{33}^0 (\theta_{3f} - T)^{2/3}$$

$$\alpha_{333} = \alpha_{333}^0 (\theta_{3f} - T)^{1/3}$$

$$\alpha_{3333} = \alpha_{3333}^0 ,$$

which, qualitatively at least, will then satisfy the observed temperature dependence of ϵ_{33} . The measured relationship between p and P_3 (Eq. (14)) will also be satisfied, but unfortunately without yielding any information about the magnitudes of α_{33}^0 , etc. The postulated temperature dependencies may, however, be unnecessarily strict since the dielectric stiffness and electric field relations involve the sum and difference of at least four (potentially large) terms in the ferroelectric phase. Hence, an additional experimental method is needed to determine the thermodynamic coefficients in an unequivocal manner.



B. The Linear Electro-Dielectric Effect in SBN:60

The extension of the LGD phenomenology out to the eighth power of P_3 in the Gibbs free-energy expansion necessarily leads to an underdetermined set of equations based on the physically measurable parameters E_3 and ϵ_{33} , so that no unique values for the higher order coefficients can be established. One solution to this problem is to examine the behavior of the dielectric constant at several different applied fields; this will lead, for example, to upward shifts of the phase transition temperature for applied fields of the same polarity as the poling field.¹⁷ This technique has been used by many authors to investigate ferroelectric materials, including the excellent work by Glass¹ on SBN compositions and the work by Burns et al³² to determine the values of the sixth-order Devonshire coefficients for La-modified $\text{Sr}_2\text{KNb}_5\text{O}_{15}$ crystals. Unfortunately, this type of analysis is necessarily limited to a small temperature range near T_C , and is further complicated by finite distributions of transition temperatures in materials such as SBN.

An alternative technique is to examine small changes in the dielectric constant with changes in the applied field at fixed temperatures; this method was successfully used by Drougard et al²⁰ to establish the strong temperature dependence of the fourth-power coefficient in BaTiO_3 using a dynamic low-frequency biasing technique above T_C . This method may also be applied below T_C as long as instrument sensitivity and accuracy are sufficient to measure $\Delta\epsilon_{33}$. In the particular case of the eighth-order phenomenology presented here, the change in the dielectric stiffness with applied electric field along the c-axis may be calculated from Eq. (8):

$$\frac{\partial \chi_{33}}{\partial E_3} = (24\alpha_{33}P_3 + 120\alpha_{333}P_3^3 + 336\alpha_{3333}P_3^5) \frac{\partial P_3}{\partial E_3} \quad (18)$$

For small changes in E_3 , $\partial P_3/\partial E_3 = \epsilon_0\epsilon_{33}$, so that Eq. (18) may be written as

$$\frac{\partial \chi_{33}}{\partial E_3} = \frac{\epsilon_0\epsilon_{33}}{P_3} (24\alpha_{33}P_3^2 + 120\alpha_{333}P_3^4 + 336\alpha_{3333}P_3^6) \quad (19)$$

This equation, combined with the relations for the electric field (Eq. (6)) and dielectric stiffness (Eq. (18)), completes the set of equations necessary to determine the higher order coefficients. Under the constraint of small linear changes of χ_{33} with applied field, the solutions are



$$\begin{aligned} \alpha_{33} &= \frac{1}{32\epsilon_{33}P_3^2} \left[\frac{P_3}{\epsilon_0} \frac{\partial \chi_{33}}{\partial E_3} + 24\epsilon_{33} \frac{(\theta_3 - T)}{C_3} - 11 \right] \\ \alpha_{333} &= \frac{-1}{24\epsilon_{33}P_3^4} \left[\frac{P_3}{\epsilon_0} \frac{\partial \chi_{33}}{\partial E_3} + 12\epsilon_{33} \frac{(\theta_3 - T)}{C_3} - 9 \right] \\ \alpha_{3333} &= \frac{1}{64\epsilon_{33}P_3^6} \left[\frac{P_3}{\epsilon_0} \frac{\partial \chi_{33}}{\partial E_3} + 8\epsilon_{33} \frac{(\theta_3 - T)}{C_3} - 7 \right] \end{aligned} \quad (20)$$

To this point, we have made no assumptions regarding any specific temperature dependencies, except for the paraelectric dielectric stiffness, $(T - \theta_3)/C_3$. In the particular case of SBN:60, we may substitute for the temperature dependence of P_3 and ϵ_{33} , and with the approximation $\theta \approx \theta_3 \approx \theta_{3f}$, the expressions in Eq. (20) become

$$\alpha_{3333} \approx \frac{1}{64C_{3f}P_{30}^6} \left[\frac{P_3}{\epsilon_0} \frac{\partial \chi_{33}}{\partial E_3} + \frac{8C_{3f}}{C_3} - 7 \right], \text{ etc.},$$

where C_{3f} and P_{30} are as defined earlier. Hence, if $\partial \chi_{33}/\partial E_3$ varies with temperature as P_3^{-1} , α_{3333} is a constant. Similarly, α_{33} and α_{333} will vary respectively with temperature as $(\theta - T)^{2/3}$ and $(\theta - T)^{1/3}$, as suggested earlier. Note, however, that the higher order coefficients need not follow any specific simple functions of temperature, but need only satisfy the general expressions given in Eq. (20).

The linear electro-dielectric effect, $\partial \chi/\partial E$, is the low-frequency analog of the linear electro-optic effect in ferroelectric crystals, and it is a particularly powerful test for the validity of truncated free energy power expansions. For example, rearrangement of the third expression in Eq. (20) gives

$$\frac{\partial \chi_{33}}{\partial E_3} = \frac{\epsilon_0}{P_3} \left[64\epsilon_{33}\alpha_{3333}P_3^6 - 8\epsilon_{33} \frac{(\theta_3 - T)}{C_3} + 7 \right] \quad (21)$$

so that by setting $\alpha_{3333} = 0$, the electro-dielectric response for a sixth-order Gibbs free-energy expansion may be calculated. In the particular case of SBN:60 at 20°C, with $\epsilon_{33} = 920$ and $P_3 = 0.285 \text{ C/m}^2$, the calculated sixth-order response is $190 \times 10^{-12} \text{ m/V}$. The



measured value, constant for linear dielectric changes of up to several percent, is 418×10^{-12} m/V, more than twice the calculated sixth-order value. This discrepancy cannot be accounted for by adiabatic or contra-piezoelectric corrections since these amount to at most a 3-4% correction to the calculated value. This particular result is what finally confirmed our recent suspicions that a sixth-order LGD phenomenology was inadequate to characterize SBN compositions, and perhaps the tungsten bronze crystal family in general.

A full series of electro-dielectric measurements were carried out from -140°C to T_c on poled SBN:60 crystals from different growths. All measurements were made at fixed temperatures to insure equilibrium conditions. Although the response times for changes in applied field were short below 50°C (on the order of the bridge-balancing time of ~ 1 s or less), these increased to tens of seconds near T_c , rendering methods such as low-frequency dynamic biasing to be of limited value. Nevertheless, the latter has appealing features and may be explored in future work. In the present work, all electro-dielectric measurements were performed using static electric fields of alternating polarity.

Representative electro-dielectric response data for SBN:60 are shown in Fig. 7. The higher order Devonshire coefficients were calculated from these data and from measured ϵ_{33} and P_3 values using Eq. (20), and are plotted on a log-log scale vs $(\theta_{3f}-T)$ in Fig. 8. These coefficients are well characterized by the postulated temperature dependencies, with

$$\begin{aligned} \alpha_3 &= -1.22 \times 10^{-6} (\theta_3 - T) \\ \alpha_{33} &= 1.54 \times 10^{-4} (\theta_{3f} - T)^{2/3} \quad (\text{m}^2/\text{C})^2 \\ \alpha_{333} &= -1.03 \times 10^{-2} (\theta_{3f} - T)^{1/3} \quad (\text{m}^2/\text{C})^4 \\ \alpha_{3333} &= 2.20 \times 10^{-1} \quad (\text{m}^2/\text{C})^6 \end{aligned}$$

The solid curve in Fig. 7 is calculated from Eq. (21) using the value of α_{3333} given above.

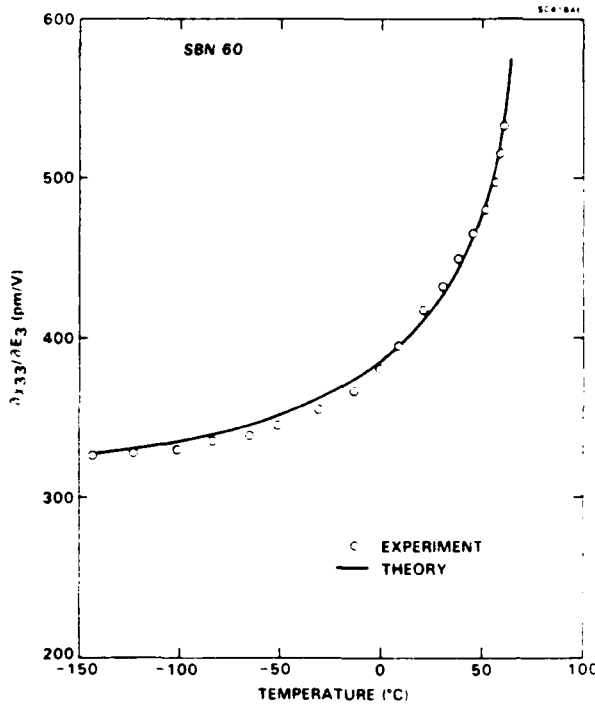


Fig. 7

The polar axis linear electrodielectric response of poled SBN:60. The solid line is the theoretical curve based on the derived phenomenological constant α_{3333} .

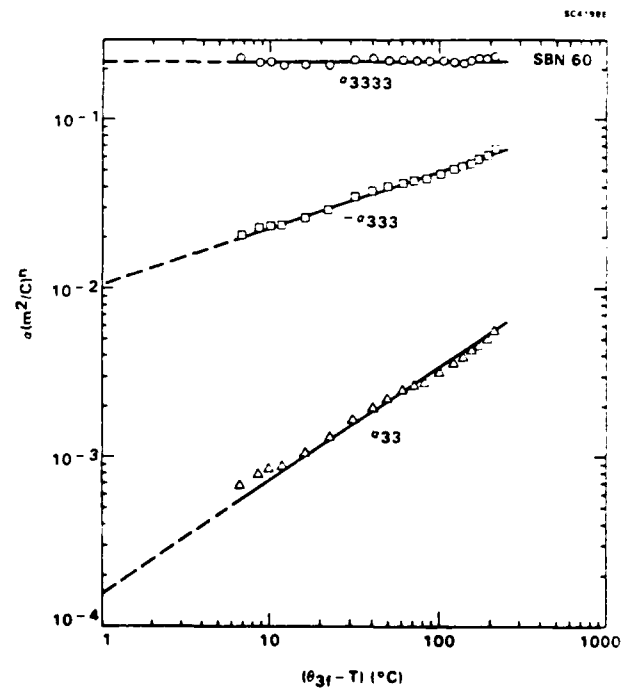


Fig. 8

Log-log plots of the higher order c-axis Devonshire coefficients vs $(\theta_{3f}-T)$. The coefficients follow a $(\theta_{3f}-T)^n$ temperature dependence, with $n = 0, 1/3$ and $2/3$.



The electro-dielectric response was found to be independent of applied voltage, as expected, for dielectric change up to 3-4%; the maximum applied voltage was adjusted with temperature to maintain adequate sensitivity and linearity. However, close to T_c no consistent data could be obtained due to long-term drifts. In spite of the long equilibration times necessary after temperature changes near T_c (~ 1 h), the dielectric data were found to be highly reproducible on cooling, indicating that a fully poled, single ferroelectric domain condition can be maintained in SBN:60 even after long-term exposures to elevated temperatures near T_c .

Figure 9 shows the calculated crystal free energy, ΔG_1 , as a function of polarization. At room temperature, the depth of the potential well is only ~ 1 meV per unit cell, substantially below the thermal energy, kT , thus illustrating the cooperative coupling of microdomains necessary to maintain a uniform macrodomain state. The calculated free energy is absolutely stable over the entire temperature range; metastable states for $\Delta G = \Delta G_1 - E_3 P_3$ do exist for reverse polarity fields, but these are inaccessible since they lie at energies above those for the absolutely stable states. Calculated P_3 vs E_3 hysteresis loops for SBN:60 show a coercive switching field of approximately 20 kV/cm at room temperature, a factor of eight larger than the ~ 2.5 kV/cm encountered experimentally. This result is not surprising, however, since the phenomenological model does not attempt to account for the kinetics of microdomain reversal.^{33,34}

The electro-dielectric character of SBN:60 crystals was also examined above the ferroelectric phase transition temperature. In this phase, P_3 is small or zero at zero bias; hence, using $P_3 \approx \Delta P_3 = \epsilon_0 \epsilon_{33} \Delta E_3$ in Eq. (8), and ignoring higher order terms,

$$\frac{\Delta \chi_{33}}{\Delta E_3} \approx 24 \alpha_{33} \epsilon_0^2 \epsilon_{33}^2 \Delta E_3 \quad (T > T_c) \quad , \quad (22)$$

or

$$\frac{\Delta \epsilon_{33}}{\epsilon_{33}} \approx -24 \alpha_{33} \epsilon_{33}^3 (\epsilon_0 \Delta E_3)^2 \quad . \quad (23)$$

Therefore, $\Delta \epsilon_{33}/\epsilon_{33}$ is expected to vary quadratically with applied electric field and rapidly diminish above T_c with the third power of ϵ_{33} . This behavior was found in SBN:60, but some asymmetry with $\pm \Delta E_3$ was seen in poled crystals at temperatures as much as 40°C above T_c . A more symmetric response was found after thermal depoling under shorted conditions, although measurements below 95°C remained unreliable due to long-term drifts,



presumably due to crystal repoling. From the measurements over the temperature range of 100-150°C, the averaged value of α_{33} calculated from Eq. (23) is

$$\alpha_{33} \approx -1.4 \times 10^{-4} \text{ (m}^2/\text{C)}^2 \quad (T > T_c) \quad ,$$

a value opposite in sign to the $T < T_c$ value. Although it was difficult to establish any temperature dependence for α_{33} in the paraelectric phase, it seems reasonable to presume that α_{33} changes sign somewhere near T_c with no abrupt discontinuities. Such a sign change may also occur for α_{333} , but this could not be determined from these measurements.

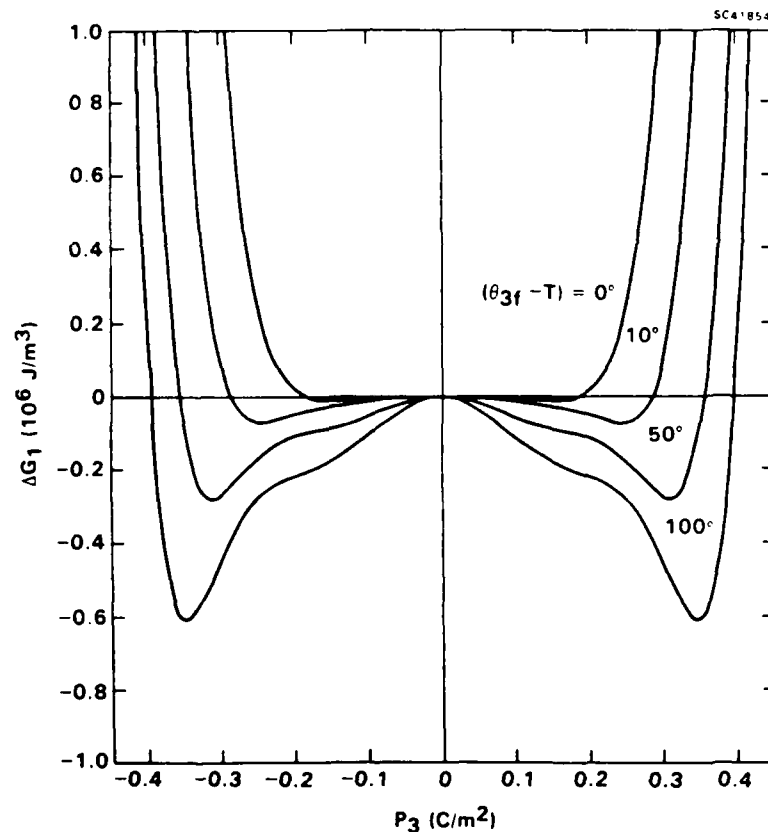


Fig. 9 Calculated curves for the Gibbs free energy of SBN:60 at four temperatures, showing absolute stability for the energy minima at $P_3 = \pm P_S$.



VI. NONPOLAR PROPERTIES

We now turn attention to the dielectric properties of SBN:60 along the nonpolar a- or b-axis. The weak-field dielectric stiffness at zero bias is given in Eq. (7a) and repeated here for convenience:

$$\chi_{11} = \chi_{22} = \frac{(T-\theta_1)}{C_1} + 2\alpha_{13}P_3^2 + 2\alpha_{133}P_3^4$$
$$(P_1 = P_2 = 0) \quad (24)$$

A dielectric anomaly is therefore anticipated for the nonpolar directions as a result of the onset of the spontaneous polarization, P_3 . A complicating factor in the measurement of the nonpolar dielectric properties is the large dielectric anisotropy of most tetragonal ferroelectric bronzes, so that incomplete contact coverage or slight axial misalignment can cause erroneous results, particularly near T_C . Fortunately, we were able to obtain a nearly perfectly oriented a-axis crystal wafer (as evidenced by x-ray diffraction and ac conductivity measurements), and its dielectric behavior is shown on an expanded scale in Fig. 10. Corresponding Arrhenius plots of the a-axis conductivity at 0.1, 1.0 and 10 kHz are presented in Fig. 11, showing the virtual absence of major conductivity peaks near T_C .

The a-axis dielectric dispersion over 100 Hz-100 kHz was found to be minimal except at the temperature extremes where it increased to 2-5%. Dielectric losses were similarly low, with $\tan\delta = 0.003$ or less over most of the temperature range, rising primarily above 300°C due to the onset of significant dc conductivity. At room temperature, the dark dc conductivity was typically $5 \times 10^{-16} \Omega^{-1}\text{-cm}^{-1}$ or less.

As expected, changes in ϵ_{11} with applied field were unmeasurable because of the small induced polarization $\Delta P_1 = \epsilon_0 \epsilon_{11} \Delta E_1$; hence, the values of coefficients such as α_{11} and α_{111} in Eq. (7) ($P_1 \neq 0$) could not be determined. This is of little consequence, since these coefficients do not contribute to the dielectric stiffness (Eq. (24)) or the Gibbs free energy (Eq. (2)) at zero bias ($P_1 = P_2 = 0$).

The dielectric stiffness expression in Eq. (24) could be fitted to the measured data under the assumption of temperature-invariant α_{13} and α_{133} . The calculated curve is shown as the dashed line in Fig. 10 based on the following constants:

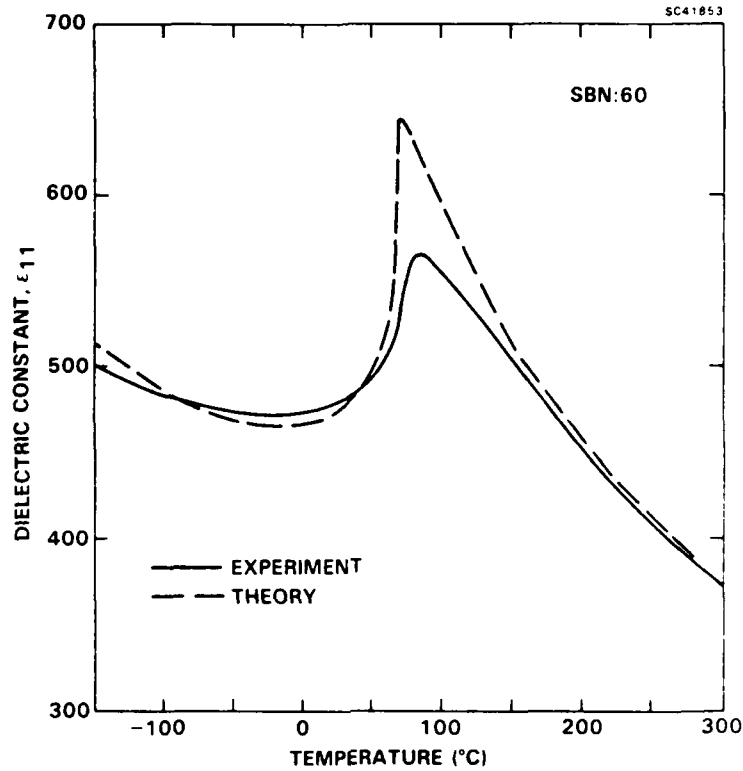


Fig. 10 The a-axis dielectric constant of SBN:60 at 10 kHz. Data at other frequencies are essentially identical. The dashed curve is calculated from the phenomenological model using temperature-independent higher order coefficients.

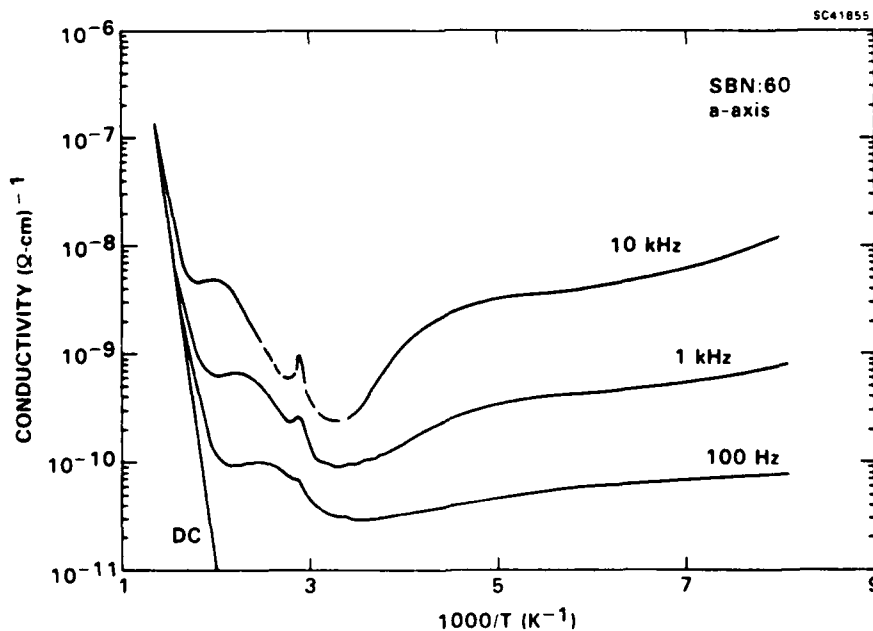


Fig. 11 Arrhenius plots of the a-axis conductivity for SBN:60 at dc, 100 Hz, 1 kHz and 10 kHz; much of the 100 kHz conductivity was below instrument sensitivity. Note the virtual absence of a large conductivity peak at T_C .



$$C_1 = 2.04 \times 10^5$$

$$\theta_1 = -245^\circ \pm 20^\circ\text{C}$$

$$\alpha_{13} = 3.78 \times 10^{-3} (\text{m}^2/\text{C})^2$$

$$\alpha_{133} = 1.40 \times 10^{-2} (\text{m}^2/\text{C})^4$$

The calculated fit to the a-axis dielectric data is generally quite good (less than 3.5% error) except near T_C . Perhaps the most interesting discrepancy is the roughly 10° difference between the theoretical and measured dielectric maxima. The a-axis dielectric peak is also higher in temperature than the c-axis peak by $6-8^\circ$. The shift in temperature between the theoretical and experimental maxima of ϵ_{11} may be accounted for, at least in part, by fluctuations in P_3 such that $\langle P_3 \rangle \approx 0$, but $\langle P_3^2 \rangle \neq 0$, above T_C . This would also help to explain the small discrepancies in the theoretical and measured values for the paraelectric phase well above T_C .

VII. DISCUSSION

The thermodynamic phenomenology developed for SBN:60 may be applied to the calculation of other important crystal properties such as the entropy, S , and the excess heat capacity. Using the crystal free-energy expression in Eq. (2) with $P_1 = P_2 = 0$ and the measured temperature dependencies of the coefficients, the entropy is given by

$$S = - \left(\frac{\partial \Delta G_1}{\partial T} \right)_{P_3}$$

$$= \frac{P_3^2}{\epsilon_0} \left[- \frac{1}{2C_3} + \frac{2}{3} \alpha_{33}^0 (\theta_{3f} - T)^{-1/3} P_3^2 + \frac{1}{3} \alpha_{333}^0 (\theta_{3f} - T)^{-2/3} P_3^4 \right] \quad (25)$$

Inserting the measured temperature dependence of P_3 into Eq. (25), we have

$$S = -0.14 (\theta_{3f} - T)^{1/3} \text{ cal/mole-}^\circ\text{C} \quad (26)$$

and therefore the excess heat capacity due to nonzero polarization below T_C is



$$c_e - c_p^0 = T \left(\frac{\partial S}{\partial T} \right)_E = 0.047 T (\theta_{3p} - T)^{-2/3} \quad \text{cal/mole-}^\circ\text{C} \quad (27)$$

The excess heat capacity is thus expected to peak sharply as the phase transition temperature is approached from below, in qualitative agreement with the experimental results by Glass¹ on early SBN crystals. However, very close to the transition, the calculated excess heat capacity represents a substantial fraction of the background lattice heat capacity of 30-40 cal/mole-°C, whereas the measured values represent only a few percent of the total. Our own preliminary heat capacity results show similar behavior. This is not entirely unexpected, however, since the phenomenological model does not account for a distribution of phase transition temperatures, but rather presents an average of the macroscopic crystal behavior for regions well above and below the transition region.

The Gibbs free-energy function for SBN:60 possesses continuous first derivatives with respect to P, T and discontinuous second derivatives, making SBN:60 a second-order phase transition ferroelectric. It is interesting to note, however, that the temperature behavior of the heat capacity is of the form expected for a classic first-order transition,¹⁹ this being due to the strong temperature dependencies of the higher order Devonshire coefficients. Since these coefficients tend to zero as $T \rightarrow \theta$, the phenomenology suggests that the transition from macropolar to macro-nonpolar is tetracritical in SBN:60.

The highly regular temperature dependencies of the major physical properties for SBN:60 permit the straightforward evaluation of several parameters relevant to device applications. For example, the commonly accepted figure-of-merit for longitudinal pyroelectric IR detectors is p/ϵ_{33} . Using Eqs. (12) and (14),

$$p/\epsilon_{33} = \frac{P_{30}}{6C_{3f}} (\theta_{3f} - T)^{1/6} \quad (28)$$

indicating that this figure-of-merit varies only weakly with the separation between the operating temperature, T, and the transition temperature. Equation (28) is also valid for other SBN compositions (e.g., SBN:50, SBN:75), with differences occurring principally in the value of θ_{3f} and, to a lesser extent, P_{30} .

Another parameter of interest for optical applications is the linear electro-optic coefficient, r_{ij} . The linear electro-optic effect in bronze ferroelectrics may be considered a prototypic quadratic effect biased by the nonzero spontaneous polarization in the ferroelectric phase.³⁵ Hence, along the polar c-axis,



$$r_{33} = 2g_{33}P_3\epsilon_0\epsilon_{33} = \frac{2g_{33}P_3\epsilon_0C_{3f}}{(\theta_{3f}-T)^{5/6}} \quad (29)$$

where g_{33} is the quadratic electro-optic coefficient. Measurements of g_{33} on SBN crystals³⁶ have shown this to be essentially independent of temperature, with a value of $\sim 0.10 \text{ m}^4/\text{C}^2$, so that at room temperature the calculated linear coefficient for SBN:60 is $r_{33} = 464 \times 10^{-12} \text{ m/V}$. This value is in excellent agreement with room-temperature measurements at optical wavelengths,^{8,12,14} although data at other temperatures are presently lacking. However, considerable data for the temperature dependence of r_{33} have been obtained for SBN:60 at millimeter-wave frequencies (30-90 GHz).^{7,37} At room temperature, the equivalent r_{33} value is $1600\text{-}2700 \times 10^{-12} \text{ m/V}$, with the spread in value due partly to complications arising from moderate dielectric losses. At 77K, where the dielectric losses are considerably lower, $r_{33} = 725 \times 10^{-12} \text{ m/V}$, in general agreement with the temperature dependence predicted in Eq. (29). These large values indicate that g_{33} is substantially higher at millimeter-wave frequencies, with a computed value of approximately $0.60 \text{ m}^4/\text{C}^2$.

The linear electro-optic effect at optical and millimeter-wave frequencies is the high-frequency equivalent of the low-frequency linear electro-dielectric effect. It must be cautioned, however, that although the room-temperature value for r_{33} at optical frequencies is similar to the electro-dielectric value ($418 \times 10^{-12} \text{ m/V}$), their functional origins are vastly different. This is reflected in the temperature dependencies, with the linear electro-dielectric effect in SBN:60 following a $(\theta_{3f}-T)^{-1/6}$ dependence, as may be deduced from Eq. (21), whereas r_{33} follows a much stronger $(\theta_{3f}-T)^{-5/6}$ power law. Nevertheless, these two effects do share a common strong dependence on the value of the low-frequency dielectric constant, ϵ_{33} .

In the derivation of the phenomenological constants for SBN:60, we have made use of the measured c-axis dielectric properties in the paraelectric phase to determine the Curie-Weiss constants C_3 and θ_3 , as discussed in Section V. These constants were determined from the linear inverse susceptibility region which exists above T_c up to approximately 250°C (Fig. 4). Above 250°C , however, there exists a second linear Curie-Weiss region, with constants $C_3' = 2.8 \times 10^5$ and $\theta_3' = 134^\circ\text{C}$, the latter being substantially above the phase transition temperature. It has been postulated in the work by Burns and Dacol^{38,39} on bronze $\text{Sr}_2\text{KNb}_5\text{O}_{15}$ (SKN), and more recently in their work with Bhalla et al⁴⁰ on SBN, that observed deviations of the optical refractive index from a linear



temperature dependence above T_c may arise from fluctuations in the polarization such that $\langle P_3 \rangle = 0$, but $\langle P_3^2 \rangle \neq 0$, over a large temperature range. This would necessarily affect the low-frequency dielectric properties as well, and may account for the change in slope of χ_{33} in the paraelectric region below 250°C.

This, then, raises the question regarding which values of C_3 and θ_3 to use in the development of the c-axis phenomenology for the ferroelectric phase. However, evaluation of the ferroelectric phenomenology using the alternative constants from the high-temperature paraelectric region shows a rapid divergence of all of the higher order c-axis Devonshire coefficients near the phase transition, leading to metastable energy states and anomalous calculated hysteresis loops. This is in sharp contrast to the well-behaved, predictable temperature dependencies shown in Section V. This result, combined with the phenomenological similarities determined for other tungsten bronzes such as BSKNN,⁴¹ lead us to conclude that the lower temperature Curie-Weiss region provides a more valid description of the macroscopic paraelectric behavior of SBN:60 as it applies to the temperature dependence of α_3 in the ferroelectric phase.

The presence of fluctuating polar microdomains in the paraelectric phase below 300°C would also serve to explain the deviation of ϵ_{11} from the extrapolated high-temperature Curie-Weiss behavior, as shown in Fig. 10. An average rms polarization, $P_d = \langle P^2 \rangle^{1/2}$, may be calculated from a least-squares fit of Eq. (24) to the measured a-axis paraelectric data using the temperature-independent values for α_{13} and α_{133} calculated earlier. Such a fit shows a substantial nonzero P_d which declines nearly linearly with temperature up to ~ 250-300°C, in qualitative agreement with the results from optical index measurements.⁴⁰ However, the calculated magnitude of P_d critically depends upon the chosen values for the Curie-Weiss parameters C_1 and θ_1 in Eq. (24), and hence cannot be determined with particular confidence. This uncertainty also exists, to some extent, in the interpretation of the refractive index data, as it also depends upon the chosen extrapolation of a linear high-temperature region.³⁸⁻⁴⁰

While this analysis is adequate to qualitatively account for the deviation of ϵ_{11} from Curie-Weiss behavior in the paraelectric phase, the situation is more complicated along the c-axis. In this direction, any spatially fluctuating (and possibly dynamically inverting) polar microdomains would be perturbed by an ac measurement field, E_3 , and thus would contribute significantly to the macroscopic dielectric polarizability.⁴⁰ At the lowest order, this would qualitatively lead to an apparent change in the Curie-Weiss behavior of α_3 (Eqs. (6) and (8)), with the higher order terms contributing to the measured dielectric



behavior by a considerably smaller amount. By inference from the discussion of ferroelectric stability given above, this contribution from fluctuating microdomains would necessarily extrapolate well into the ferroelectric region below T_c . Further support for this hypothesis is provided by millimeter-wave measurements, which show anomalous *c*-axis dielectric losses at room temperature which diminish on further cooling to 77K.^{7,37}

VIII. CONCLUSIONS

The experimental data for ferroelectric SBN:60 show that for a more realistic fitting of the data, the Taylor series expansion of the Gibbs free energy must be taken out to at least the eighth power of the polarization, and that the coefficients of terms up to the sixth power must be taken as functions of temperature. This phenomenological description should provide a foundation for future comparisons with other compositions in the bronze crystal family, and may also assist in uncovering potentially anomalous ferroelectric behavior in materials which otherwise may appear to have well-behaved dielectric and polarization properties. It is noteworthy, however, that a more classical sixth-order phenomenology with temperature-invariant higher order coefficients still provides a useful, approximate description for many of the measured properties,¹⁶ and has proven particularly effective for comparisons with other crystal families.³⁶

The extended eighth-order phenomenology is that of a simple proper crystalline ferroelectric. The highly regular behavior of the phenomenology suggests that this description is perfectly adequate to account for the observed ferroelectric properties in SBN:60. However, there has been some suggestion that SBN may be an incommensurate phase transition ferroelectric.⁴² Although the present phenomenology does not preclude such a possibility, neither does it suggest it, since the computed energy states remain absolutely stable over the entire temperature range. In either case, the phenomenology should prove useful in developing a much clearer theoretical description for the ferroelectric behavior in SBN crystals, and perhaps for other bronze crystal systems as well.



ACKNOWLEDGEMENTS

The authors wish to thank W.K. Cory for his patient work on the Czochralski crystal growth technology used for the development of high quality SBN crystals. This research on the phenomenology of SBN was supported by the Office of Naval Research (Contract No. N00014-81-C-0463).

REFERENCES

1. A.M. Glass, J. Appl. Phys. 40 (12), 4699 (1969).
2. R.R. Neurgaonkar, M.H. Kalisher, T.C. Lim, E.J. Staples and K.L. Keester, Mat. Res. Bull. 15, 1235 (1980).
3. R.R. Neurgaonkar, DARPA Final Report, Contract No. F49620-78-C-0093 (1982).
4. G. Burns, IEEE Trans. Electron Dev. ED-16 (16), 506 (1969). Includes an extensive bibliography of early tungsten bronze papers.
5. K. Tada, T. Murai, M. Aoki, K. Muto and K. Awazu, Japan. J. Appl. Phys. 11 (11), 1622 (1972).
6. R.R. Neurgaonkar, W.K. Cory and J.R. Oliver, Ferroelectrics 51, 3 (1983).
7. W.F. Hall, W.W. Ho, R.R. Neurgaonkar and W.K. Cory, Proc. 6th IEEE Int. Symp. on Applications of Ferroelectrics (ISAF), 469 (1986).
8. R.R. Neurgaonkar, J.R. Oliver, W.K. Cory and L.E. Cross, in Advances in Materials for Active Optics (S. Musikant, ed.), Proc. SPIE 567, 11 (1985).
9. B. Fischer, M. Cronin-Golomb, J.O. White, A. Yariv and R.R. Neurgaonkar, Appl. Phys. Lett. 40, 863 (1982).



10. G. Salamo, M.J. Miller, W.W. Clark III, G.L. Wood and E.J. Sharp, *Opt. Comm.* 59, 417 (1986).
11. E.J. Sharp, M.J. Miller, G.L. Wood, W.W. Clark III, G.J. Salamo and R.R. Neurgaonkar, *Proc. Sixth IEEE Int'l Symp. on Applications of Ferroelectrics (ISAF)*, 51 (1986).
12. R.R. Neurgaonkar and W.K. Cory, *J. Opt. Soc. Am. B* 3, 274 (1986). Includes an extensive bibliography of early and more recent papers on tungsten bronze ferroelectrics.
13. G. Rakuljic, A. Yariv and R.R. Neurgaonkar, *Opt. Eng.* 25 (11), 1212 (1986).
14. R.R. Neurgaonkar, W.K. Cory, J.R. Oliver, M.D. Ewbank and W.F. Hall, *Optical Eng.* 26 (5), 392 (1987).
15. K. Megumi, N. Nagatsuma, K. Kashiwada and Y. Furuhata, *Mat. Science* 11, 1583 (1976).
16. T.R. ShROUT, L.E. Cross, P. Moses, H.A. McKinstry and R.R. Neurgaonkar, *Proc. IEEE 1980 Ultrasonics Symp.*, 414 (1980).
17. A.F. Devonshire, *Adv. Phys.* 3 (10), 85 (1954).
18. See for example J.F. Nye, *Physical Properties of Crystals* (Clarendon Press, Oxford, 1969).
19. M.E. Lines and A.M. Glass, *Principals and Applications of Ferroelectrics and Related Materials* (Clarendon Press, Oxford, 1977).
20. M.E. Drougard, R. Landauer and D.R. Young, *Phys. Rev.* 98 (4), 1010 (1955).
21. M.H. Francombe, *Acta Cryst.* 13, 131 (1960).
22. P.B. Jarnieson, S.C. Abrahams and J.L. Bernstein, *J. Chem. Phys.* 48 (11), 5048 (1968).



23. L.A. Shuvalov, Proc. Second Int'l Meeting on Ferroelectricity, J. Phys. Soc. Japan 28 (Suppl.), 38 (1970).
24. A.A. Ballman and H. Brown, J. Cryst. Growth 1, 311 (1967).
25. R.B. Maciolek and S.T. Liu, J. Electron. Mat. 2, 191 (1973).
26. F.J. Morin, J.R. Oliver and R.M. Housley, Phys. Rev. B 6 (10), 4434 (1977).
27. R. Clarke and J.C. Burfoot, J. Phys. D 8, 1115 (1975).
28. I. Camlibel, J. Appl. Phys. 40 (4), 1690 (1969).
29. T.W. Cline and L.E. Cross, J. Appl. Phys. 49 (7), 4298 (1978).
30. G. Borchardt, J. v. Cieminski and G. Schmidt, Phys. Sol. Stat. (a) 76, K1-41 (1983).
31. A.S. Bhalla and L.E. Cross, Ferroelectrics 38, 935 (1981).
32. G. Burns, D.F. O'Kane, E.A. Giess and B.A. Scott, Solid State Comm. 6, 223 (1968).
33. M. Hayashi, J. Phys. Soc. Japan 33 (3), 616 (1972).
34. L. Godefroy, Ferroelectrics 35, 207 (1981).
35. M. DiDomenico and S.H. Wemple, J. Appl. Phys. 40 (2), 720 (1969).
36. R.R. Neurgaonkar and L.E. Cross, DARPA Semi-Annual Technical Reports No. 1 (1983) and No. 5 (1985), Contract No. N00014-82-C-2466.
37. R.R. Neurgaonkar, J.R. Oliver, L.E. Cross and W.F. Hall, ONR Annual Report No. 5, Contract No. N00014-81-C-0463 (1985).
38. G. Burns, Phys. Rev. B 13 (1), 215 (1976).



39. G. Burns and F.H. Dacol, Phys. Rev. B 30 (7), 4012 (1984).
40. A.S. Bhalla, R. Guo, L.E. Cross, G. Burns, F.H. Dacol and R.R. Neurgaonkar, Phys. Rev. B 36 (4), 2030 (1987).
41. J.R. Oliver, R.R. Neurgaonkar and L.E. Cross, unpublished.
42. J. Schneck, J.C. Toledano, R. Whatmore and F.W. Ainger, Ferroelectrics 36, 327 (1981).



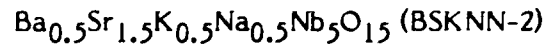
Rockwell International
Science Center

SC5345.AR

**8.0 PRELIMINARY RESULTS ON THE THERMODYNAMIC PHENOMENOLOGY
FOR FERROELECTRIC TUNGSTEN BRONZE BSKNN-2**



PRELIMINARY RESULTS ON THE THERMODYNAMIC PHENOMENOLOGY
FOR FERROELECTRIC TUNGSTEN BRONZE



J.R. Oliver and R.R. Neurgaonkar
Rockwell International Science Center
Thousand Oaks, CA 91360

I. INTRODUCTION

In prior work on the Landau:Ginsburg:Devonshire (LGD) phenomenology for tungsten bronze SBN:60,¹ it was shown that an expanded thermodynamic phenomenology for tetragonal (4mm) ferroelectrics could uniquely describe the measured properties with the prediction of absolutely stable ferroelectric states at all temperatures. This work has now been extended to the important tungsten bronze ferroelectric $\text{Ba}_{0.5}\text{Sr}_{1.5}\text{K}_{0.5}\text{Na}_{0.5}\text{Nb}_5\text{O}_{15}$ (BSKNN-2).² As in the case for SBN:60, the phenomenology for BSKNN-2 is based on a Taylor expansion of the Gibbs free energy function taken out to the eighth power of the polarization, with no assumptions made about the possible temperature dependencies of the higher order coefficients.

The preliminary results presented here show that BSKNN-2 possesses several striking similarities to SBN compositions for a temperature range some 80°C below the ferroelectric phase transition temperature. However, at temperatures down to room temperature and below, BSKNN-2 shows anomalous behavior in the E-field dependence of the low frequency dielectric permittivity which cannot be explained on the basis of the phenomenology for a simple proper ferroelectric. These results may ultimately help to explain the discrepancies in the calculated vs. measured electro-optic coefficients, r_{ij} , for BSKNN-2 at millimeter wave^{3,4} and optical frequencies,^{5,6} in contrast to the more predictable results achieved for SBN:60.^{1,2,7}



II. FERROELECTRIC PROPERTIES OF BSKNN-2

Measurements of the dielectric, pyroelectric and polarization properties of BSKNN-2 were made on crystal wafers oriented along the polar c-axis ($\langle 001 \rangle$) and the non-polar a-axis ($\langle 100 \rangle$). All samples used sputtered Pt/Au contacts annealed at 500°C or above prior to measurement. Crystals of several different thicknesses (0.30 - 1.3 mm) were examined with little discernable difference in the measured properties; hence, contact boundary layer effects do not appear to have played any significant role in the measured properties.

The dielectric constant along the polar c-axis, ϵ_{33} , for a poled BSKNN-2 crystal is shown as a function of temperature in Fig. 1. Crystal poling to a single ferroelectric domain was accomplished in a dry oxygen atmosphere using a normal field-cooling method, with a d.c. poling field of 7-10 kV/cm applied from just below the phase transition down to room temperature. Although some frequency-dependent relaxor behavior is evident in Fig. 1 near the ferroelectric phase transition temperature (Curie point) at 171°C, it is less pronounced than the relaxor effects observed for SBN compositions. It is suspected that the diminished relaxor character of BSKNN compositions results from the complete filling of the A_1 (15-fold coordinated) and A_2 (12-fold coordinated) lattice sites in the tungsten bronze lattice, so that the lattice site uncertainty of the Sr^{2+} and Ba^{2+} ions is substantially reduced compared to the large site uncertainty found in the partially-filled SBN lattice.²

BSKNN-2 also has a much sharper dielectric anomaly at the phase transition compared to SBN:60. This is reflected in the behavior of the reciprocal dielectric constant, $\chi_{33} = \epsilon_{33}^{-1}$, which is shown in Fig. 2. χ_{33} has a nearly linear Curie-Weiss behavior both above and below the phase transition, with

$$\begin{aligned} \chi_{33} &= (T - \theta_3)/C_3 & (T > T_c) \\ &= (\theta_{3f} - T)/C_{3f} & (T < T_c) \end{aligned} \quad (1)$$

In the paraelectric phase ($T > T_c$), $C_3 = 2.35 \times 10^5$ and $\theta_3 = 168^\circ\text{C}$, whereas in the ferroelectric phase, $C_{3f} = 2.70 \times 10^4$ and $\theta_{3f} = 169^\circ\text{C}$, with the latter functional dependence remaining linear down to approximately room temperature. The values of C_3 and C_{3f} are substantially lower than the values found for SBN:60¹ (4.10×10^5 and 4.50×10^4 , respectively), reflecting the sharper dielectric character of BSKNN-2. However, the $C_3:C_{3f}$ ratio of 8.7

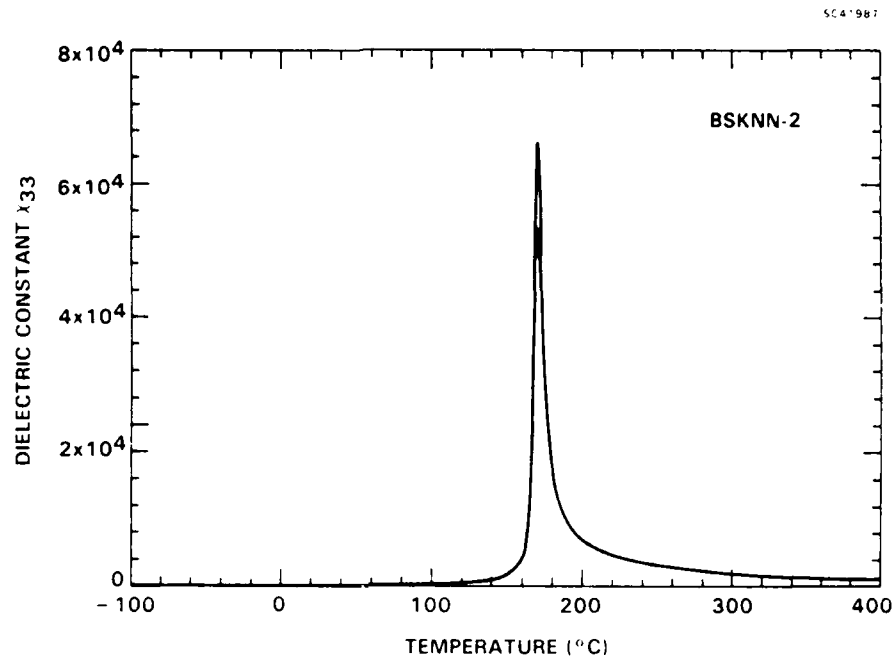


Fig. 1 Polar axis dielectric constant for a poled BSKNN-2 crystal at 100 Hz (upper curve) and 100 kHz (lower curve). $T_C = 170-171^\circ\text{C}$.

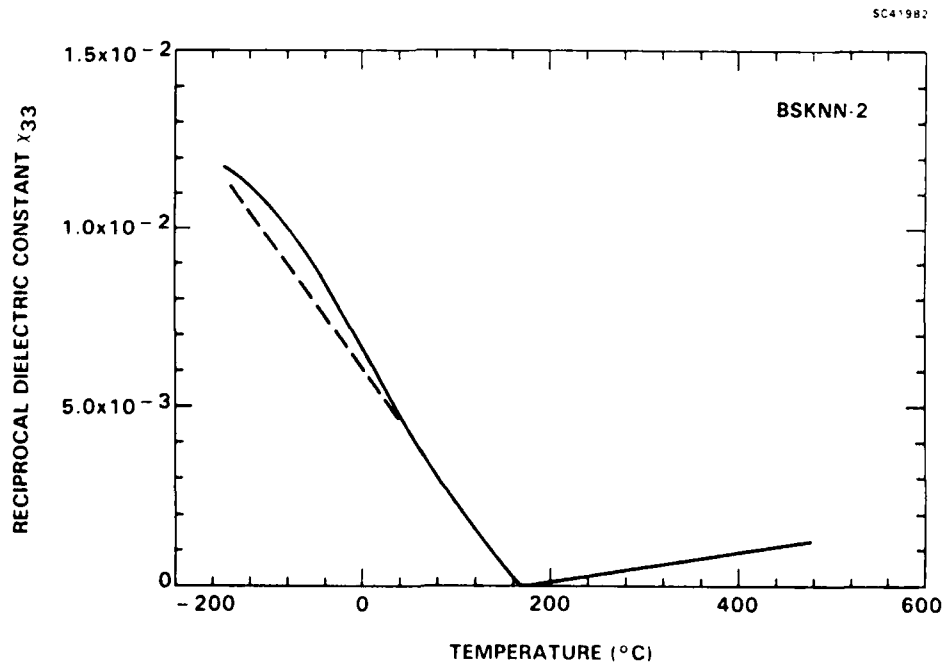


Fig. 2 Polar axis reciprocal dielectric constant (stiffness) at 10 kHz for poled BSKNN-2.



remains similar to that for SBN:60. Considering the small uncertainty in the determination of the θ values, we take $\theta_3 = \theta_{3f} = 169^\circ\text{C}$, making BSKNN a second order phase transition ferroelectric consistent with its very large dielectric anomaly.

The measured temperature dependencies of the polarization, P_3 , and the pyroelectric coefficient, $p = -dP_3/dT$, for BSKNN-2 are shown in Fig. 3. The respective values at room temperature are $P_3 = 0.311 \text{ C/m}^2$ and $p = 3.5 \times 10^{-4} \text{ C/m}^2\text{-}^\circ\text{C}$, the latter being a factor of three lower than the pyroelectric coefficient for SBN:60 due to the substantial difference in the phase transition temperatures. An examination of the temperature dependence of the polarization shows that P_3^6 varies linearly with temperature over a wide range, as shown in Fig. 4. Formally,

$$P_3 = P_{30}(\theta_3 - T)^{1/6}, \quad (2)$$

with $P_{30} = 0.135 \text{ C/m}^2\text{-}(^\circ\text{C})^{1/6}$, compared to a value of 0.150 for SBN:60.¹

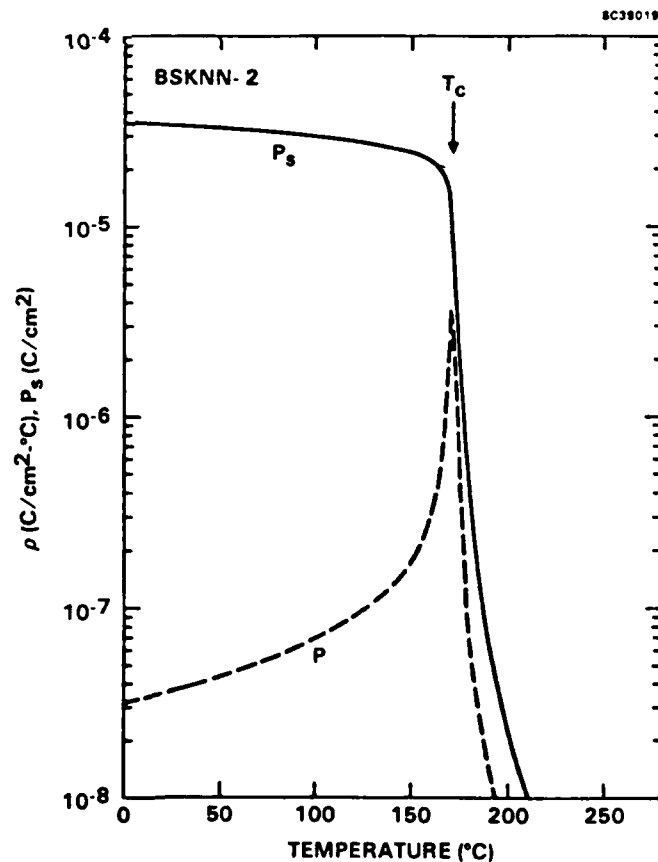


Fig. 3

The polar axis polarization, P_3 , and the pyroelectric coefficient, p , for BSKNN-2.

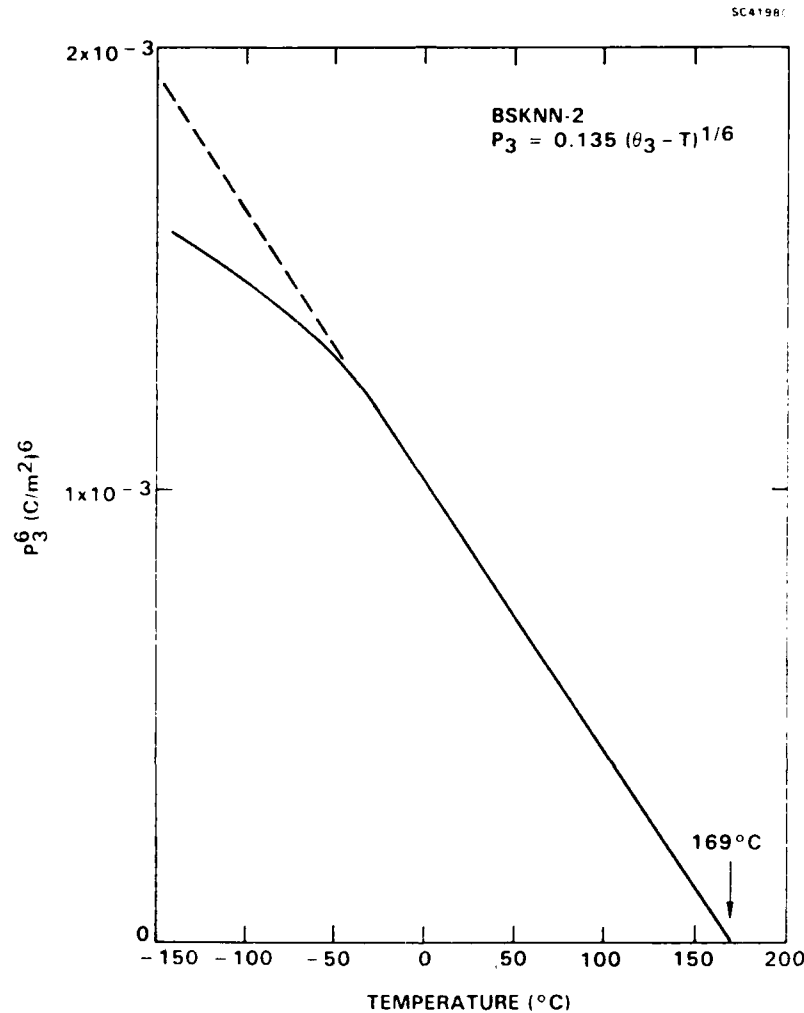


Fig. 4 Plot of the sixth power of P_3 for BSKNN-2, showing the linear region below the zero intercept at 169°C.

III. THERMODYNAMIC PHENOMENOLOGY

The general dielectric and polarization character of BSKNN-2 shows great similarity to SBN:60, particularly regarding the temperature dependence of the polarization and the nearly linear Curie-Weiss dielectric stiffness behavior in the ferroelectric phase. Considering BSKNN-2 to have a tetragonal 4mm symmetry in the ferroelectric phase with a unique polar c-axis ($P_3 \neq 0$), the eighth order LGD phenomenological relation for the excess Gibbs free energy under the condition $P_1 = P_2 = 0$ is^{1,8}



$$\Delta G_1 = \frac{1}{\epsilon_0} (\alpha_3 P_3^2 + \alpha_{33} P_3^4 + \alpha_{333} P_3^6 + \alpha_{3333} P_3^8) \quad (3)$$

where the Devonshire coefficients, α , have been normalized by the free-space permittivity, ϵ_0 . The expression for the electric field, E_3 , is found by setting the derivative with respect to P_3 of $\Delta G = \Delta G_1 - E_3 P_3$ equal to zero, giving

$$E_3 = \frac{1}{\epsilon_0} (2\alpha_3 P_3 + 4\alpha_{33} P_3^3 + 6\alpha_{333} P_3^5 + 8\alpha_{3333} P_3^7) \quad (4)$$

Finally, the c-axis dielectric stiffness is given by

$$\chi_{33} = \epsilon_0 \frac{\partial E_3}{\partial P_3} = 2\alpha_3 + 12\alpha_{33} P_3^2 + 30\alpha_{333} P_3^4 + 56\alpha_{3333} P_3^6 \quad (5)$$

In the paraelectric phase above T_c , $P_3 = 0$, so that only the α_3 term remains in the dielectric stiffness expression in Eq. (5). Hence, from the measured paraelectric behavior of χ_{33} in Eq. (1), we have

$$\chi_{33} = 2\alpha_3 = (T - \theta_3)/C_3 \quad (T > T_c) \quad (6)$$

In order to have a complete set of equations necessary to uniquely determine all of the Devonshire coefficients, an additional relation is needed beyond the measurable parameters E_3 and χ_{33} in Eqs. (4) and (5). This is satisfied by the relation for the linear electro-dielectric response, given by

$$\frac{\partial \chi_{33}}{\partial E_3} = \frac{\epsilon_0 \epsilon_{33}}{P_3} (24\alpha_{33} P_3^2 + 120\alpha_{333} P_3^4 + 336\alpha_{3333} P_3^6) \quad (7)$$

Experimentally, Eq. (7) may be determined by the linear change in χ_{33} with changes in the d.c. bias field, E_3 . The combination of Eqs. (4), (5) and (7), using the experimental value of α_3 established from Eq. (6), may then be used to determine the unique values of α_{33} , α_{333} and α_{3333} at any given temperature.

Figure 5 shows the measured electro-dielectric response for BSKNN-2 taken at a series of discrete temperatures. The derived values for the Devonshire coefficients are plotted on a log-log scale vs. $(\theta_3 - T)$ in Fig. 6. For an 80°C range below θ_3 , these coefficients follow the same temperature dependencies found previously for SBN:60,¹ with

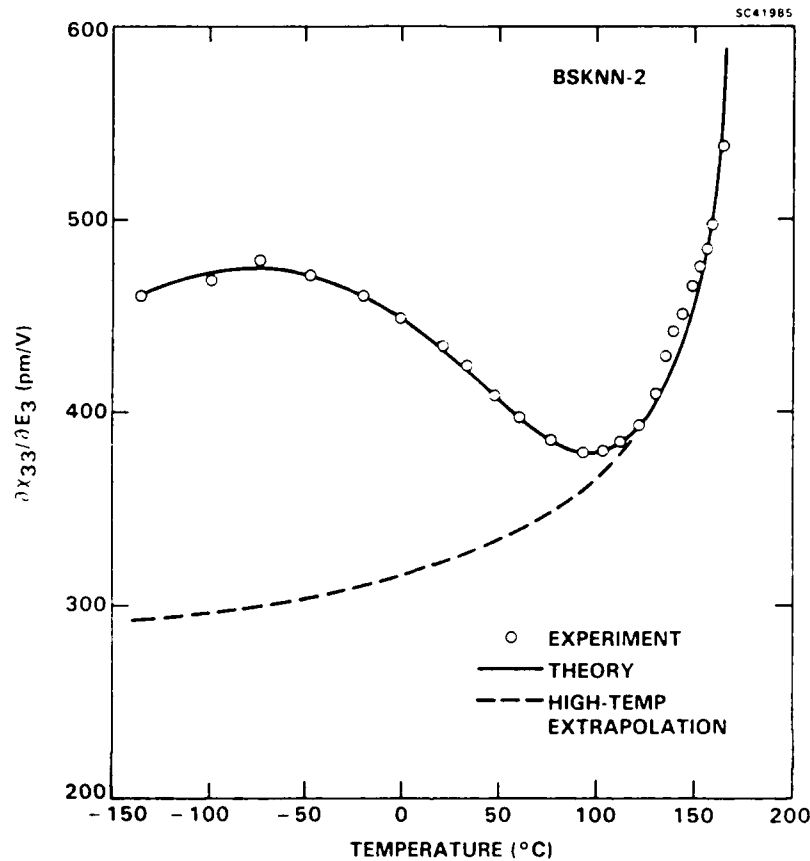


Fig. 5 The polar axis electro-dielectric response for BSKNN-2. The dashed line is the extrapolated theoretical curve based on the high temperature phenomenological behavior.

$$\alpha_{33} = \alpha_{33}^0 (\theta_3 - T)^{2/3} \quad (m^2/C)^2, \quad \alpha_{33}^0 = 2.00 \times 10^{-4}$$

$$\alpha_{333} = \alpha_{333}^0 (\theta_3 - T)^{1/3} \quad (m^2/C)^4, \quad \alpha_{333}^0 = -1.73 \times 10^{-2}$$

$$\alpha_{3333} = \alpha_{3333}^0 \quad (m^2/C)^6, \quad \alpha_{3333}^0 = 0.50$$

The dashed line in Fig. 5 is the calculated electro-dielectric response based on the theoretical dependencies. Below 100°C (($\theta_3 - T$) > 70°), the electro-dielectric response deviates substantially from the extrapolated high temperature behavior, resulting in large values for all of the higher order coefficients, as shown in Fig. 6. Far below 100°C, however, the α 's then appear to attain largely temperature-invariant values.

AD-A193 512

RESEARCH ON CRYSTAL AND FILM FERROELECTRIC MATERIALS
FOR OPTOELECTRONIC A. (U) ROCKWELL INTERNATIONAL
THOUSAND OAKS CA SCIENCE CENTER R R NEURGAONKAR MAR 88

2/2

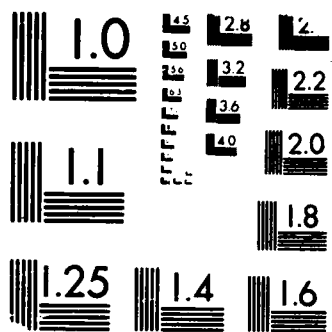
UNCLASSIFIED

SC5345. AR N00014-81-C-0463

F/G 9/5

NL





MICROCOPY RESOLUTION TEST CHART
(NBS 1963-A) STANDARDS 1963 A



SC41986

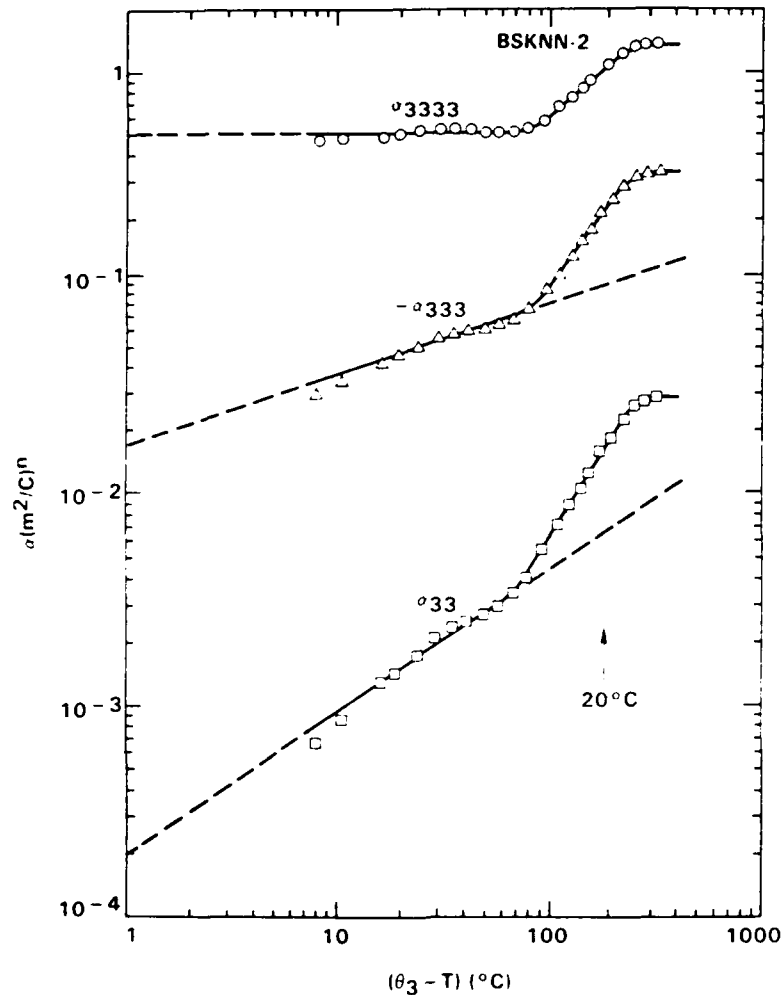


Fig. 6 Log-log plots of the higher order c-axis Devonshire coefficients vs $(\theta_3 - T)$. The coefficients follow the general temperature dependencies found for SBN:60 up to $(\theta_3 - T) = 70^\circ C$, beyond which they deviate considerably.

The significance of the anomalous electro-dielectric behavior for BSKNN-2 can be best appreciated by an examination of the calculated excess crystal free energy, ΔG_1 , using the computed values for the Devonshire coefficients shown in Fig. 6. Calculations of ΔG_1 as a function of polarization are shown in Fig. 7 (a,b) for $(\theta_3 - T) = 40^\circ, 150^\circ$ and $300^\circ C$, the latter two corresponding to the region of anomalous electro-dielectric behavior. For $(\theta_3 - T) = 40^\circ C$, the free energy shows only well-defined, absolutely stable energy minima at the spontaneous polarization, $P_s = \pm 0.26 C/m^2$. Near room temperature ($(\theta_3 - T)$

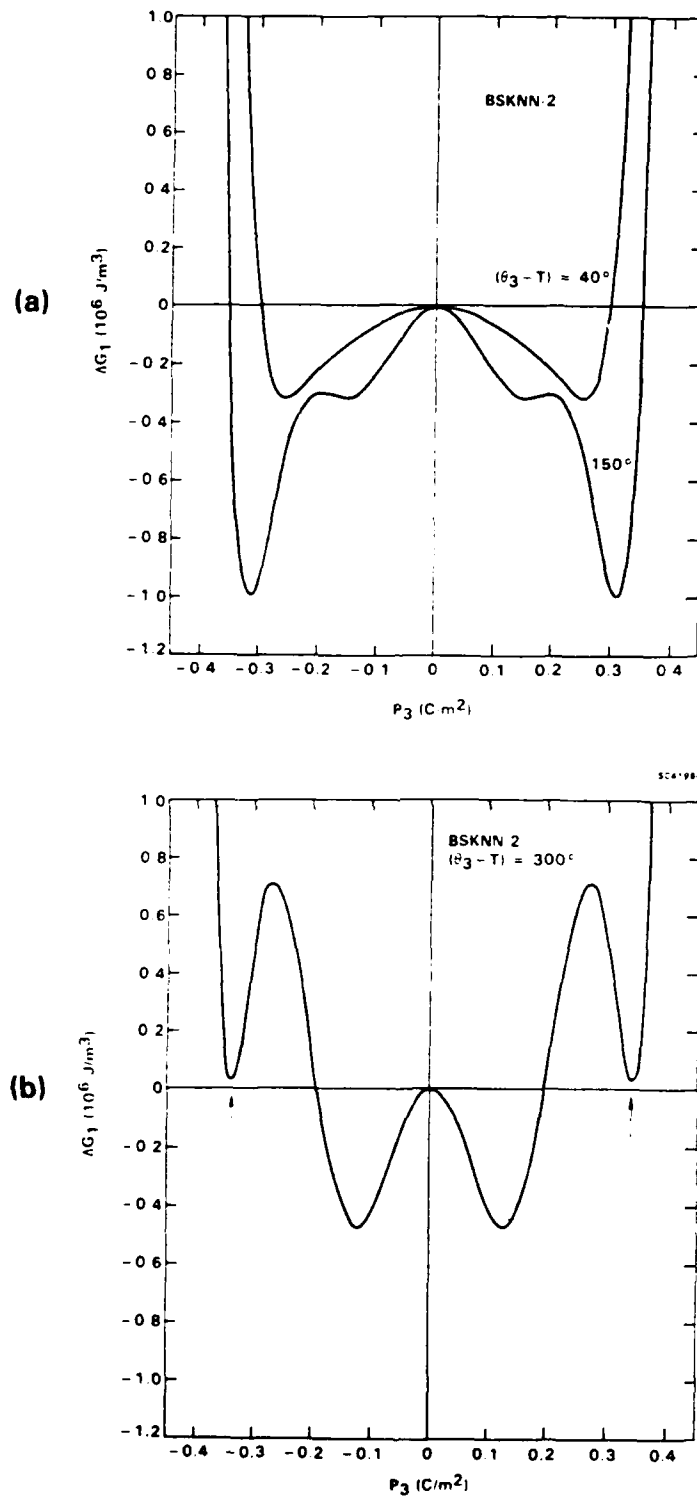


Fig. 7 (a) Calculated Gibbs free energy curves for BSKNN-2 at $(\theta_3 - T) = 40^\circ$ and 150° C, showing absolutely stable ferroelectric states at the energy minima $P_3 = \pm P_s$. (b) Calculated Gibbs free energy curve for BSKNN-2 at $(\theta_3 - T) = 300^\circ$ C, showing metastable ferroelectric states at $P_3 = \pm P_s$.



= 150°C), the energy minima at $P_s = \pm 0.31 \text{ C/m}^2$ are substantially deeper, as expected, but a pair of second, shallower minima also appears at a much lower $\pm P_3$ values. Finally, at $(\theta_3 - T) = 300^\circ\text{C}$ (Fig. 7b), two prominent energy minima pairs appear, with those at $P_s = \pm 0.34 \text{ C/m}^2$ being metastable with respect to the deeper energy minima at $P_3 = \pm 0.12 \text{ C/m}^2$.

The calculated Gibbs free energy results of Fig. 7 clearly indicate a breakdown of the tetragonal bronze ferroelectric phenomenology at temperatures far below the phase transition temperature. Such a breakdown is qualitatively suggested by the unusual electro-dielectric behavior for BSKNN-2 shown in Fig. 5. What is especially interesting, however, is the fact that neither the character of the polarization nor that of the dielectric constant, both of which are smooth, monotonic functions of temperature below T_c , suggest any anomalous behavior for BSKNN-2 in the ferroelectric phase.

We now turn attention to the non-polar a-axis dielectric constant, ϵ_{11} . As in the case for SBN compositions, a dielectric anomaly occurs for ϵ_{11} in the vicinity of T_c , as shown in Fig. 8. Along this axis, the phenomenological relation for the dielectric stiffness, $\chi_{11} = \epsilon_{11}^{-1}$, is given by¹

$$\chi_{11} = 2\alpha_1 + 2\alpha_{13}P_3^2 + 2\alpha_{133}P_3^4, \quad (8)$$

so that a dielectric anomaly is anticipated at the phase transition due to the onset of nonzero spontaneous polarization. In the paraelectric phase ($P_3 = 0$), χ_{11} follows a linear Curie-Weiss law, so that from Eq. (8),

$$\chi_{11} = 2\alpha_1 = (T - \theta_1)/C_1 \quad (T > T_c), \quad (9)$$

where $C_1 = 2.32 \times 10^5$ and $\theta_1 = -83 \pm 10^\circ\text{C}$. The value of C_1 is quite similar to that for SBN:60 (2.04×10^5), but θ_1 has a considerably higher value than one would infer from the 100° difference in the phase transition temperatures for these two bronzes.

The a-axis electro-dielectric response, $\partial\chi_{11}/\partial E_1$, proved unmeasureably small, as expected, due to the low induced polarization $\Delta P_1 = \epsilon_0\epsilon_{11}\Delta E_1$. A fit of Eq. (8) to the measured a-axis dielectric behavior in the ferroelectric phase was made on the basis of temperature invariant values for α_{13} and α_{133} using the measured temperature dependence of α_1 given in Eq. (9). The calculated theoretical curve, shown as the dashed line in Fig. 8, is based on the following values for the higher order a-axis constants:



SC41979

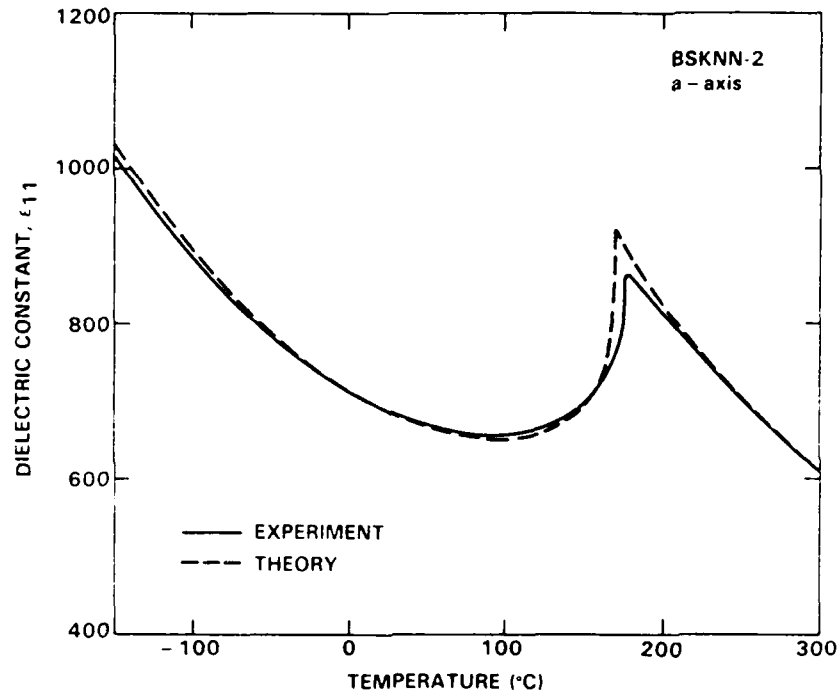


Fig. 8 The a-axis dielectric constant of BSKNN-2 at 10 kHz. The dashed curve is the least-squares fit of the phenomenological model (see text).

$$\alpha_{13} = 4.01 \times 10^{-3} \text{ (m}^2/\text{C)}^2$$
$$\alpha_{133} = 1.14 \times 10^{-2} \text{ (m}^2/\text{C)}^4$$

The calculated curve has an excellent fit to the measured a-axis dielectric data except very close to T_c ; in fact, the fit in this case is substantially better than that found for SBN:60,¹ with an error of 1.5% or less over most of the temperature range.



IV. DISCUSSION

Summaries of the c-axis and a-axis ferroelectric properties of BSKNN-2 are presented in Tables I and II, respectively, in comparison with corresponding results for SBN:60.¹ The phenomenological c-axis constants given for BSKNN-2 in Table I are valid for an 80°C temperature range below the phase transition temperature. It can be seen from both Tables that there are a number of gratifying similarities between BSKNN-2 and SBN:60, with the major differences in the physical properties arising from the dissimilar Curie-Weiss constants, C_3 and C_{3f} , and the necessarily different θ values. Although significant differences also appear for the higher order Devonshire constants, these differences diminish for the dimensionless terms $\alpha_{33}^0 P_{30}^2$, etc., which are more appropriate for the purposes of comparison. As for the remaining dissimilarity in the values for $\alpha_{133} P_{30}^4$, it must be pointed out that the contribution of this term to the a-axis permittivity is small compared to the lower order terms, with its value depending principally on the quality of the fit to the measured data. Indeed, reasonable fits to the a-axis data can still be obtained in both SBN:60 and BSKNN-2 by setting α_{133} identically to zero.

The failure of the phenomenology to predict absolutely stable ferroelectric states at lower temperatures (Fig. 7) indicates that BSKNN-2 cannot be considered a simple tetragonal bronze ferroelectric, in spite of its otherwise smoothly behaved dielectric and polarization properties. It appears that this material may undergo another phase transition, possibly near 90°C, which is ferroelastic and therefore requires a second order parameter (other than polarization) in the phenomenology. As in the case of barium sodium niobate (BNN), this transition would lead to a weakly orthorhombic symmetry at room temperature^{9,10} while still retaining a unique polar c-axis.

Support for this picture is supplied by measurements of the linear electro-optic coefficient, r_{ij} . This coefficient is the high-frequency analog of the low-frequency electro-dielectric response, although their functional dependencies differ considerably. Based on a simple proper ferroelectric model, the phenomenological relation for the c-axis electro-optic coefficient, r_{33} , is given by¹¹

$$r_{33} = 2g_{33}P_3\epsilon_0\epsilon_{33} \quad (10)$$

where g_{33} is the quadratic electro-optic coefficient of the paraelectric prototype. Among the bronzes, g_{33} appears to have a nearly constant, temperature-independent value of



Table I
 Ferroelectric c-axis Properties of SBN:60 and BSKNN-2

| c-axis | SBN:60 | BSKNN-2 |
|--|------------------------|------------------------|
| Curie Point, T_c ($^{\circ}\text{C}$) | 75 $^{\circ}$ | 171 $^{\circ}$ |
| ϵ_{33} @ 20 $^{\circ}\text{C}$ | 920 | 170 |
| P_3 @ 20 $^{\circ}\text{C}$ (C/m^2) | 0.285 | 0.311 |
| P_{30} ($\text{C}/\text{m}^2 - (^{\circ}\text{C})^{1/6}$) | 0.150 | 0.135 |
| p @ 20 $^{\circ}\text{C}$ ($\text{C}/\text{m}^2 - ^{\circ}\text{C}$) | 9.7×10^{-4} | 3.5×10^{-4} |
| r_{33} @ 20 $^{\circ}\text{C}$ (10^{-12} m/V) | 420 - 470 (464)* | 140 - 180 (94)* |
| Curie-Weiss Constants | | |
| θ_3 | 75 $^{\circ}$ | 169 $^{\circ}$ |
| θ_{3f} | 69 $^{\circ}$ | 169 $^{\circ}$ |
| C_3 | 4.10×10^5 | 2.35×10^5 |
| C_{3f} | 4.50×10^4 | 2.70×10^4 |
| Devonshire Coeff.† | | |
| a_{33}^0 | 1.54×10^{-4} | 2.00×10^{-4} |
| a_{333}^0 | -1.04×10^{-2} | -1.73×10^{-2} |
| a_{3333}^0 | 2.20×10^{-1} | 5.00×10^{-1} |
| $a_{33}^0 P_{30}^2$ | 3.47×10^{-6} | 3.64×10^{-6} |
| $a_{333}^0 P_{30}^4$ | -5.26×10^{-6} | -5.75×10^{-6} |
| $a_{3333}^0 P_{30}^6$ | 2.51×10^{-6} | 3.03×10^{-6} |

* Calculated e-o values

† Valid for BSKNN-2 only above 90 $^{\circ}\text{C}$.



Table II
Ferroelectric a-axis Properties of SBN:60 and BSKNN-2

| a-axis | SBN:60 | BSKNN-2 |
|-----------------------------------|-----------------------|-----------------------|
| ϵ_{11} @ 20°C | 475 | 695 |
| r_{51} @ 20°C (10^{-12} m/V) | ~ 80 - 90 (96)* | - (153)* |
| Curie-Weiss Constants | | |
| θ_1 | $-245 \pm 20^\circ$ | $-83 \pm 10^\circ$ |
| $(\theta_3 - \theta_1)$ | 314° | 252° |
| C_1 | 2.04×10^5 | 2.32×10^5 |
| Devonshire Coeff. | | |
| α_{13} | 3.78×10^{-3} | 4.01×10^{-3} |
| α_{133} | 1.40×10^{-2} | 1.14×10^{-2} |
| $\alpha_{13}P_{30}^2$ | 8.50×10^{-5} | 7.31×10^{-5} |
| $\alpha_{133}P_{30}^4$ | 7.08×10^{-6} | 3.79×10^{-6} |

* Calculated e-o values.

approximately $0.10 \text{ m}^4/\text{C}^2$ at optical frequencies.¹² In the case of SBN:60, the calculated room temperature value for r_{33} from Eq. (10) is 464×10^{-12} m/V, in good agreement with measured optical values of $420 - 470 \times 10^{-12}$ m/V.^{1,2,7} However, in the case of BSKNN-2, the calculated value is $r_{33} = 94 \times 10^{-12}$ m/V, roughly one-half the measured value.⁶

This trend persists in the millimeter wave region as well. For SBN:60, the equivalent millimeter wave value for g_{33} increases to approximately $0.60 \text{ m}^4/\text{C}^2$ based on dn_3/dE_3 measurements from 77K to room temperature.^{3,4} Using this value of g_{33} for BSKNN-2, we find $r_{33} = 560 \times 10^{-12}$ at room temperature, a value some 40% less than determined from measured dn_3/dE_3 data.

It appears, then, that a more accurate phenomenological description is needed for BSKNN-2, and perhaps for the BSKNN solid solution system in general. Similar difficulties arise for other tungsten bronzes, such as the $\text{Sr}_{2-x}\text{Ca}_x\text{NaNb}_5\text{O}_{15}$ (SCNN) system in which a very pronounced second dielectric peak is observed.⁴ In the case of BSKNN, any phenome-



nological description involving a second order parameter in the Gibbs free energy function must necessarily be such that it predicts the excess electro-dielectric response below 100°C without any predicted anomalies in the otherwise smooth, monotonic temperature dependencies of the spontaneous polarization and the dielectric properties. There is a considerable body of literature on improper ferroelastic transitions, particularly for tungsten bronze BNN,^{10,13,14} and these may prove to be useful starting points. It remains to be seen, however, whether such an improper ferroelastic phenomenology can be uniquely determined for BSKNN-2 based on measured physical properties.

ACKNOWLEDGEMENTS

The authors would like to thank W.K. Cory for his work in the Czochralski growth of high quality BSKNN crystals, and L.E. Cross and W.F. Hall for their valuable discussions during the course of this research. This work was supported by the Office of Naval Research (Contract No. N00014-81-C-0463).

REFERENCES

1. J.R. Oliver, R.R. Neurgaonkar and L.E. Cross, accepted for publication in the J. Appl. Physics (1988).
2. R.R. Neurgaonkar, W.K. Cory, J.R. Oliver, M.D. Ewbank and W.F. Hall, Opt. Eng. 16, 392 (1987).
3. W.F. Hall, W.W. Ho, R.R. Neurgaonkar and W.K. Cory, Proc. Sixth Int'l Meeting on Applications of Ferroelectrics (ISAF), 469 (1986).
4. R.R. Neurgaonkar, J.R. Oliver, L.E. Cross and W.F. Hall, ONR Annual Report No. 5 (1985) and No. 6 (1986), Contract No. N00014-81-C-0463 (1985).
5. R.R. Neurgaonkar, W.K. Cory and J.R. Oliver, in Phase Conjugation; Beam Combining and Diagnostics (R.A. Fisher and I. Abramowitz, ed.), Proc. SPIE 739, 91 (1987).



6. R.R. Neurgaonkar, W.K. Cory, J.R. Oliver, W.W. Clark III, G.L. Wood, M.J. Miller and E.J. Sharp, *J. Cryst. Growth* 84, 629 (1987).
7. R.R. Neurgaonkar and W.K. Cory, *J. Opt. Soc. Am. B* 3, 274 (1986).
8. A.F. Devonshire, *Adv. Phys.* 3(10), 85 (1954).
9. S.C. Abrahams, *Mat. Res. Bull.* 6, 881 (1971).
10. J. Schneck and F. Denoyer, *Phys. Rev. B* 23(1), 383 (1981).
11. M. DiDomenico and S.H. Wemple, *J. Appl. Phys.* 40(2), 720 (1969).
12. R.R. Neurgaonkar and L.E. Cross, DARPA Semi-Annual Technical Reports No. 1 (1983) and No. 6 (1985), Contract No. N00014-82-C-2466.
13. T. Yamada, H. Iwasaki and N. Niizeki, *J. Appl. Phys.* 41(10), 4141 (1970).
14. J.C. Toledano, *Phys. Rev. B* 12(3), 943 (1975).

ENVO

DATE

FILMED

8-88

DTIC